A λ3mm line survey towards the circumstellar envelope of the carbon-rich AGB star IRC+10216 (CW Leo)

Tuo, J., Li, X., Sun, J., Millar, T. J., Zhang, Y., Qiu, J., Quan, D., Esimbek, J., Zhou, J., Gao, Y., Chang, Q., Xiao, L., Feng, Y., Miao, Z., Ma, R., Szczerba, R., & Fang, X. (2024). A λ3mm line survey towards the circumstellar envelope of the carbon-rich AGB star IRC+10216 (CW Leo). *Astrophysical Journal Supplement*, *271*(2), Article 45. https://doi.org/10.3847/1538-4365/ad2460

Published in:
Astrophysical Journal Supplement

Document Version:
Publisher's PDF, also known as Version of record

Queen's University Belfast - Research Portal:
[Link to publication record in Queen's University Belfast Research Portal](#)

CrossMark

A λ 3 mm Line Survey toward the Circumstellar Envelope of the Carbon-rich AGB Star IRC+10216 (CW Leo)

Juan Tuo[1,2], Xiaohu Li[1,3] , Jixian Sun[4,5], Tom J. Millar[6] , Yong Zhang[1,7,8] , Jianjie Qiu[7] , Donghui Quan[1,9] ,
Jarken Esimbek[1,3], Jianjun Zhou[1,3] , Yu Gao[4,5,10,15] , Qiang Chang[11] , Lin Xiao[12] , Yanan Feng[1,2], Zhenzhen Miao[1,3],
Rong Ma[1,2], Ryszard Szczerba[1,13] , and Xuan Fang[1,8,14]

[1] Xinjiang Astronomical Observatory, Chinese Academy of Sciences, 150 Science 1-Street, Urumqi, Xinjiang 830011, People's Republic of China
xiaohu.li@xao.ac.cn
[2] University of Chinese Academy of Sciences, Beijing 100049, People's Republic of China
[3] Xinjiang Key Laboratory of Radio Astrophysics, 150 Science 1-Street, Urumqi, Xinjiang 830011, People's Republic of China
[4] Purple Mountain Observatory, Chinese Academy of Sciences, Nanjing 210034, People's Republic of China
[5] Key Laboratory of Radio Astronomy, Chinese Academy of Sciences, Nanjing 210034, People's Republic of China
[6] Astrophysics Research Centre, School of Mathematics and Physics, Queen's University Belfast, Belfast, BT7 1NN, UK
[7] School of Physics and Astronomy, Sun Yat-sen University, Guangzhou 510275, People's Republic of China
[8] Laboratory for Space Research, Faculty of Science, The University of Hong Kong, Hong Kong, People's Republic of China
[9] Astronomical Computing Research Center, Zhejiang Laboratory, Hangzhou 311100, People's Republic of China
[10] Department of Astronomy, Xiamen University, Xiamen, Fujian 361005, People's Republic of China
[11] School of Physics and Optoelectronic Engineering, Shandong University of Technology, Zibo, Shandong 255000, People's Republic of China
[12] College of Science, Changchun Institute of Technology, Changchun, Jilin 130012, People's Republic of China
[13] Nicolaus Copernicus Astronomical Center, Rabiańska 8, 87-100 Toruń, Poland
[14] National Astronomical Observatories, Chinese Academy of Sciences, A20, Datun Road, Chaoyang District, 100012 Beijing, People's Republic of China

Abstract

We present an unbiased λ 3 mm spectral line survey (between 84.5 and 115.8 GHz), conducted by the Purple Mountain Observatory 13.7 m radio telescope, together with updated modeling results, toward the carbon-rich asymptotic giant branch star IRC+10216 (CW Leo). A total of 75 spectral lines (96 transitions) are detected, and identified to arise from 19 molecules: C_2H, l-C_3H, C_4H, CN, C_3N, HC_3N, HC_5N, HCN, HNC, CH_3CN, MgNC, CO, c-C_3H_2, SiC_2, SiO, SiS, CS, C_2S, C_3S, and their isotopologues. Among them, one molecular emission line ($H^{13}CCCN$ $J = 13$–12) is discovered in IRC+10216 for the first time. The excitation temperature, column density, and fractional abundance of the detected species are deduced by assuming they are in local thermodynamic equilibrium. In addition, the isotopic ratios of $[^{12}C]/[^{13}C]$, $[^{32}S]/[^{34}S]$, $[^{28}Si]/[^{29}Si]$, and $[^{12}C^{34}S]/[^{13}C^{32}S]$ are obtained and found to be consistent with previous studies. Finally, we summarize all of the 106 species detected in IRC+10216 to date with their observed and modeled column densities for the convenience of future studies.

1. Introduction

One of the most important stages in the evolution of intermediate and low mass stars (0.8–$8\,M_\odot$) is the asymptotic giant branch (AGB) stage. During the AGB phase, the mass-loss rate is about 10^{-8}–$10^{-4}\,M_\odot\,\mathrm{yr}^{-1}$ (De Beck et al. 2010). The ejected material forms a dense circumstellar envelope (CSE) composed of gas and dust. Based on the carbon-to-oxygen abundance ratio ([C]/[O]), AGB stars can be divided into carbon-rich AGB stars (C-rich, [C]/[O] > 1), oxygen-rich AGB stars (O-rich, [C]/[O] < 1), and S-type AGB stars ([C]/[O] ≈ 1) (Olofsson 1996).

IRC+10216 (CW Leo), a C-rich AGB star, is the brightest astronomical source at $5\,\mu$m outside the solar system (Becklin et al. 1969). Its mass-loss rate is about $2 \times 10^{-5}\,M_\odot\,\mathrm{yr}^{-1}$ at a distance of 130 pc to Earth (Crosas & Menten 1997; Menten et al. 2012). As summarized in Table 1, 106 molecular species (note

that these are 35% of the overall known 300 molecules in space[16]) have been detected in the CSE of IRC+10216 (Agúndez et al. 2014; Cernicharo et al. 2017; Fonfría et al. 2018; McGuire 2018, 2022; Cernicharo et al. 2019a, 2019b; Pardo et al. 2022). Molecules that were observed in the CSE of IRC+10216 and the column densities of these molecules calculated by our CSE chemical model (see Section 4.3) are listed in Table 1. The detected molecules include a large number of linear carbon chain molecules such as C_nH ($n = 2$–8) (Tucker et al. 1974; Guélin et al. 1978, 1997; Thaddeus et al. 1985a; Cernicharo et al. 1986a; Saito et al. 1987; Cernicharo & Guélin 1996), HC_nN ($n = 1$–9) (Morris et al. 1971, 1975; Churchwell et al. 1978; Winnewisser & Walmsley 1978; Guélin & Cernicharo 1991; Bell et al. 1992b; Cernicharo et al. 2004), C_nS ($n = 1, 2, 3, 5$) (Penzias et al. 1971; Cernicharo et al. 1987a; Bell et al. 1992b), negatively and positively charged molecules such as C_nH^- ($n = 4, 6, 8$) (McCarthy et al. 2006; Cernicharo et al. 2007; Remijan et al. 2007) and C_nN^- ($n = 1, 3, 5$) (Cernicharo et al. 2008; Thaddeus et al. 2008; Agúndez et al. 2010) and HCO^+ (Tenenbaum et al. 2010b), metal cyanides/isocyanides such as KCN, CaNC, NaCN, MgNC, MgCN,

[16] https://cdms.astro.uni-koeln.de/classic/molecules/

Table 1
Summary of the 106 Detected Species (Excluding Isotopologues) toward the CSE of the Carbon-rich AGB Star, IRC+10216

No.	Species	$N_{\mathrm{obs.}}$ (cm^{-2})	References	$N_{\mathrm{mod.}}$ (cm^{-2})
(1)	C (C I)	$(4.0\text{--}7.0) \times 10^{15}$	Keene et al. (1993)	2.19×10^{16}
	C (C I)	2.5×10^{16}	van der Veen et al. (1998)	2.19×10^{16}
	C (C I)	...	Jeste et al. (2023)	2.19×10^{16}
(2)	C$^+$ (C II)	$(4.0 \pm 0.6) \times 10^{17}$	Reach et al. (2022)	3.83×10^{16}
	C$^+$ (C II)	...	Jeste et al. (2023)	3.83×10^{16}
(3)	C$_2$	7.9×10^{14}	Bakker et al. (1997)	4.79×10^{15}
(4)	OH	...	Ford et al. (2003)	2.96×10^{14}
(5)	HF	...	Agúndez et al. (2011)	1.02×10^{14}
(6)	AlF[a]	$(0.3\text{--}1.1) \times 10^{15}$	Ziurys et al. (1994)	...
	AlF	...	Cernicharo & Guélin (1987)	...
(7)	HCl	...	Cernicharo et al. (2010a)	1.25×10^{15}
(8)	KCl	...	Cernicharo & Guélin (1987)	...
(9)	NaCl	5×10^{12}	Cernicharo & Guélin (1987)	...
(10)	AlCl	...	Cernicharo & Guélin (1987)	...
(11)	CP[a]	5×10^{12}	Halfen et al. (2008)	2.16×10^{12}
	CP	8×10^{13}	Guélin et al. (1990)	2.16×10^{12}
(12)	PN	6.3×10^{12}	Halfen et al. (2008)	3.89×10^{12}
	PN	...	Milam et al. (2008)	3.89×10^{12}
	PN	1.6×10^{12}	Agúndez et al. (2007)	3.89×10^{12}
	PN	...	Guélin et al. (2000)	3.89×10^{12}
	PN	...	Cernicharo et al. (2000)	3.89×10^{12}
(13)	CN	$(1.08 \pm 0.42) \times 10^{15}$	This work	3.25×10^{15}
	CN	2×10^{15}	Agúndez et al. (2010)	3.25×10^{15}
	CN	6.2×10^{14}	Groesbeck et al. (1994)	3.25×10^{15}
	CN	7.6×10^{14}	Avery et al. (1992)	3.25×10^{15}
	CN	1.7×10^{15}	Wootten et al. (1982)	3.25×10^{15}
	CN	...	Wilson et al. (1971)	3.25×10^{15}
(14)	SiN	3.8×10^{13}	Turner (1992)	3.72×10^{11}
(15)	CS	$(1.57 \pm 0.46) \times 10^{15}$	This work	1.02×10^{16}
	CS	5.9×10^{15}	Kawaguchi et al. (1995)	1.02×10^{16}
	CS	3.0×10^{15}	Groesbeck et al. (1994)	1.02×10^{16}
	CS[a]	4×10^{15}	Cernicharo et al. (1987a)	1.02×10^{16}
	CS	1.8×10^{15}	Morris et al. (1975)	1.02×10^{16}
	CS	...	Penzias et al. (1971)	1.02×10^{16}
(16)	SiC	$(4.9 \pm 2.3) \times 10^{13}$	He et al. (2008)	1.95×10^{13}
	SiC[a]	6×10^{13}	Cernicharo et al. (1989)	1.95×10^{13}
(17)	FeC	...	Koelemay & Ziurys (2023)	...
(18)	SiO	$(4.84 \pm 1.13) \times 10^{14}$	This work	1.74×10^{15}
	SiO	4.1×10^{14}	Morris et al. (1975)	1.74×10^{15}
	SiO	5.4×10^{14}	Kawaguchi et al. (1995)	1.74×10^{15}
	SiO	2.1×10^{14}	Groesbeck et al. (1994)	1.74×10^{15}
	SiO	5.4×10^{14}	Kawaguchi et al. (1995)	1.74×10^{15}
(19)	SiS	$(5.86 \pm 1.74) \times 10^{15}$	This work	2.17×10^{16}
	SiS	4.7×10^{15}	Kawaguchi et al. (1995)	2.17×10^{16}
	SiS	3.0×10^{15}	Groesbeck et al. (1994)	2.17×10^{16}
	SiS	$(6.5 \pm 0.5) \times 10^{15}$	Avery et al. (1992)	2.17×10^{16}
	SiS	7×10^{15}	Cernicharo et al. (1987a)	2.17×10^{16}
	SiS	1.6×10^{15}	Morris et al. (1975)	2.17×10^{16}
(20)	CO	$(4.03 \pm 1.51) \times 10^{17}$	This work	1.35×10^{19}
	CO	2.0×10^{18}	Groesbeck et al. (1994)	1.35×10^{19}
	CO	...	Solomon et al. (1971)	1.35×10^{19}
(21)	H$_2$O	...	Melnick et al. (2001)	3.22×10^{16}
(22)	KCN	$(1 \pm 0.2) \times 10^{12}$	Pulliam et al. (2010)	...
(23)	NaCN	$(8.5 \pm 1.7) \times 10^{12}$	Pardo et al. (2022)	...
	NaCN	3.8×10^{14}	Kawaguchi et al. (1995)	...
	NaCN	$(2.0 - 3.8) \times 10^{13}$	Turner et al. (1994)	...
(24)	MgCN	$(7.4 \pm 2) \times 10^{11}$	Cabezas et al. (2013)	...
	MgCN[a]	2×10^{12}	Ziurys et al. (1995)	...
(25)	SiCN[a]	2×10^{12}	Guélin et al. (2000)	...
(26)	FeCN	8.6×10^{11}	Zack et al. (2011)	...
(27)	MgNC	$(3.20 \pm 0.51) \times 10^{13}$	This work	...
	MgNC	$(3.9 \pm 1.5) \times 10^{13}$	Gong et al. (2015)	...
	MgNC	$(1.3 \pm 0.3) \times 10^{13}$	Cabezas et al. (2013)	...

Table 1
(Continued)

No.	Species	$N_{\rm obs.}$ (cm^{-2})	References	$N_{\rm mod.}$ (cm^{-2})
	MgNC	7.8×10^{13}	He et al. (2008)	...
	MgNC	2.5×10^{13}	Kawaguchi et al. (1993)	...
	MgNC	...	Guélin et al. (1993)	...
	MgNC	...	Guélin et al. (1986)	...
(28)	AlNC	9×10^{11}	Ziurys et al. (2002)	...
(29)	SiNC	2×10^{12}	Guélin et al. (2004)	9.35×10^{8}
(30)	CaNC	2×10^{11}	Cernicharo et al. (2019b)	...
(31)	HNC	$(1.11 \pm 0.08) \times 10^{14}$	This work	1.17×10^{14}
	HNC	...	Brown et al. (1976)	1.17×10^{14}
(32)	HCN	$(7.36 \pm 0.92) \times 10^{14}$	This work	2.51×10^{17}
	HCN	2.8×10^{16}	Groesbeck et al. (1994)	2.51×10^{17}
	HCN	...	Morris et al. (1971)	2.51×10^{17}
(33)	MgC$_2$	$(1.0 \pm 0.3) \times 10^{12}$	Changala et al. (2022)	...
(34)	SiC$_2$	$(1.41 \pm 0.34) \times 10^{15}$	This work	6.30×10^{15}
	SiC$_2$	$(1.87 \pm 1.34) \times 10^{15}$	Zhang et al. (2017)	6.30×10^{15}
	SiC$_2$	$(1.2 \pm 0.0) \times 10^{15}$	Gong et al. (2015)	6.30×10^{15}
	SiC$_2$[b]	$(2.35 \pm 0.36) \times 10^{15}$	He et al. (2008)	6.30×10^{15}
	SiC$_2$[c]	$(5.40 \pm 0.88) \times 10^{14}$	He et al. (2008)	6.30×10^{15}
	SiC$_2$[d]	1.04×10^{15}	He et al. (2008)	6.30×10^{15}
	SiC$_2$[e]	5.3×10^{15}	He et al. (2008)	6.30×10^{15}
	SiC$_2$	2.2×10^{14}	Kawaguchi et al. (1995)	6.30×10^{15}
	SiC$_2$	3.7×10^{14}	Groesbeck et al. (1994)	6.30×10^{15}
	SiC$_2$	(cold range) 9.5×10^{14}	Avery et al. (1992)	6.30×10^{15}
	SiC$_2$	(warm range) 1.9×10^{15}	Avery et al. (1992)	6.30×10^{15}
	SiC$_2$[a]	2×10^{15}	Cernicharo et al. (1987a)	6.30×10^{15}
	SiC$_2$	1.5×10^{14}	Thaddeus et al. (1984)	6.30×10^{15}
(35)	SiCSi[f]	$(1.4 \pm 0.4) \times 10^{15}$	Cernicharo et al. (2015b)	...
	SiCSi[g]	$(3.0 \pm 0.7) \times 10^{15}$	Cernicharo et al. (2015b)	...
	SiCSi[h]	$(3.2 \pm 0.9) \times 10^{15}$	Cernicharo et al. (2015b)	...
(36)	C$_3$	1×10^{15}	Hinkle et al. (1988)	1.93×10^{14}
(37)	H$_2$S[a]	1×10^{13}	Cernicharo et al. (1987a)	5.11×10^{13}
(38)	HCP	$(1.0 - 1.4) \times 10^{14}$	Halfen et al. (2008)	3.17×10^{14}
	HCP	1.3×10^{15}	Agúndez et al. (2007)	3.17×10^{14}
(39)	C$_2$H	$(8.14 \pm 2.29) \times 10^{15}$	This work	1.01×10^{16}
	C$_2$H	$(3.84 \pm 0.09) \times 10^{15}$	De Beck et al. (2012)	1.01×10^{16}
	C$_2$H	5.0×10^{15}	Cernicharo et al. (2000)	1.01×10^{16}
	C$_2$H	4.6×10^{15}	Groesbeck et al. (1994)	1.01×10^{16}
	C$_2$H	5.4×10^{15}	Avery et al. (1992)	1.01×10^{16}
	C$_2$H	...	Tucker et al. (1974)	1.01×10^{16}
(40)	C$_2$P	1.2×10^{12}	Halfen et al. (2008)	8.99×10^{9}
(41)	C$_2$S	$(1.59 \pm 0.73) \times 10^{14}$	This work	1.84×10^{13}
	C$_2$S	$(4.0 \pm 0.7) \times 10^{13}$	Pardo et al. (2022)	1.84×10^{13}
	C$_2$S	$(2.3 \pm 0.8) \times 10^{14}$	Gong et al. (2015)	1.84×10^{13}
	C$_2$S	$(5.0 \pm 0.3) \times 10^{13}$	Agúndez et al. (2014)	1.84×10^{13}
	C$_2$S	1.5×10^{14}	Kawaguchi et al. (1995)	1.84×10^{13}
	C$_2$S	$(9 \pm 2) \times 10^{13}$	Bell et al. (1993)	1.84×10^{13}
	C$_2$S	1.5×10^{14}	Cernicharo et al. (1987a)	1.84×10^{13}
(42)	C$_2$N	$(1.1 \pm 0.6) \times 10^{13}$	Anderson & Ziurys (2014)	1.46×10^{13}
(43)	l-C$_3$H	$(1.25 \pm 0.22) \times 10^{14}$	This work	1.42×10^{14}
	l-C$_3$H	$(1.32 \pm 0.34) \times 10^{14}$	He et al. (2008)	1.42×10^{14}
	l-C$_3$H	7.0×10^{13}	Cernicharo et al. (2000)	1.42×10^{14}
	l-C$_3$H	5.6×10^{13}	Kawaguchi et al. (1995)	1.42×10^{14}
	l-C$_3$H	2.8×10^{13}	Thaddeus et al. (1985a)	1.42×10^{14}
(44)	c-C$_3$H	...	Cernicharo et al. (2000)	...
(45)	H$_2$CO	5×10^{12}	Ford et al. (2004)	2.80×10^{11}
(46)	NH$_3$ (para)	$(2.3, 2.7) \times 10^{14}$	Gong et al. (2015)	2.50×10^{16}
	NH$_3$ (ortho)	$(1.5, 2.9) \times 10^{14}$	Gong et al. (2015)	2.50×10^{16}
	NH$_3$	4.2×10^{13}	Nguyen-Q-Rieu et al. (1984)	2.50×10^{16}
	NH$_3$	1×10^{17}	Betz et al. (1979)	2.50×10^{16}
(47)	C$_3$S	$(3.27 \pm 0.16) \times 10^{13}$	This work	1.55×10^{13}
	C$_3$S	$(2.58 \pm 3.60) \times 10^{13}$	Pardo et al. (2022)	1.55×10^{13}
	C$_3$S	$(2.2 \pm 0.4) \times 10^{13}$	Gong et al. (2015)	1.55×10^{13}
	C$_3$S	$(1.7 \pm 0.1) \times 10^{13}$	Agúndez et al. (2014)	1.55×10^{13}

Table 1
(Continued)

No.	Species	$N_{\rm obs.}$ (cm^{-2})	References	$N_{\rm mod.}$ (cm^{-2})
	C$_3$S	$(4.9 \pm 0.3) \times 10^{13}$	Kawaguchi et al. (1995)	1.55×10^{13}
	C$_3$S	$(5.8 \pm 2.7) \times 10^{12}$	Bell et al. (1993)	1.55×10^{13}
	C$_3$S	1.1×10^{14}	Cernicharo et al. (1987a)	1.55×10^{13}
(49)	C$_3$N	$(4.25 \pm 0.81) \times 10^{14}$	This work	5.85×10^{14}
	C$_3$N	$(3.1 \pm 0.3) \times 10^{14}$	Gong et al. (2015)	5.85×10^{14}
	C$_3$N	$(4.54 \pm 2.13) \times 10^{14}$	He et al. (2008)	5.85×10^{14}
	C$_3$N	2.5×10^{14}	Cernicharo et al. (2000)	5.85×10^{14}
	C$_3$N	4.1×10^{14}	Kawaguchi et al. (1995)	5.85×10^{14}
(49)	C$_2$H$_2$	3×10^{19}	Ridgway et al. (1976)	9.94×10^{17}
(50)	H$_2$CS[a]	1.0×10^{13}	Agúndez et al. (2008b)	5.01×10^{11}
(51)	SiC$_3$	(cold range) 4.3×10^{12}	Apponi et al. (1999)	2.03×10^{12}
	SiC$_3$	(warm range) 4.3×10^{12}	Apponi et al. (1999)	2.03×10^{12}
(52)	C$_3$O	1.2×10^{12}	Tenenbaum et al. (2006)	1.07×10^{12}
(53)	HC$_2$N	1.4×10^{13}	Cernicharo et al. (2004)	…
	HC$_2$N	1.8×10^{13}	Kawaguchi et al. (1995)	…
	HC$_2$N	1.2×10^{13}	Guélin & Cernicharo (1991)	…
(54)	HMgNC	6×10^{11}	Cabezas et al. (2013)	…
(55)	MgCCH	2×10^{12}	Agúndez et al. (2014)	…
	MgCCH	2×10^{12}	Cernicharo et al. (2019a)	…
(56)	NCCP[i]	7×10^{11}	Agúndez et al. (2014)	…
(57)	PH$_3$	…	Agúndez et al. (2008a)	…
	PH$_3$	…	Tenenbaum & Ziurys (2008)	…
(58)	C$_5$	1×10^{14}	Bernath et al. (1989)	1.61×10^{14}
(59)	c-C$_3$H$_2$ (ortho)	$(1.14 \pm 0.15) \times 10^{14}$	This work	5.85×10^{13}
	c-C$_3$H$_2$ (para)	$(8.02 \pm 4.54) \times 10^{13}$	This work	5.85×10^{13}
	c-C$_3$H$_2$	$(1.39 \pm 1.07) \times 10^{14}$	Zhang et al. (2017)	5.85×10^{13}
	c-C$_3$H$_2$ (ortho)	$(1.2 \pm 0.3) \times 10^{14}$	Gong et al. (2015)	5.85×10^{13}
	c-C$_3$H$_2$ (para)	$(8.9 \pm 0.5) \times 10^{13}$	Gong et al. (2015)	5.85×10^{13}
	c-C$_3$H$_2$ (ortho)	$(4.82 \pm 4.14) \times 10^{14}$	He et al. (2008)	5.85×10^{13}
	c-C$_3$H$_2$ (para)	$(1.22 \pm 2.03) \times 10^{14}$	He et al. (2008)	5.85×10^{13}
	c-C$_3$H$_2$	1.6×10^{13}	Kawaguchi et al. (1995)	5.85×10^{13}
(60)	H$_2$C$_3$	2.6×10^{12}	Cernicharo et al. (1991a)	1.20×10^{13}
(61)	HC$_3$N	$(1.18 \pm 0.08) \times 10^{15}$	This work	4.79×10^{14}
	HC$_3$N	$(1.94 \pm 0.21) \times 10^{15}$	Zhang et al. (2017)	4.79×10^{14}
	HC$_3$N	$(1.4 \pm 0.2) \times 10^{15}$	Gong et al. (2015)	4.79×10^{14}
	HC$_3$N	$(8.0 \pm 1.5) \times 10^{14}$	He et al. (2008)	4.79×10^{14}
	HC$_3$N	1.7×10^{15}	Kawaguchi et al. (1995)	4.79×10^{14}
	HC$_3$N	(cold range) $(7.9 \pm 0.2) \times 10^{14}$	Bell (1993)	4.79×10^{14}
	HC$_3$N	(warm range) $(2.1 \pm 1.4) \times 10^{14}$	Bell (1993)	4.79×10^{14}
	HC$_3$N	5.9×10^{14}	Gensheimer (1997a)	4.79×10^{14}
	HC$_3$N	1.1×10^{15}	Gensheimer (1997b)	4.79×10^{14}
	HC$_3$N	$(1.6 \pm 0.4) \times 10^{15}$	Jewell & Snyder (1984)	4.79×10^{14}
	HC$_3$N	1.8×10^{15}	Morris et al. (1975)	4.79×10^{14}
(62)	HNC$_3$[a]	1×10^{12}	Gensheimer (1997a)	7.32×10^{11}
(63)	HC$_2$NC	$2.8, 3.6 \times 10^{12}$	Gensheimer (1997a)	…
	HC$_2$NC[a]	8.4×10^{12}	Gensheimer (1997b)	…
(64)	CH$_2$CN	$(8.6 \pm 1.4) \times 10^{12}$	Agúndez et al. (2008b)	2.58×10^{11}
(65)	CH$_2$NH	9×10^{12}	Tenenbaum et al. (2010a)	2.56×10^{11}
(66)	C$_4$H	$(2.75 \pm 0.36) \times 10^{15}$	This work	6.57×10^{14}
	C$_4$H	$(1.84 \pm 0.25) \times 10^{14}$	Pardo et al. (2022)	6.57×10^{14}
	C$_4$H	$(2.4 \pm 0.2) \times 10^{15}$	Gong et al. (2015)	6.57×10^{14}
	C$_4$H	$(8.1 \pm 1.1) \times 10^{15}$	He et al. (2008)	6.57×10^{14}
	C$_4$H	3.0×10^{14}	Cernicharo et al. (2000)	6.57×10^{14}
	C$_4$H	$(0.4 - 3) \times 10^{15}$	Guélin et al. (1978)	6.57×10^{14}
	C$_4$H	2.4×10^{15}	Kawaguchi et al. (1995)	6.57×10^{14}
	C$_4$H	5.6×10^{15}	Avery et al. (1992)	6.57×10^{14}
(67)	CH$_4$	2.5×10^{17}	Hall & Ridgway (1978)	4.41×10^{16}
	CH$_4$	1.8×10^{16}	Clegg et al. (1982)	4.41×10^{16}
(68)	SiH$_4$	2×10^{15}	Goldhaber & Betz (1984)	2.78×10^{15}
(69)	SiC$_4$	$(6.2 \pm 1.0) \times 10^{12}$	Pardo et al. (2022)	2.45×10^{11}
	SiC$_4$	$(1.46 \pm 0.92) \times 10^{13}$	Zhang et al. (2017)	2.45×10^{11}
	SiC$_4$	$(1.1 \pm 0.4) \times 10^{13}$	Gong et al. (2015)	2.45×10^{11}
	SiC$_4$	7×10^{12}	Kawaguchi et al. (1995)	2.45×10^{11}

Table 1
(Continued)

No.	Species	$N_{obs.}$ (cm^{-2})	References	$N_{mod.}$ (cm^{-2})
	SiC$_4$	$(7 \pm 1) \times 10^{12}$	Ohishi et al. (1989)	2.45×10^{11}
(70)	NaC$_3$N	$(1.2 \pm 0.2) \times 10^{11}$	Cabezas et al. (2023)	...
(71)	MgC$_3$N	$(5.2 \pm 0.6) \times 10^{12}$	Pardo et al. (2022)	...
	MgC$_3$N	(cold range) $(5.7 \pm 1.0) \times 10^{12}$	Cernicharo et al. (2019a)	...
	MgC$_3$N	(warm range) $(3.6 \pm 0.6) \times 10^{12}$	Cernicharo et al. (2019a)	...
(72)	MgC$_4$H	$(1.5 \pm 1.3) \times 10^{13}$	Pardo et al. (2022)	...
	MgC$_4$H	$(2.2 \pm 0.5) \times 10^{13}$	Cernicharo et al. (2019a)	...
(73)	HMgC$_3$N	$(3.0 \pm 0.6) \times 10^{12}$	Cabezas et al. (2023)	...
(74)	C$_5$H $^2\Pi_{1/2}$	$(2.7 \pm 0.5) \times 10^{13}$	Pardo et al. (2022)	4.40×10^{13}
	C$_5$H $^2\Pi_{3/2}$	$(2.52 \pm 2.48) \times 10^{14}$	Pardo et al. (2022)	4.40×10^{13}
	C$_5$H $^2\Pi_{1/2}$	$(2.96 \pm 1.21) \times 10^{14}$	Zhang et al. (2017)	4.40×10^{13}
	C$_5$H $^2\Pi_{1/2}$	$(2.9 \pm 0.6) \times 10^{13}$	Gong et al. (2015)	4.40×10^{13}
	C$_5$H $^2\Pi_{3/2}$	$(1.2 \pm 2.3) \times 10^{14}$	Gong et al. (2015)	4.40×10^{13}
	C$_5$H	4.4×10^{13}	Cernicharo et al. (2000)	4.40×10^{13}
	C$_5$H $^2\Pi_{1/2}$	$(2.9 \pm 0.3) \times 10^{14}$	Kawaguchi et al. (1995)	4.40×10^{13}
	C$_5$H $^2\Pi_{3/2}$	$(2.0 \pm 0.1) \times 10^{14}$	Kawaguchi et al. (1995)	4.40×10^{13}
	C$_5$H	...	Cernicharo et al. (1986a)	4.40×10^{13}
(75)	C$_2$H$_4$	(cold) $(1.7 \pm 0.4) \times 10^{15}$	Fonfría et al. (2017)	8.59×10^{14}
	C$_2$H$_4$	(warm) $(4.8 \pm 1.3) \times 10^{15}$	Fonfría et al. (2017)	8.59×10^{14}
	C$_2$H$_4$	4×10^{15}	Goldhaber et al. (1987)	8.59×10^{14}
	C$_2$H$_4$	10^{16}	Betz (1981)	8.59×10^{14}
(76)	HC$_4$N	$(3.9 \pm 3.7) \times 10^{12}$	Pardo et al. (2022)	...
	HC$_4$N[a]	1.5×10^{12}	Cernicharo et al. (2004)	...
(77)	H$_2$C$_4$	3×10^{12}	Kawaguchi et al. (1995)	...
	H$_2$C$_4$	1.6×10^{13}	Cernicharo et al. (1991b)	...
(78)	C$_5$N[a]	6.3×10^{12}	Cernicharo et al. (2000)	2.91×10^{13}
	C$_5$N[a]	3.1×10^{11}	Guélin et al. (1998)	2.91×10^{13}
(79)	CH$_3$CN	$(6.81 \pm 3.51) \times 10^{13}$	This work	4.88×10^{12}
	CH$_3$CN	$(2.6 \pm 0.6) \times 10^{13}$	He et al. (2008)	4.88×10^{12}
	CH$_3$CN	6×10^{12}	Kawaguchi et al. (1995)	4.88×10^{12}
	CH$_3$CN	6×10^{12}	Guélin & Cernicharo (1991)	4.88×10^{12}
	CH$_3$CN	...	Johansson et al. (1984)	4.88×10^{12}
(80)	SiH$_3$CN	1×10^{12}	Agúndez et al. (2014)	...
(81)	C$_5$S	$(0.2 - 1.4) \times 10^{13}$	Agúndez et al. (2014)	...
	C$_5$S[a]	3.6×10^{13}	Bell et al. (1993)	...
(82)	C$_6$H $^2\Pi_{1/2}$	$(1.23 \pm 0.18) \times 10^{13}$	Pardo et al. (2022)	6.01×10^{14}
	C$_6$H $^2\Pi_{3/2}$	$(1.51 \pm 0.14) \times 10^{13}$	Pardo et al. (2022)	6.01×10^{14}
	C$_6$H $^2\Pi_{1/2}$	$(1.85 \pm 0.90) \times 10^{13}$	Zhang et al. (2017)	6.01×10^{14}
	C$_6$H $^2\Pi_{1/2}$	$(1.0 \pm 0.2) \times 10^{14}$	Gong et al. (2015)	6.01×10^{14}
	C$_6$H $^2\Pi_{3/2}$	$(1.0 \pm 0.1) \times 10^{14}$	Gong et al. (2015)	6.01×10^{14}
	C$_6$H $^2\Pi_{3/2}$	$(6.6 \pm 2.0) \times 10^{13}$	Cernicharo et al. (2007)	6.01×10^{14}
	C$_6$H	5.5×10^{13}	Cernicharo et al. (2000)	6.01×10^{14}
	C$_6$H $^2\Pi_{1/2}$	$(1.13 \pm 0.06) \times 10^{14}$	Kawaguchi et al. (1995)	6.01×10^{14}
	C$_6$H $^2\Pi_{3/2}$	$(1.67 \pm 0.07) \times 10^{14}$	Kawaguchi et al. (1995)	6.01×10^{14}
	C$_6$H $^2\Pi_{1/2}$	$(3 \pm 1) \times 10^{13}$	Saito et al. (1987)	6.01×10^{14}
	C$_6$H $^2\Pi_{3/2}$	$(1^{+1.5}_{-0.5}) \times 10^{13}$	Saito et al. (1987)	6.01×10^{14}
	C$_6$H[a]	3×10^{14}	Cernicharo et al. (1987b)	6.01×10^{14}
(83)	HC$_5$N	$(5.41 \pm 0.56) \times 10^{14}$	This work	1.39×10^{14}
	HC$_5$N	$(4.2 \pm 0.4) \times 10^{14}$	Pardo et al. (2022)	1.39×10^{14}
	HC$_5$N	$(5.47 \pm 0.77) \times 10^{14}$	Zhang et al. (2017)	1.39×10^{14}
	HC$_5$N	$(4.6 \pm 0.2) \times 10^{14}$	Gong et al. (2015)	1.39×10^{14}
	HC$_5$N	$(2.3 - 5.47) \times 10^{14}$	Kawaguchi et al. (1995)	1.39×10^{14}
	HC$_5$N	(warm range) $(2.3 - 5.47) \times 10^{14}$	Bell (1993)	1.39×10^{14}
	HC$_5$N	(cold range) 3.2×10^{14}	Bell et al. (1992b)	1.39×10^{14}
	HC$_5$N	(warm range) 3.7×10^{14}	Bell et al. (1992b)	1.39×10^{14}
	HC$_5$N	4×10^{14}	Winnewisser & Walmsley (1978)	1.39×10^{14}
	HC$_5$N	...	Churchwell et al. (1978)	1.39×10^{14}
(84)	SiC$_6$[i]	1.3×10^{12}	Pardo et al. (2022)	...
(85)	CH$_2$CHCN	5.5×10^{12}	Agúndez et al. (2008b)	4.71×10^{11}
(86)	CH$_3$CCH[a]	1.8×10^{13}	Agúndez et al. (2008b)	1.44×10^{12}
(87)	MgC$_5$N	4.7×10^{12}	Pardo et al. (2022, 2021)	...
(88)	MgC$_6$H	2.0×10^{13}	Pardo et al. (2022, 2021)	...
(89)	CH$_3$SiH$_3$	...	Cernicharo et al. (2017)	...

Table 1
(Continued)

No.	Species	$N_{\rm obs.}$ (cm^{-2})	References	$N_{\rm mod.}$ (cm^{-2})
(90)	$C_7H\ ^2\Pi_{1/2}$	$(5.1 \pm 1.0) \times 10^{12}$	Pardo et al. (2022)	7.11×10^{13}
	$C_7H\ ^2\Pi_{3/2}$	$(3.2 \pm 2.0) \times 10^{12}$	Pardo et al. (2022)	7.11×10^{13}
	C_7H	2.2×10^{12}	Cernicharo et al. (2000)	7.11×10^{13}
	C_7H	2×10^{12}	Guélin et al. (1997)	7.11×10^{13}
(91)	C_6H_2	...	Guélin et al. (2000, 1997)	6.96×10^{14}
(92)	HC_7N	$(1.95 \pm 0.11) \times 10^{14}$	Pardo et al. (2022)	4.61×10^{13}
	HC_7N	$(1.52 - 6.21) \times 10^{14}$	Zhang et al. (2017)	4.61×10^{13}
	HC_7N	$(3.7 \pm 0.4) \times 10^{14}$	Gong et al. (2015)	4.61×10^{13}
	HC_7N	$(1.29 \pm 0.06) \times 10^{14}$	Kawaguchi et al. (1995)	4.61×10^{13}
	HC_7N[a]	2×10^{14}	Winnewisser & Walmsley (1978)	4.61×10^{13}
(93)	$C_8H\ ^1\Pi_{3/2}$	$(1.15 \pm 1.38) \times 10^{13}$	Pardo et al. (2022)	1.38×10^{14}
	$C_8H\ ^2\Pi_{3/2}$	$(8.9 \pm 0.9) \times 10^{12}$	Pardo et al. (2022)	1.38×10^{14}
	$C_8H\ ^2\Pi_{3/2}$	$(5.00 \pm 1.008) \times 10^{13}$	Zhang et al. (2017)	1.38×10^{14}
	$C_8H\ ^2\Pi_{3/2}$	$(8.4 \pm 1.4) \times 10^{13}$	Gong et al. (2015)	1.38×10^{14}
	C_8H	$(8 \pm 3) \times 10^{12}$	Remijan et al. (2007)	1.38×10^{14}
	C_8H	1.0×10^{13}	Cernicharo et al. (2000)	1.38×10^{14}
	C_8H	5.5×10^{12}	Cernicharo & Guélin (1996)	1.38×10^{14}
(94)	HC_9N	$(4.5 \pm 0.6) \times 10^{13}$	Pardo et al. (2022)	1.31×10^{13}
	HC_9N	$(5.88 \pm 1.28) \times 10^{13}$	Zhang et al. (2017)	1.31×10^{13}
	HC_9N	$(2.5 \pm 1.4) \times 10^{13}$	Gong et al. (2015)	1.31×10^{13}
	HC_9N	$(2.7 \pm 0.9) \times 10^{13}$	Kawaguchi et al. (1995)	1.31×10^{13}
	HC_9N	4×10^{13}	Bell et al. (1992a)	1.31×10^{13}
(95)	CN^-	5×10^{12}	Agúndez et al. (2010)	5.56×10^{10}
(96)	HCO^+	...	Pulliam et al. (2011)	1.98×10^{12}
	HCO^+	...	Tenenbaum et al. (2010b)	1.98×10^{12}
(97)	C_3N^-	1.6×10^{12}	Thaddeus et al. (2008)	3.07×10^{11}
(98)	C_4H^-	$(7.1 \pm 2.0) \times 10^{11}$	Cernicharo et al. (2007)	1.28×10^{13}
(99)	MgC_3N^+	$(1.2 \pm 0.2) \times 10^{11}$	Cernicharo et al. (2023a)	...
(100)	MgC_4H^+	$(4.8 \pm 0.3) \times 10^{11}$	Cernicharo et al. (2023a)	...
(101)	C_5N^-	$(4.9 \pm 1.6) \times 10^{12}$	Pardo et al. (2022)	3.58×10^{12}
	C_5N^-	$(3.4 - 4.9) \times 10^{12}$	Cernicharo et al. (2008)	3.58×10^{12}
	C_5N^-	$(5.7 \pm 0.2) \times 10^{12}$	Cernicharo et al. (2023b)	3.58×10^{12}
(102)	C_6H^-	$(4.3 \pm 0.6) \times 10^{12}$	Pardo et al. (2022)	8.71×10^{13}
	C_6H^-	$(6.11 \pm 2.99) \times 10^{12}$	Zhang et al. (2017)	8.71×10^{13}
	C_6H^-	$(5.8 \pm 0.5) \times 10^{12}$	Gong et al. (2015)	8.71×10^{13}
	C_6H^-	$(6.1 - 8.0) \times 10^{12}$	Kasai et al. (2007)	8.71×10^{13}
	C_6H^-	$(4.1 \pm 1.5) \times 10^{12}$	Cernicharo et al. (2007)	8.71×10^{13}
	C_6H^-	4×10^{12}	McCarthy et al. (2006)	8.71×10^{13}
(103)	MgC_5N^+	$(1.1 \pm 0.2) \times 10^{11}$	Cernicharo et al. (2023a)	...
(104)	MgC_6H^+	$(2.5 \pm 0.3) \times 10^{11}$	Cernicharo et al. (2023a)	...
(105)	C_7N^-	$(2.4 \pm 0.2) \times 10^{12}$	Cernicharo et al. (2023b)	...
(106)	C_8H^-	$(1.1 \pm 0.4) \times 10^{12}$	Pardo et al. (2022)	3.30×10^{12}
	C_8H^-	$(8 \pm 3) \times 10^{12}$	Remijan et al. (2007)	3.30×10^{12}
	C_8H^-	$(1.5 \pm 0.6) \times 10^{12}$	Kawaguchi et al. (2007)	3.30×10^{12}

Notes. Included in the table are the the species' total column density from both observations ($N_{\rm obs.}$) and an astrochemical model ($N_{\rm mod.}$) that has been updated from Li et al. (2014) and is briefly described in Section 4.3.
[a] Assumed rotational temperature.
[b] The range of data for SiC_2 fitting is $J_{\rm (up)} = 6, 7$; $K_a = 0, 2, 4$.
[c] The range of data for SiC_2 fitting is $J_{\rm (up)} = 9, 10, 11, 12$; $K_a = 0, 2, 4$.
[d] The range of data for SiC_2 fitting is $J_{\rm (up)} = 10, 11$; $K_a = 6$.
[e] The range of data for SiC_2 fitting is $J_{\rm (up)} = 10, 11$; $K_a = 8$.
[f] The range of upper-level energy for SiCSi fitting is $E_{\rm u} < 60$ K.
[g] The range of upper-level energy for SiCSi fitting is 60 K $< E_{\rm u} < 200$ K.
[h] The range of upper-level energy for SiCSi fitting is $E_{\rm u} > 200$ K.
[i] The detection of SiC_6 is marginal and the identification of NCCP is tentative.

(This table is available in machine-readable form.)

AlNC, FeCN, SiCN, SiNC, HMgNC, and SiH$_3$CN (Kawaguchi et al. 1993; Turner et al. 1994; Ziurys et al. 1995, 2002; Guélin et al. 2000, 2004; Pulliam et al. 2010; Zack et al. 2011; Cabezas et al. 2013; Cernicharo et al. 2017, 2019b), and even metal halides such as NaCl, AlCl, KCl, and AlF (Cernicharo & Guélin 1987). Some of these molecules, such as the metal halides and the metal-bearing molecules, were identified during line surveys, covering a significant part of the radio and (sub)

millimeter spectrum (Cernicharo et al. 2011). Therefore, unbiased spectral line surveys are of fundamental importance to the systematic evaluation of the molecular composition and in particular to those species whose chemistries are poorly studied. For example, the first identified Ca-bearing species in space, CaNC, was discovered by a full spectral line survey despite not being expected from chemical models (Cernicharo et al. 2019b).

Multiple transition lines of each molecular species observed in different spectral line surveys have greatly improved estimates of molecular abundances and excitation temperatures, thus better estimating the physical conditions in which each molecular species occurs. By fitting several spectral lines of C_3S, HC_3N, and HC_5N in the CSE of IRC+10216 in different wavebands, it was found that these molecules all have both cold and warm excitation temperature components (Bell et al. 1992b, 1993; Bell 1993). Later, Zhang et al. (2017) fitted the spectral line survey data of HC_5N, HC_7N, and HC_9N in three different frequency ranges and found that the high rotational transitions of these molecules trace the warmer molecular regions and that the thermal structure is stratified, which is consistent with the results for HC_5N from the CSE of the C-rich AGB star CIT6 (Chau et al. 2012).

Molecular line surveys are a powerful tool for analyzing the physical and chemical parameters of astronomical sources. IRC+10216 is the definitive source for studying the circumstellar chemistry in the late stages of stellar evolution (Zhang et al. 2020), and there have been many reports on its detailed and high-sensitivity surveys at centimeter, millimeter, and submillimeter wavelengths. Based on the works of Gong et al. (2015) and Zhang et al. (2017), we collected the published line surveys toward IRC +10216 and listed them in Table 2. We find that Johansson et al. (1984) carried out the first survey toward IRC+10216 with the OSO 20 m telescope at ∼3.8 mm (72.2–91.1 GHz), and they reviewed the excitation conditions and relative abundances of molecules in the CSE of IRC+10216. Agúndez et al. (2014) mainly reconfirmed three transitions of C_5S and preliminarily identified four transitions of MgCCH, three transitions of NCCP, and six transitions of SiH_3CN within the $\lambda \sim 3$ mm region of IRC+10216, while Agúndez et al. (2017) mainly explored the growth mechanism of carbon-chain molecules in IRC+10216 based on data in this band.

Note, however, that a systematic spectral line survey in the frequency range of 91–116 GHz is still missing, with the original survey of Johansson et al. (1984, 1985) only covering frequencies up to 91 GHz (see Table 2). Therefore, we present a spectral line survey of the C-rich AGB star IRC+10216 in the λ 3 mm (84.5–115.8 GHz) region using the Purple Mountain Observatory 13.7 m radio telescope (PMO 13.7 m).

We describe the observations and data reduction process in Section 2. and present the identification of the emission lines in Section 3. Section 4 contains the observationally deduced and modeled excitation temperatures, column densities, and the fractional abundances of detected species, together with their isotopic ratios. Our conclusions are given in Section 5. Further information is included in the six appendices. The complete spectra of the survey of IRC+10216 in the range of 84.5–115.8 GHz are shown in Appendix A. The spectral line parameters of all the identified species from this survey are presented in Appendix B. All the observed spectral profiles

Table 2
Published Radio Line Surveys toward IRC+10216[a]

Covered Frequencies (GHz)	Telescope	References
4–6	Arecibo 305 m	Araya et al. (2003)
13.3–18.5	TMRT 65 m	Zhang et al. (2017)
17.8–26.3	Effelsberg 100 m	Gong et al. (2015)
18–50	VLA	Keller et al. (2015)
20–25	Nobeyama 45 m	Zhang et al. (2020)
28–50	Nobeyama 45 m	Kawaguchi et al. (1995)
31.3–50.6	Yebes 40 m	Tercero et al. (2021)
31.3–50.3	Yebes 40 m	Pardo et al. (2022)
72.2–91.1	Onsala 20 m	Johansson et al. (1984, 1985)
84.5–115.8	PMO 13.7 m	This work
129.0–172.5	IRAM 30 m	Cernicharo et al. (2000)
131.2–160.3	ARO 12 m	He et al. (2008)
214.5–285.5	SMT 10 m	Tenenbaum et al. (2010b)
219.5–245.5 and 251.5–267.5	SMT 10 m	He et al. (2008)
222.4–267.92[b]	JCMT 15 m	Avery et al. (1992)
253–261	CARMA	Fonfría et al. (2014)
255.3–274.8	ALMA	Cernicharo et al. (2013)
255.3–274.8	ALMA	Velilla Prieto et al. (2015)
293.9–354.8	SMA	Patel et al. (2011)
330.2–358.1	CSO 10.4 m	Groesbeck et al. (1994)
339.6–364.6	JCMT 15 m	Avery et al. (1992)
554.5–636.5	Herschel/HIFI	Cernicharo et al. (2010b)

Notes. A collection of line surveys of evolved stars at the λ 3 mm wavelength band can be found in Table 7.
[a] Unpublished work is not included in this table; for instance, the 3 mm IRAM 30 m and ALMA surveys toward IRC+10216 mentioned in the papers of Agúndez et al. (2014, 2017).
[b] The line survey was discontinuously conducted in the listed frequency range and contains significant gaps.

are included in Appendix C. A detailed description of the detected molecules from this survey, as well as from previous observations, is included in Appendix D. Appendix E presents the rotational diagrams for the identified species, while the stratified thermal structures of a few molecules can be found in Appendix F. Detailed comparisons of emission lines obtained with different angular resolutions are included in Appendix G.

2. Observations and Data Reduction

The spectral line survey of IRC+10216 between 84.5 and 115.8 GHz was carried out in 2019 August using the PMO 13.7 m millimeter-wave radio telescope of the Purple Mountain Observatory in Delingha, China. The typical system temperature was about 150–300 K (Li et al. 2013). The front end of the receiver uses a nine-beam sideband separation Superconduction Spectroscopic Array Receiver system, and the back end consists of 18 high-resolution digital spectrum analyzer fast Fourier transform spectrometers (FFTSs). Each FFTS provides 16,384 channels with a total bandwidth of 1 GHz (Shan et al. 2012). The beam separation of the nine beams of the PMO 13.7 m telescope is 3′. The observations adopted the position-switching mode using the standard chopper wheel calibration method. The position-switching mode uses only one beam, while the other beams point to other parts of the sky. On- and off-source
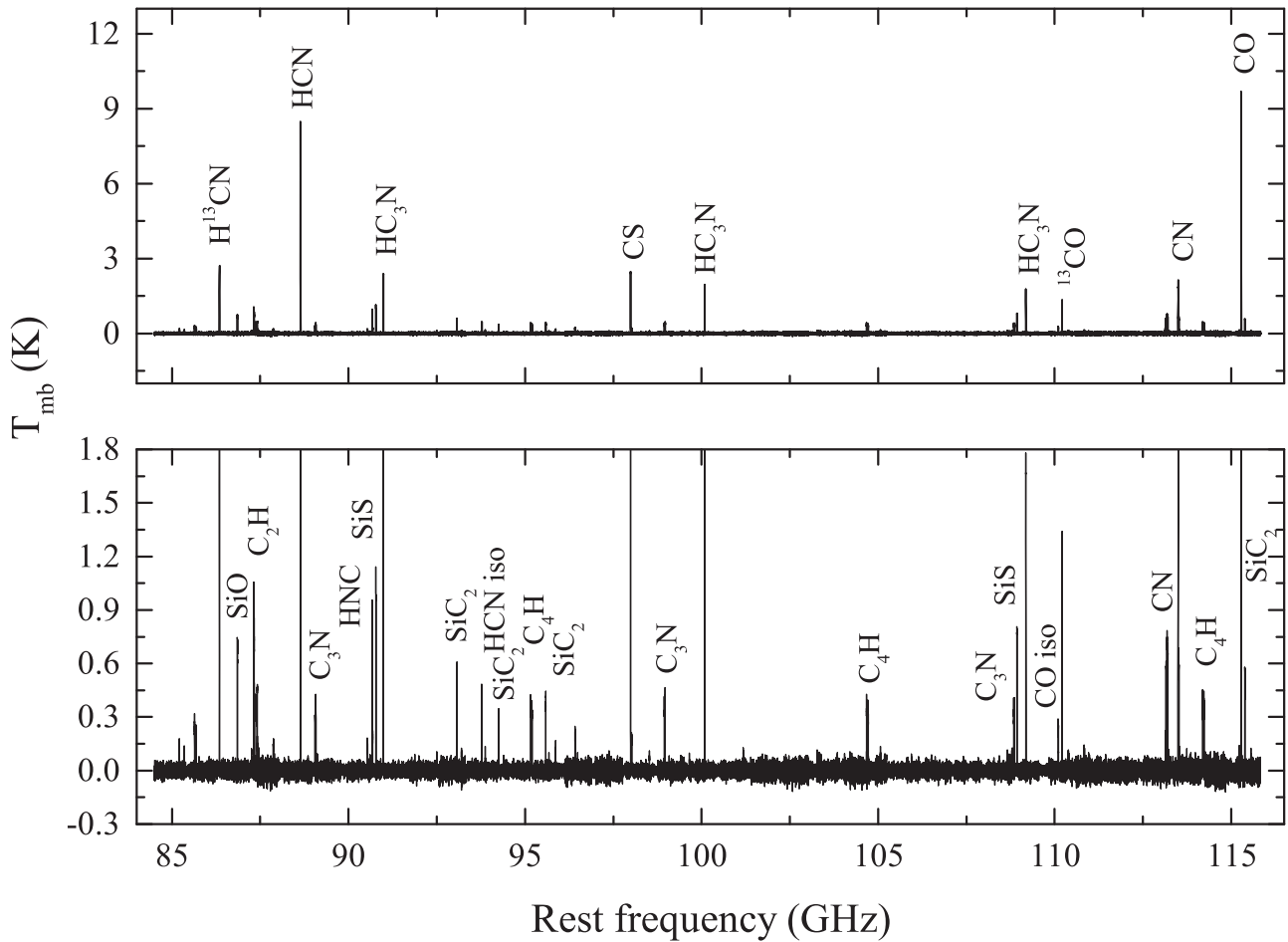
Figure 1. An overall spectral line survey toward IRC+10216 in the 3 mm band by the PMO 13.7 m radio telescope. The rest frequency scale was obtained by adopting a radial velocity of -26.5 km s^{-1}. The X-axis denotes the rest frequency (GHz), and the Y-axis depicts T_{mb} (kelvin). On the upper panel, spectral lines with T_{mb} greater than 1.3 K are marked, while those with T_{mb} greater than 350 mK are marked on the lower panel.

integration times were 1 minute each per scan. The temperature scale is antenna temperature (T_A^*) after correction of atmospheric absorption and ohmic loss. The T_A^* scale is related to the main beam brightness temperature (T_{mb}) via the main beam efficiency (η), i.e., $T_{mb} = T_A^*/\eta$; the value of η is ~ 0.6.[17] The half-power bandwidths (HPBWs) are 51″ and 49″ at 110 and 115 GHz, respectively. The velocity resolution is ~ 0.16–0.17 km s^{-1}. The total observing time of the spectral line survey is about 32.5 hr, which includes overhead due to telescope movement. The pointing accuracy was better than 5″.

The data were reduced using the GILDAS[18] software package, including CLASS and GREG. Linear baseline subtractions were used for all the spectra. Since the edges of the spectral range may have unknown defects, channels closer than 150 MHz to each edge of a spectral window were discarded. Velocity is given relative to the local standard of rest. Except for CO, CS, and HCN, molecular lines were smoothed (combined channels) to improve signal-to-noise ratios (S/Ns) for individual channels. The rms noise of the smoothed spectra is about 0.014 (or ~ 0.135) K in 1.759 (or ~ 0.402) km s^{-1} wide channels for the detected species (or CO, CS, and HCN).

3. Results

3.1. The Overall Survey

Figure 1 presents an overview of the spectral line survey toward IRC+10216 in the λ 3 mm band, which is displayed in consecutive 475 MHz frequency segments with 0.244 MHz spectral resolution in Appendix A. We find 96 transitions, and the identified lines are assigned to 19 different molecular species and their isotopologues. The line identification was performed by using the Jet Propulsion Laboratory[19] (JPL; Pickett et al. 1998), Cologne Database for Molecular Spectroscopy catalogs[20] (CDMS; Müller et al. 2005), and Splatalogue databases[21] as well as the online Lovas line list[22] (Lovas 2004) for astronomical spectroscopy. The local standard of rest radial velocity (V_{lsr}) of -26.5 km s^{-1} is adopted to derive the rest frequency of the observed lines (Zhang et al. 2017). This paper discusses the lines detected with S/N of at least 3 (Fonfría et al. 2014).

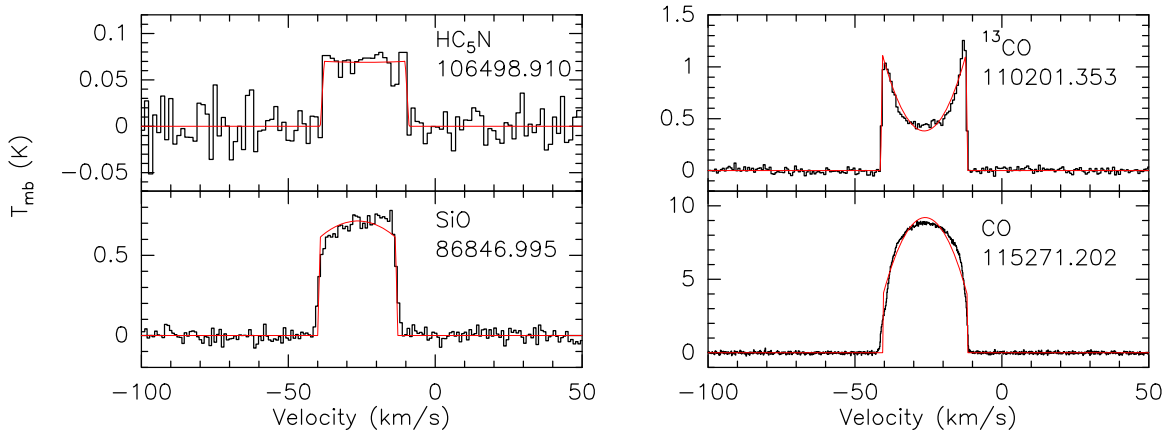We used the SHELL fitting routine in CLASS to fit the spectral line profiles and obtain the relevant parameters

---

[17] http://www.radioast.nsdc.cn/zhuangtaibaogao.php
[18] GILDAS is developed and distributed by the Observatoire de Grenoble and IRAM.

[19] http://spec.jpl.nasa.gov
[20] https://cdms.astro.uni-koeln.de/classic/entries/
[21] https://splatalogue.online/#/advanced
[22] http://www.nist.gov/pml/data/micro/index.cfm

Figure 2. Illustrations of the four typical shapes of the spectral line profiles observed in IRC+10216: flat topped (e.g., HC$_5$H, optically thin, spatially unresolved), double peaked (e.g., ^{13}CO, optically thin, spatially resolved), truncated parabolic (e.g., SiO, optically thick, spatially resolved), and parabolic (e.g., CO, optically thick, spatially unresolved). The solid black line shows the observed spectrum, and the solid red line represents the spectral line profile fitted by the shell function. The rest frequency of separable spectral lines are in MHz, and the molecule's name is displayed in the upper right corner of each panel. All of the detected spectra from this survey are included in Appendix C.

(Gong et al. 2015). The fitted spectral line parameters include peak intensity, integrated intensity, and expansion velocity, defined as the half-width at zero power (Gong et al. 2015; Zhang et al. 2017). For the lines with hyperfine structure (hfs; like HCN, H^{13}CN, etc.), only their primary components are fitted with the routine to obtain their expansion velocities, and the integrated intensity is a sum over all hyperfine components. All detected transitions and the line parameters are listed in Table B1. The rms noise on a main beam brightness temperature ($T_{\rm mb}$) scale is obtained from the statistics in regions free of noticeable spectral lines, and the measurement uncertainty of the integrated intensity given in this work is calculated as the product of the rms noise and the line width (Zhang et al. 2017).

All detected transitions are shown in Figures 2 and C1–C10. To clearly present the spectral line profile and $V_{\rm lsr}$ of each molecule, the X-axis range of the spectral line figure we show varies. For most spectral lines, the velocity range is set from -100 to 50 km s^{-1}, while the velocity ranging from -50 to 0 km s^{-1} is assumed for transitions shown in Figures C1, C4 (except for the top right panel where it extends from -200 to 50 km s^{-1}), and C5 (except for the bottom right panel, where the velocity range is the standard one).

The detected lines include six transitions each for C$_2$H and C$_3$N, eight transitions for l-C$_3$H as well as C$_4$H ($\nu = 0$), seven transitions of C$_4$H ($\nu = 1$), nine transitions for CN as well as HC$_5$N, two transitions each for H^{13}CCCN, SiS, and C$_2$S, three transitions each for HC^{13}CCN, HCC^{13}CN, HNC, HCN, H^{13}CN, CH$_3$CN, and HC$_3$N, one transition for c-C$_3$H$_2$, CO, ^{13}CO, SiO, ^{29}SiO, Si^{34}S, ^{29}SiS, C$_3$S, CS, ^{13}CS, C^{34}S, and MgNC, and four transitions of SiC$_2$.

Table 3 summarizes previous 3 mm observations toward IRC +10216. We checked if the previous work had detected all of the species we identified, or if they had provided all of the necessary information about these species, such as spectral line profile, excitation temperature ($T_{\rm ex}$), and the molecular column density (N) or the fractional abundance (f). Clearly, none of them have provided all of these parameters. Therefore, a detailed complete study of the 3 mm molecules in this famous source is highly desirable. Here, we find that the $J = 13$–12 transition of H^{13}CCCN is detected in IRC+10216 for the first time.

3.2. Typical Spectral Line Profiles

Typically, in the CSEs of AGB stars, there are four types of molecular spectral line profiles: double-peaked, parabolic, flat-topped, and truncated parabolic line shapes (see Figure 2). The different shapes of the observed spectral lines are mainly determined by the optical depth of the transition and the ratio of the angular area of the emitting region to the beam size of the telescope (Zuckerman 1987). Optically thin unresolved and resolved emission lines show flat-topped and double-peaked profiles, while optically thick unresolved and resolved emission lines have parabola and truncated parabola profiles. (Morris et al. 1975; Zuckerman 1987; Habing & Olofsson 2004).

The profiles of the C$_2$H (Johansson et al. 1984), l-C$_3$H, C$_4$H ($\nu = 0$) (Olofsson et al. 1982; Johansson et al. 1984), C$_4$H($\nu = 1$), C$_3$N (Johansson et al. 1984), c-C$_3$H$_2$ (Zhang et al. 2017), ^{13}CO, H^{13}CCCN (Zhang et al. 2017), HC$_5$N (Gong et al. 2015; Zhang et al. 2017), MgNC, CH$_3$CN, HNC, SiC$_2$, ^{13}CS, C^{34}S (Groesbeck et al. 1994), and C$_2$S and C$_3$S emission lines appear to be double peaked or/and flat topped, indicating that they are optically thin. The profiles of the HCN, H^{13}CN, and CO emission lines appear to be parabolic, while the CS line is a truncated parabola profile, which implies that they are all optically thick.

Interestingly, the CN $N = 1$–0, $J = 1/2$–$1/2$, and $F = 1/2$–$1/2$ profile is double peaked, while other $N = 1$–0, $J = 1/2$–$1/2$ hyperfine transitions of CN ($F = 1/2$–$3/2$, $F = 3/2$–$1/2$, $F = 3/2$–$3/2$) show truncated parabolic profiles (see Figure C4). Groesbeck et al. (1994) find that CN ($N = 3$–2) lines have prominent double-peaked profiles indicative of low optical depth.

Zhang et al. (2017) found that HC$_3$N produced a double-peaked profile and was rated to be optically thin. However, we find that the spectral lines of HC$_3$N are truncated parabola (see Figure C6), which indicates that HC$_3$N is at least partially saturated (Olofsson et al. 1982).

Our fitting results for SiO (see Figure 2) showed a truncated parabolic shape, indicating that the line is slightly optically thick. ^{29}SiO shows a double-peaked structure (see Figure C8), which indicates that this molecule is optically thin. Judging from the average profile of the ^{29}SiO and ^{30}SiO lines, Kahane et al. (1988) pointed out that the $J = 2$–1 rotational transition of SiO seems to be optically thick. However, Olofsson et al. (1982) noted that the SiO $J = 2$–1 transition has a flat-topped appearance, albeit that the redshifted emission is slightly

Table 3
Overview of Previous Studies on Molecules Identified within Our Measured λ 3 mm Band toward IRC+10216

No.	Molecule	Rest Freq. (MHz)	Detected?	Spectrum?	T_{ex} Obtained?	N or f[a] Obtained?	References
(1)	HC$_5$N	85,201.346	✓	✓	✓	✓	(1, 2, 3, 4, 5)
(2)	c-C$_3$H$_2$	85,338.906	✓	✓	...	✓	(2, 6, 7)
(3)	C$_4$H	85,634.000	✓	✓	✓	✓	(2, 5, 7, 8)
(4)	C$_4$H	85,672.570	✓	✓	✓	✓	(2, 5, 8)
(5)	^{29}SiO	85,759.188	✓	✓	✓	✓	(2, 9, 10, 11, 12)
(6)	H^{13}CN	86,338.737	✓	✓	...	...	(4, 6, 9, 13)
(7)	H^{13}CN	86,340.176	✓	✓	...	✓	(4, 6, 9, 13, 14, 15, 16)
(8)	H^{13}CN	86,342.255	✓	✓	...	...	(4, 6, 9, 13)
(9)	SiO	86,846.995	✓	✓	✓	✓	(2, 6, 9, 11, 12, 17)
(10)	C$_2$H	87,284.156	✓	✓	✓	✓	(2, 4, 10, 18, 19)
(11)	C$_2$H	87,316.925	✓	✓	✓	✓	(2, 4, 10, 16, 18, 19, 20, 21)
(12)	C$_2$H	87,328.624	✓	✓	✓	✓	(2, 4, 5, 10, 16, 18, 19, 20)
(13)	C$_2$H	87,402.004	✓	✓	✓	✓	(2, 4, 10, 16, 18, 19, 20)
(14)	C$_2$H	87,407.165	✓	✓	✓	✓	(2, 4, 10, 18, 19, 20)
(15)	C$_2$H	87,446.512	✓	✓	✓	✓	(2, 4, 10, 18, 19)
(16)	HC$_5$N	87,863.630	✓	✓	✓	✓	(1, 2, 3, 5, 9)
(17)	H^{13}CCCN	88,166.808	✓	✓	...	...	(2, 3, 4, 9)
(18)	HCN	88,630.416	✓	✓	...	...	(2, 4, 6, 9, 13)
(19)	HCN	88,631.847	✓	✓	✓	✓	(2, 4, 6, 9, 13, 14, 16, 15)
(20)	HCN	88,633.936	✓	✓	...	...	(2, 4, 6, 9, 13, 22)
(21)	C$_3$N	89,045.590	✓	✓	✓	✓	(2, 5, 23, 24)
(22)	C$_3$N	89,064.360	✓	✓	✓	✓	(4, 5, 23, 24)
(23)	^{29}SiS	89,103.720	✓	✓	✓	✓	(4, 10, 11, 12)
(24)	HC$_5$N	90,525.890	✓	✓	✓	✓	(2, 3, 5, 25, 26)
(25)	HC^{13}CCN	90,593.059	✓	✓	...	✓	(2, 4, 6)
(26)	HCC^{13}CN	90,601.791	✓	✓	...	✓	(2, 4, 6)
(27)	HNC	90,663.450	✓	✓	...	...	(2, 4, 6, 9, 27, 28)
(28)	HNC	90,663.574	✓	✓	✓	✓	(2, 4, 6, 9, 16, 21, 27, 28)
(29)	HNC	90,663.656	✓	✓	...	...	(2, 4, 6, 9, 27, 28)
(30)	SiS	90,771.561	✓	✓	✓	✓	(2, 6, 9, 11, 12, 16, 17, 22, 29, 30)
(31)	HC$_3$N	90,978.989	✓	✓	✓	✓	(2, 4, 5, 6, 9 16, 17, 21)
(32)	^{13}CS	92,494.270	✓	✓	✓	✓	(11, 12, 15, 31)
(33)	SiC$_2$	93,063.639	✓	✓	✓	✓	(25, 32, 33, 34, 35)
(34)	HC$_5$N	93,188.123	✓	✓	✓	✓	(3, 5, 36)
(35)	C$_4$H	93,863.300	✓	✓	...	...	(37)
(36)	C$_2$S	93,870.098	✓	✓	✓	✓	(31, 38)
(37)	SiC$_2$	94,245.393	✓	✓	✓	✓	(7, 25, 30, 32, 33, 35)
(38)	C$_4$H	95,150.320	✓	✓	✓	✓	(5, 6, 8, 34)
(39)	C$_4$H	95,188.940	✓	✓	✓	✓	(5, 8, 34)
(40)	SiC$_2$	95,579.381	✓	✓	✓	✓	(25, 32, 33, 35, 39)
(41)	HC$_5$N	95,850.335	✓	✓	✓	✓	(3, 5)
(42)	C^{34}S	96,412.950	✓	✓	✓	✓	(4, 10, 11, 12)
(43)	CS	97,980.953	✓	✓	...	✓	(4, 10, 11, 12, 15, 16, 22, 30, 40, 41)
(44)	l-C$_3$H	97,995.212	✓	✓	✓	✓	(2, 4, 40)
(45)	l-C$_3$H	97,995.951	✓	✓	✓	✓	(2, 4, 6, 40)
(46)	l-C$_3$H	98,011.649	✓	✓	✓	✓	(2, 4, 34, 40)
(47)	l-C$_3$H	98,012.576	✓	✓	✓	✓	(2, 4, 34, 40)
(48)	HC$_5$N	98,512.524	✓	✓	✓	✓	(1, 3, 5)
(49)	C$_3$N	98,940.020	✓	✓	✓	✓	(5, 23, 24, 42)
(50)	C$_3$N	98,958.780	✓	✓	✓	✓	(5, 23, 24, 42)
(51)	HC^{13}CCN	99,651.863	✓	✓	...	...	(7)
(52)	HCC^{13}CN	99,661.471	✓	✓	...	...	(7)
(53)	HC$_3$N	100,076.386	✓	✓	✓	✓	(5, 16)
(54)	HC$_5$N	101,174.677	✓	...	...	...	(5)
(55)	C$_4$H	103,266.081	✓	...	...	...	(37)
(56)	l-C$_3$H	103,319.278	✓	✓	...	...	(37)
(57)	l-C$_3$H	103,319.818	✓	✓	...	...	(37)
(58)	l-C$_3$H	103,372.506	✓	✓	...	...	(37)
(59)	l-C$_3$H	103,373.129	✓	✓	...	...	(37)
(60)	HC$_5$N	103,836.817	✓	...	...	...	(5)
(61)	C$_3$S	104,048.451	✓	✓	✓	✓	(31, 42)
(62)	C$_4$H	104,666.560	✓	✓	✓	✓	(5, 8)
(63)	C$_4$H	104,705.100	✓	✓	✓	✓	(5, 8)

Table 3
(Continued)

No.	Molecule	Rest Freq. (MHz)	Detected?	Spectrum?	T_{ex} Obtained?	N or f[a] Obtained?	References
(64)	C$_4$H	105,838.000	✓	…	…	…	(37)
(65)	Si^{34}S	105,941.503	✓	…	…	…	(11, 12)
(66)	C$_4$H	106,132.800	✓	…	…	…	(37)
(67)	C$_2$S	106,347.740	✓	…	✓	✓	(31)
(68)	HC$_5$N	106,498.910	✓	✓	✓	✓	(3, 5)
(69)	MgNC	107,399.420	✓	✓	✓	✓	(43)
(70)	HC^{13}CCN	108,710.523	✓	…	…	✓	(6)
(71)	HCC^{13}CN	108,721.008	✓	…	…	✓	(6)
(72)	C$_3$N	108,834.270	✓	✓	✓	✓	(2, 5, 6, 22, 23, 24)
(73)	C$_3$N	108,853.020	✓	✓	✓	✓	(2, 5, 22, 23, 24)
(74)	SiS	108,924.297	✓	✓	…	✓	(2, 6, 11, 12, 17, 22, 29, 44)
(75)	HC$_3$N	109,173.638	✓	✓	✓	✓	(2, 5, 6, 9, 15, 16)
(76)	^{13}CO	110,201.354	✓	✓	…	…	(6, 9, 15, 16, 41, 45, 46)
(77)	CH$_3$CN	110,375.049	✓	✓	✓	✓	(7)
(78)	CH$_3$CN	110,381.400	✓	✓	✓	✓	(7)
(79)	CH$_3$CN	110,383.518	✓	✓	✓	✓	(7)
(80)	C$_4$H	112,922.500	✓	…	…	…	(37)
(81)	CN	113,123.337	✓	✓	…	…	(16, 18)
(82)	CN	113,144.192	✓	✓	…	✓	(16, 18)
(83)	CN	113,170.528	✓	✓	…	✓	(16, 18)
(84)	CN	113,191.317	✓	✓	…	✓	(16, 18)
(85)	C$_4$H	113,265.900	✓	✓	…	…	(37, 47)
(86)	CN	113,488.140	✓	✓	…	…	(7, 14, 16, 18)
(87)	CN	113,490.982	✓	✓	…	✓	(6, 14, 16, 18, 41)
(88)	CN	113,499.639	✓	✓	…	…	(5, 14, 16, 18)
(89)	CN	113,508.944	✓	✓	…	…	(14, 16, 18)
(90)	CN	113,520.414	✓	✓	…	…	(14, 16, 18)
(91)	C$_4$H	114,182.510	✓	✓	✓	✓	(5, 8)
(92)	C$_4$H	114,221.040	✓	✓	✓	✓	(5, 8)
(93)	H^{13}CCCN	114,615.021	…	…	…	…	
(94)	C$_4$H	115,216.800	✓	…	…	…	(37)
(95)	CO	115,271.202	✓	✓	✓	✓	(6, 9, 15, 16, 41, 48, 49, 50, 45)
(96)	SiC$_2$	115,382.375	✓	✓	✓	✓	(32, 33, 35, 51)

Notes. Note that in this work we have provided all of the information on all of the species listed here.
Since there exist numerous observations toward IRC+10216, here we only provide a few key references containing molecular spectral line profiles, excitation temperature, and column density, which are (1) Bujarrabal et al. (1981); (2) Johansson et al. (1984); (3) Cernicharo et al. (1986b); (4) Kahane et al. (1988); (5) Agúndez et al. (2017); (6) Nyman et al. (1993); (7) Agúndez et al. (2008b); (8) Guélin et al. (1978); (9) Olofsson et al. (1982); (10) Groesbeck et al. (1994); (11) Agúndez et al. (2012); (12) Velilla Prieto et al. (2019); (13) Morris et al. (1971); (14) Dayal & Bieging (1995); (15) Wannier & Linke (1978); (16) Park et al. (2008); (17) Morris et al. (1975); (18) Truong-Bach et al. (1987); (19) De Beck et al. (2012); (20) Tucker et al. (1974); (21) Bieging & Rieu (1988); (22) Henkel et al. (1985); (23) Guélin & Thaddeus (1977); (24) Thaddeus et al. (2008); (25) Cernicharo et al. (1986c); (26) Agúndez et al. (2014); (27) Brown et al. (1976); (28) Daniel et al. (2012); (29) Sahai et al. (1984); (30) Lucas et al. (1995); (31) Cernicharo et al. (1987a); (32) Thaddeus et al. (1984); (33) Snyder et al. (1985); (34) Cernicharo et al. (1986a); (35) Cernicharo et al. (2018); (36) Turner et al. (1994); (37) Yamamoto et al. (1987); (38) Cernicharo et al. (2019a); (39) Guélin et al. (1990); (40) Thaddeus et al. (1985a); (41) Wilson et al. (1971); (42) Cernicharo & Guélin (1987); (43) Guélin et al. (1986); (44) Bieging & Nguyen-Quang-Rieu (1989); (45) Kuiper et al. (1976); (46) Knapp & Chang (1985); (47) Cernicharo et al. (2019b); (48) Solomon et al. (1971); (49) Fong et al. (2003); (50) Fong et al. (2006); (51) Tenenbaum et al. (2006).
[a] N and f depict the total column density and fractional abundance of the molecular species.

stronger than the blueshifted emission and resembles the typical rectangular line profile of an unresolved, optically thin molecular shell with a constant velocity gas flow. On the other hand, the spectral lines of the SiO $J = 2–1$ to $J = 8–7$ transitions observed by Agúndez et al. (2012) have a slight double-peaked structure, but the spectral line profiles simulated by them using radiative transfer are parabolic. This may indicate that the envelope of SiO is slightly unresolved (Agúndez et al. 2012), or more likely that an enhanced density shell should be considered in the IRC+10216 model (see De Beck et al. 2012 and Daniel et al. 2012), or that more infrared pumping should be added in the model (Agúndez et al. 2012).

The SiS $J = 6–5$ spectrum (see Figure C9) shows an optically thick emission with a parabolic shape. This result is consistent with observations by Johansson et al. (1984) and Fonfría et al. (2018). Johansson et al. (1984) and Olofsson et al. (1982) speculated that the SiS $J = 5–4$ double-peaked profile might be due to maser-enhanced line wings. Fonfría et al. (2018) find through monitoring of the SiS $J = 5–4$ and SiS $J = 6–5$ lines in IRC+10216 that the SiS $J = 5–4$ spectral line shows narrow peaks at high expansion velocities, which vary strongly with the pulsation of the star, while the remaining line profile is approximately constant over the stellar pulsation period. On the contrary, SiS $J = 6–5$ shows neither narrow

peaks nor a constant profile over the stellar period at high expansion velocities.

Apparently, the line shape of a certain transition of a molecule could be different when being observed by different telescopes. We compared and summarized all of the line profiles related to this work in Appendix G.

4. Discussion

4.1. Rotation Diagram Analysis

4.1.1. Molecular Excitation Temperature and Column Density

Assuming local thermal equilibrium (LTE), the column densities (N_{tot}) and excitation temperatures of detected lines were derived by using the following equation:

$$\ln \frac{N_u}{g_u} = \ln \frac{3kW}{8\pi^3 \nu S \mu^2} = \ln \frac{N_{tot}}{Q(T_{ex})} - \frac{E_u}{kT_{ex}}, \quad (1)$$

where, N_u and g_u are the population and statistical weights of the upper level, k is the Boltzmann constant, $W = \int T_R dv$ is the integral of the source brightness temperature (T_R) over the line's velocity range, ν is the rest frequency of the line, S is the transition's intrinsic strength, μ is the permanent dipole moment, and Q is the partition function, which is related to T_{ex}, and E_u, the excitation energy of the upper level. The values of Q, E_u/k, and $S\mu^2$ are taken from the Splatalogue spectral line catalogs.

In actual astronomical measurements, the observed molecules often do not fill the telescope beam, so it is necessary to consider the correction of the main beam brightness temperature and source brightness temperature by using the beam dilution correction of the molecular source (η_{BD}).

The relationship between the main beam brightness temperature and the source brightness temperature is as follows:

$$T_R = \frac{T_{mb}}{\eta_{BD}}, \quad (2)$$

where

$$\eta_{BD} = \frac{\theta_s^2}{\theta_s^2 + \theta_{beam}^2}. \quad (3)$$

Here, η_{BD} is the beam dilution factor or beam filling factor, θ_{beam} is the HPBW of the antenna, and θ_s is the source size. In our calculations, η_{BD} of all the identified unblended molecular lines and the supplemented data are calculated via Equation (3), while data from the blended lines are excluded. When a molecule's excitation temperature is obtained using rotational diagrams, it is required that at least two unblended transition lines of the same molecule, with significant upper energy differences have been observed. Unfortunately, this does not hold for all our detections. We only observed one line in the case of CS, $C^{34}S$, ^{13}CS, C_3S, CO, ^{13}CO, SiO, ^{29}SiS, $Si^{34}S$, MgNC, and c-C_3H_2. For molecules such as HNC, HCN, $H^{13}CN$, and CH_3CN, we only observed the hfs of one rotational transition. Because the frequency interval of these fine structure lines is too small, their spectral lines are blended. For CN, SiC_2, l-C_3H, C_3N, $H^{13}CCCN$, and C_2H, at least two transitions have been observed, but the energy level spacing of these lines is minimal. It has been reported that the excitation temperatures of HC_3N and HC_5N are related to their energy level transitions (Bell et al. 1992b). Therefore, to calculate these

molecules' excitation temperature and column density, we supplemented our data with spectral line surveys of other research groups. The additional frequency ranges with observational data include 13.3–18.5 GHz (Zhang et al. 2017), 17.8–26.3 GHz (Gong et al. 2015), 28–50 GHz (Kawaguchi et al. 1995), 129.0–172.5 GHz (Cernicharo et al. 2000), 131.2–160.3 GHz (He et al. 2008), 219.5–267.5 GHz (He et al. 2008), and 330–358 GHz (Groesbeck et al. 1994). In addition, supplementary data for HNC come from Daniel et al. (2012). For CS, ^{13}CS, $C^{34}S$, SiO, ^{29}SiO, SiS, ^{29}SiS, and $Si^{34}S$, we have also supplemented the data using the observations of Agúndez et al. (2012). Data for HCN from Nyman et al. (1993) are also included. We processed the data of Groesbeck et al. (1994), Kawaguchi et al. (1995), He et al. (2008), Gong et al. (2015), and Zhang et al. (2017), calculating the uncertainty of the integrated intensity as the product of the rms noise and the line width. For other supplementary data, we adopted the integrated intensity and uncertainty values as reported in the original literature. To derive the excitation temperature and column density of a molecule, one needs to know the spatial distribution of the molecular source or the source size. Agúndez et al. (2017) find that the observational results of HC_5N ($J = 32$–31 to $J = 43$–42) with the Atacama Large Millimeter/submillimeter Array (ALMA) do not show a radial shift in the emission peak between low-J and high-J lines as might reasonably be expected, and all emission distributions of HC_5N appear quite similar. The same is found for HC_3N, C_4H, and C_3N in the λ 3 mm band (Agúndez et al. 2017). The source size employed in this work is taken from previous high-resolution maps in the λ 3 mm band of the relevant molecule. If such a study does not exist, the source size is obtained from chemically related species (He et al. 2008; Gong et al. 2015). The employed sizes of the identified molecules, θ_s, and the references are listed in Table 4.

We used the least squares method to perform the linear fitting for the rotational diagrams of these molecules and their isotopes. The fitting results are shown in Figures E1 and E2. According to the rotational diagrams, it can be seen that most spectra have large dispersion, especially CS, ^{13}CS, and $C^{34}S$. The derived excitation temperatures, column densities, and the molecular fractional abundances relative to H_2 (see Section 4.2) together with observational results from the literature (including line surveys in the 18, 13, 8, 2, and 1.3 mm bands), are summarized in Table 4. The excitation temperatures of the molecules range from 5.3–73.4 K and their column densities range from 3.27×10^{13} to 4.15×10^{17} cm^{-2}.

Compared to observational results in the literature, the molecules with large differences in excitation temperatures include l-C_3H, C_4H ($\nu = 0$), C_4H ($\nu = 1$), HC_5N, c-C_3H_2, C_2S, and CH_3CN. We also find that column densities, except for C_4H, HCN, and CH_3CN, agree with previously published observational results.

The excitation temperatures of l-C_3H in the $^2\Pi_{1/2}$ and $^2\Pi_{3/2}$ states are 8.5 K (Thaddeus et al. 1985a; Kawaguchi et al. 1995) and 52 K (Thaddeus et al. 1985a), respectively. Thaddeus et al. (1985a) pointed out that the low excitation temperature (8.5 K) of the $^2\Pi_{1/2}$ state of l-C_3H is due to rapid radiative decay, while the high excitation temperature (52 K) of the $^2\Pi_{3/2}$ state is a consequence of the fact that interconnecting far-IR radiative transitions are only weakly permitted. When we adopt an l-C_3H diameter of 30″, the excitation temperatures of the $^2\Pi_{1/2}$

Table 4
Summary of Column Density (N), Excitation Temperature (T_{ex}), Source Size, (θ_s) and Fractional Abundance Relative to H_2 ($f = N/N_{H_2}$), of the Detected Species in This Work and the Literature

Molecule	This Work					Lit. Observational		
	T_{ex} (K)	N (cm^{-2})	f	θ_s (arcsec)	References (for θ_s)	T_{ex} (K)	N (cm^{-2})	References (for T_{ex}, N)
C_2H	17.0 (2.0)	8.14 (2.29) × 10^{15}	3.37 × 10^{-6}	32	(1)	16	4.6 × 10^{15}	(11)
l-C_3H	14.3 (0.9)	1.25 (0.22) × 10^{14}	4.84 × 10^{-8}	30	(2)	8.5	5.6 × 10^{13}	(11)
						25 (5)	1.32 (0.35) × 10^{14}	(12)
C_4H ($\nu = 0$)	45.9 (3.1)	2.75 (0.36) × 10^{15}	1.07 × 10^{-6}	30	(2)	18.5 (7.6)	2.4 (0.2) × 10^{15}	(13)
						15	2.4 × 10^{15}	(11)
						4.9 (0.6)	1.84 (0.25) × 10^{14}	(14)
						53 (5)	8.1 (1.1) × 10^{15}	(12)
C_4H ($\nu = 1$)	64.3 (2.8)	3.66 (0.74) × 10^{16}	1.42 × 10^{-5}	30	(3)	53 (4)	5.9 (2.1) × 10^{15}	(12)
						10 (5)	6.6 (2.0) × 10^{13}	(14)
CN	9.8 (2.0)	>1.08 (0.42) × 10^{15}	>1.4 × 10^{-6}	100	(4)	8.7	6.2 × 10^{14}	(15)
C_3N	27.6 (1.9)	4.25 (0.81) × 10^{14}	1.98 × 10^{-7}	36	(5)	20.2 (1.1)	3.1 (0.3) × 10^{14}	(13)
						15	4.1 × 10^{14}	(11)
HC_3N	21.2 (0.5)	>1.18 (0.08) × 10^{15}	>4.59 × 10^{-7}	30	(6)	27.2 (19.4)	1.94 (0.21) × 10^{15}	(16)
						24.7 (18.5)	1.4 (0.2) × 10^{15}	(13)
						26	1.7 × 10^{15}	(11)
						28 (1)	8.0 (1.5) × 10^{14}	(12)
$H^{13}CCCN$	15.9 (0.9)	4.38 (0.88) × 10^{13}	1.70 × 10^{-8}	30	(3)	18.7 (3.3)	3.25 (1.46) × 10^{13}	(16)
						27	2 × 10^{13}	(12)
HC_5N	23.7 (0.5)	5.41 (0.56) × 10^{14}	2.10 × 10^{-7}	30	(6)	13.6 (2.1)	5.47 (0.77) × 10^{14}	(16)
						18.8 (1.3)	4.6 (0.2) × 10^{14}	(13)
						27 (5)	2.7 (0.2) × 10^{14}	(11)
						10.1 (0.6)	4.2 (0.4) × 10^{14}	(14)
HNC	12.1 (0.1)	1.11 (0.08) × 10^{14}	5.76 × 10^{-8}	40	(7)	…	…	
HCN	16.0 (1.4)	>7.36 (0.92) × 10^{14}	>6.10 × 10^{-7}	64	(4)	…	2.8 × 10^{16}	(15)
$H^{13}CN$	20.8 (5.5)	>3.92 (1.17) × 10^{14}	>2.84 × 10^{-7}	56	(4)	…	2.8 × 10^{14}	(15)
CO	31.9 (10.9)	>4.03 (1.51) × 10^{17}	>1.04 × 10^{-3}	200	(8)	…	2.0 × 10^{18}	(15)
^{13}CO	30.2 (5.4)	4.12 (0.86) × 10^{16}	1.07 × 10^{-4}	200	(3)	17	5.0 × 10^{16}	(15)
c-C_3H_2 (ortho)	5.3 (0.2)	1.14 (0.15) × 10^{14}	4.44 × 10^{-8}	30	(3)	5.7 (1.4)	4.82 (4.14) × 10^{14}	(12)
c-C_3H_2 (para)	5.7 (0.9)	8.02 (4.54) × 10^{13}	3.11 × 10^{-8}	30	(3)	8 (6)	1.22 (2.03) × 10^{14}	(12)
						6.1 (2.8)	1.39 (1.07) × 10^{14}	(16)
						5.5 (0.6)	2.1 (0.4) × 10^{14}	(13)
						20	1.6 × 10^{13}	(11)
SiO	29.2 (3.9)	>4.84 (1.13) × 10^{14}	>1.38 × 10^{-7}	22	(9)	29	5.4 × 10^{14}	(11)
						29	2.1 × 10^{14}	(15)
^{29}SiO	27.7 (3.5)	3.95 (0.91) × 10^{13}	1.13 × 10^{-8}	22	(9)	29	2.5 × 10^{13}	(11)
						29	1.9 × 10^{13}	(15)
^{29}SiS	64.8 (4.6)	4.39 (0.75) × 10^{14}	1.25 × 10^{-7}	22	(9)	85	2.1 × 10^{14}	(15)
$Si^{34}S$	72.5 (5.2)	3.35 (0.59) × 10^{14}	9.54 × 10^{-8}	22	(9)	79	1.8 × 10^{14}	(15)
SiS	73.4 (11.3)	>5.86 (1.74) × 10^{15}	>1.70 × 10^{-6}	22	(9)	70	4.7 × 10^{15}	(11)
						70	3 × 10^{15}	(15)
CS	22.9 (4.3)	>1.57 (0.46) × 10^{15}	>8.12 × 10^{-7}	40	(9)	28	5.9 × 10^{15}	(11)
							3.0 × 10^{15}	(15)
^{13}CS	51.4 (15.8)	8.09 (2.80) × 10^{13}	4.19 × 10^{-8}	40	(9)	…	…	
$C^{34}S$	26.1 (3.3)	1.47 (0.26) × 10^{14}	7.63 × 10^{-8}	40	(9)	28	1.5 × 10^{14}	(15)
C_2S	11.2 (1.2)	1.59 (0.73) × 10^{14}	8.22 × 10^{-8}	40	(3)	39.2 (135.3)	2.3 (0.8) × 10^{14}	(13)
						14	1.5 × 10^{14}	(11)
						7.9 (1.1)	4.0 (0.7) × 10^{13}	(14)
C_3S	34.0 (1.2)	3.27 (0.16) × 10^{13}	1.70 × 10^{-8}	40	(3)	20.4 (13.7)	2.2 (0.4) × 10^{13}	(13)
						33	4.9 × 10^{13}	(11)
						23.6 (96.85)	2.58 (3.60) × 10^{13}	(14)
MgNC	18.9 (1.2)	3.20 (0.51) × 10^{13}	1.24 × 10^{-8}	30	(2)	25.8 (54.9)	3.9 (1.5) × 10^{13}	(13)
						15	2.5 × 10^{13}	(11)
						8.6	7.8 × 10^{13}	(12)
CH_3CN	37.4 (6.4)	6.81 (3.51) × 10^{13}	2.64 × 10^{-8}	30	(3)	16	6 × 10^{12}	(11, 17)
						35 (4)	2.6 (0.6) × 10^{13}	(12)
SiC_2	34.9 (5.5)	1.41 (0.34) × 10^{15}	4.92 × 10^{-7}	27	(10)	40.1 (36.2)	1.87 (1.34) × 10^{15}	(16)
						31.8 (0.9)	1.2 (0.0) × 10^{15}	(13)

Note. The derivation of the fractional abundance is discussed in Section 4.2. The values in parentheses in this table are the 1σ errors associated with the fits to our rotational diagrams. The corresponding references are (1) Guélin et al. (1999); (2) Guélin et al. (1993); (3) The source size assumed to be the same as its main isotopomer or obtained from chemically related species (He et al. (2008); Gong et al. (2015)); (4) Dayal & Bieging (1995); (5) Bieging & Tafalla (1993); (6) Keller et al. (2015); (7) Guélin et al. (1997); (8) Fong et al. (2006); (9) Velilla Prieto et al. (2019); (10) Lucas et al. (1995); (11) Kawaguchi et al. (1995); (12) He et al. (2008); (13) Gong et al. (2015); (14) Pardo et al. (2022); (15) Groesbeck et al. (1994); (16) Zhang et al. (2017); (17) Guélin & Cernicharo (1991).

and $^2\Pi_{3/2}$ states of l-C_3H are 27.4 ± 9.3 and 14.2 ± 1.7 K, respectively.

The excitation temperature of C_4H ($\nu = 0$) obtained in our work is 45.9 ± 3.1 K, and the excitation temperature of C_4H deduced by Avery et al. (1992) is 48 ± 4 K. Comparing the excitation temperatures and column densities in Table 4, we find that the excitation temperatures derived by others are lower than those derived by us except for that of Avery et al. (1992) and He et al. (2008). For Kawaguchi et al. (1995), and Gong et al. (2015), the difference even amounts to a factor of 2. Pardo et al. (2022) derive both the lowest excitation temperature, 4.9 ± 0.6 K, and column density, $(1.84 \pm 0.25) \times 10^{14}$ cm^{-2}, the latter about an order of magnitude lower than the other values. The excitation temperatures and column densities of the vibrationally excited C_4H ($\nu = 1$) derived by us and He et al. (2008) are obviously much larger than those derived by Pardo et al. (2022). In contrast, Pardo et al. (2022) observed low-J lines of C_4H ($\nu = 1$), which trace the cold component of the gas (see Appendix F for a detailed discussion), resulting in a lower excitation temperature. Although they also used a rotational diagram to derive the excitation temperature and column density of C_4H ($\nu = 1$), they did not consider the effect of the beam dilution factor. The large excitation temperatures and column densities derived for the $\nu = 0$ and $\nu = 1$ states of C_4H indicate that infrared pumping could be very efficient (Avery et al. 1992; He et al. 2008).

The excitation temperature of HC_5N obtained by our rotational diagram analysis is close to that of Kawaguchi et al. (1995), but more than twice that of Pardo et al. (2022). In fact, the excitation temperatures of HC_5N are stratified (see Appendix F for a detailed discussion). The excitation temperature of HC_5N obtained by us is the result of fitting multiple rotational transitions, including low and high rotational transitions, which may result in our excitation temperature being close to the one from Kawaguchi et al. (1995). Kawaguchi et al. (1995) derived a higher excitation temperature than Pardo et al. (2022), likely because the latter did not consider the beam dilution factor. Bell et al. (1992b) pointed out that the moderately high excitation temperature of HC_5N, 25 K, is probably due to the influence of infrared excitation. Warm HC_3N ($T_{ex} = 48$ K) and warm HC_5N ($T_{ex} = 35$ K) in the CSE of IRC+10216 may indicate that the excitation is almost entirely due to infrared radiation (Bell 1993).

For ^{13}CO, the excitation temperature and column density obtained by us are consistent with the results of Groesbeck et al. (1994). The column density of CO with opacity corrections obtained by Groesbeck et al. (1994) is about five times larger than our value. Our value of N (CO) in Table 4 is derived from a rotation diagram and is a lower limit as CO is optically thick.

Our HCN column density is much different from that calculated by Groesbeck et al. (1994). Our column density of $H^{13}CN$ is slightly larger than their value, but our value for N (HCN) is only 2.6% of theirs. They derived their value by first using the rotation diagram method for $HC^{15}N$ to obtain T_{ex} and N ($HC^{15}N$). Using a $[^{12}C]/[^{13}C]$ ratio of 44 (Kahane et al. 1988; Cernicharo et al. 1991c) and a $[^{14}N]/[^{15}N] = 4000$ (Kahane et al. 1988), they derived N (HCN) and N ($H^{13}CN$). We detected $HC^{15}N$ with an S/N of less than 3, so our observations of HCN and $H^{13}CN$, which are both optically thick, give lower limits to their column densities in Table 4.

Similarly, using the rotation diagram method, Qiu et al. (2022) derived the column density of HCN in C-rich post-AGB star CRL 2688, and they found that this molecule exhibits a much lower observed abundance, which could be attributed to the effect of optical depth.

For CS, Groesbeck et al. (1994) used the same isotopic rotational diagram method to derive its column density using observations of $C^{34}S$ and a $[^{32}S]/[^{34}S]$ ratio of 20.2, derived by Kahane et al. (1988) from $Si^{32}S$ and $Si^{34}S$. We used the same method and our determination of N ($C^{34}S$) to derive N(CS) $= 3.0 \times 10^{15}$ cm^{-2}, agreeing with the value derived by Groesbeck et al. (1994). The excitation temperature of C_2S derived by us is in good agreement with that obtained by Kawaguchi et al. (1995), but the excitation temperature derived by Gong et al. (2015) is three times that of ours. In the work of Gong et al. (2015), the uncertainty in the C_2S excitation temperature is large because the C_2S transitions only cover a narrow energy range. We find that the excitation temperature of C_3S is 3 times that of C_2S. Agúndez et al. (2014) find that the rotational temperature of C_3S is more than twice that of C_2S, which points to differences in the excitation and may indicate that radiative pumping to vibrationally excited states plays an important role in the case of C_3S (Agúndez et al. 2008b).

In thermal equilibrium, ortho-to-para ratios (OPRs) for species containing two protons with parallel and antiparallel nuclear spins range from their statistical weight limit of 3:1 at high temperatures ($T \geqslant 30$ K) to infinity or zero as the temperature decreases, depending on the symmetry of the rotational and electronic wave functions (Decin et al. 2010; Khouri et al. 2014; Le Gal et al. 2017; Chapovsky 2021; Tsuge et al. 2021). The statistical OPR of c-C_3H_2 derived by He et al. (2008) is approximately 4 (3.95 ± 3.16) while we derived a ratio of 1.42 ± 0.58, consistent with the result estimated by Gong et al. (2015). However, compared to He et al. (2008) and Gong et al. (2015), we have collected and employed more data, and the excitation temperatures (less than 10 K) of para and ortho-c-C_3H_2 are fitted independently. The amounts of ortho-c-C_3H_2 and para-c-C_3H_2 formed are influenced by the OPR of H_2 and by ion–neutral reactions of C_3H_2 with H^+ and H_3^+ that can exchange protons with it. Both Park et al. (2006) and Morisawa et al. (2006) have observed and modeled the OPR of c-C_3H_2 in the dark cloud TMC-1. The latter authors show that this OPR is dependent on the age of the cloud as abundances of species change with time. The situation in IRC +10216 is in part simpler since the OPR in H_2 is likely to be 3 since it forms at high temperature and its flow time through the envelope is too short to change it to any extent. On the other hand, the changing physical conditions of temperature and density, ion abundances, and collision times in the outflow add complexity to the state selective chemistry that ultimately sets the OPR of molecules such as c-C_3H_2 that form in the outer envelope. A detailed study of the ortho–para chemistry of c-C_3H_2 in the CSE is needed to understand the observed ratio.

For SiC_2, we have not added more data. Avery et al. (1992) carefully studied transitions with upper-level energies of 10–300 K and later He et al. (2008) those with values in the range of 20–200 K. The excitation temperature and column density of SiC_2 obtained by us agree with the observed results collected in Table 4.

For the column density of CH_3CN, the result we obtained is in good agreement with that of Agúndez et al. (2008b, 2015) and He et al. (2008), but it is 1 order of magnitude higher than
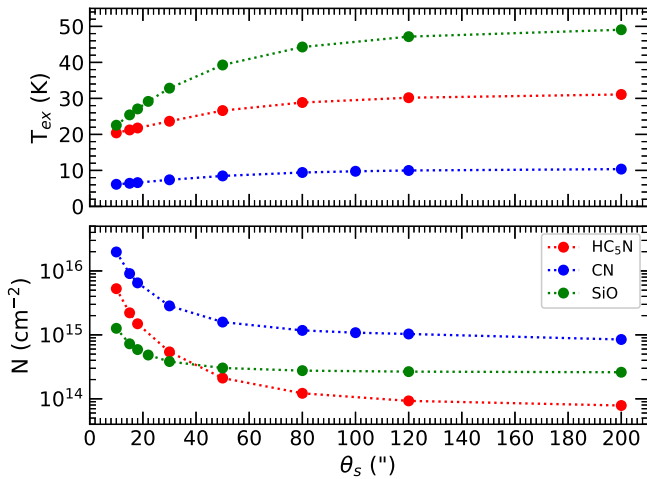
Figure 3. Illustrations for the impact of the employed source size (θ_s) on the calculated excitation temperature (T_{ex}) and column density (N) of HC$_5$N (in red), CN (in blue), and SiO (in green).

that estimated by Kawaguchi et al. (1995). Unfortunately, we are unable to provide any insight into why we have a larger column density than that in Kawaguchi et al. (1995). Kawaguchi's values are actually taken from Guélin & Cernicharo (1991). However, these authors simply give the values in the text of the article and give no information on how these were derived.

We have discussed all spectral lines with S/N of at least 3. Spectral lines whose S/N are between 3 and 5 will affect the calculated results of molecular excitation temperature and column density (Gong et al. 2015). Moreover, different transitions of the same molecule have different source sizes (He et al. 2008). We neglected this factor in the calculations of the molecules' excitation temperature and column density given the lack of available high-resolution data and detailed radiative transfer modeling, including radiative pumping, which could allow one to determine the radial extent of the observed transitions. In addition, significant uncertainties will arise when one deals with the optically thick lines by employing the rotational diagram method. These factors will cause uncertainties in the observationally deduced excitation temperature and column density of the molecules.

4.1.2. Impact of the Source Size on Molecular Excitation Temperature and Column Density

In order to try to understand the effect of the influence of source size on T_{ex} and column density, we use different source sizes (10″, 15″, 18″, 30″, 50″, 80″, 120″, and 200″) for all molecules for which we determine these quantities through the rotational diagram method. It is found that as source size increases so do the excitation temperatures, while column densities decrease. Figure 3 shows the results for CN, HC$_5$N, and SiO. Molecular column densities decrease rapidly between source sizes of 10″ and 50″. The excitation temperatures of molecules vary by a factor of 2, while column densities vary by up to 3 orders of magnitude.

4.2. Observationally Deduced Fractional Abundances

Once the column density of H$_2$ is known, the molecular fractional abundances relative to H$_2$ can be obtained. The beam-averaged H$_2$ column density (N(H$_2$)) can be calculated

from the mass-loss rate via the formula (Gong et al. 2015)

$$N_{H_2} = \frac{\dot{M}R/V_{exp}}{\pi R^2 m_{H_2}} = \frac{\dot{M}}{\pi R V_{exp} \mu m_H}, \qquad (4)$$

where $\dot{M}$, R, V_{exp}, and m_H are the mass-loss rate, the radius of the molecular emission, expansion velocity, and the mass of a hydrogen atom, respectively. For IRC+10216, $\dot{M}$ is $2 \times 10^{-5} M_\odot$ yr^{-1} (Crosas & Menten 1997; Menten et al. 2012); V_{exp} is 14.5 km s^{-1} (Cernicharo et al. 2000); and μ is 2.3 amu (Massalkhi et al. 2018). According to Equation (4), the beam-averaged H$_2$ column density varies with radius (the location of the molecular emission region in the CSE). Due to the large differences in the observed sizes of molecules (e.g., the emission size of CO is over 100″ (Fong et al. 2006), while that of HC$_3$N is about 15″ (Keller et al. 2015). N(H$_2$) obtained at different radii can be quite different (up to an order of magnitude; Gong et al. 2015). We thus calculated the beam-averaged H$_2$ column density at different radii to obtain the molecular fractional abundances relative to H$_2$.

The observationally deduced molecular abundance relative to H$_2$, along with the beam-averaged H$_2$ column density that varies with radius, are summarized in Table 4 and plotted in Figure 4. Here, $f(X) = N(X)/N_R(H_2)$, where $N(X)$ depicts the total column density of the species (X), and $N_R(H_2)$ represents the beam-averaged H$_2$ column density at radius R. For those parent species that peak on the central star, the corresponding $N_R(H_2)$ values are calculated at the maximum emission radii of these species. In the case of daughter species that are distributed in a shell-like structure around the central star, $N_R(H_2)$ is calculated at the peak emission radii of the molecules.

It is found that in IRC+10216, the fractional abundances of the majority of detected species are between 10^{-8} and 10^{-6} in the λ 3 mm wavelength band. Some parent species, however, are more abundant. Agúndez et al. (2012) used the large-velocity gradient radiative transfer model to deduce the fractional abundances of CS, SiO, SiS, and CO, which are 7×10^{-7}, 1.8×10^{-7}, 1.3×10^{-6}, and 6×10^{-4}, respectively. These results are very close to our observational results.

4.3. Updated CSE Model

Good astrochemical modeling results are valuable in explaining, comparing with, and creating observations. As one of the best-observed *molecular factories* in space, IRC+10216 has frequently been modeled for various purposes, e.g., Millar et al. (2000), Agúndez & Cernicharo (2006), Cordiner & Millar (2009), Li et al. (2014), Agúndez et al. (2017), Van de Sande & Millar (2019, 2022), Millar (2020), Van de Sande et al. (2021), and Reach et al. (2022). We employ the CSE model described in Li et al. (2014), with an update of the initial fractional abundances of several parent species listed in Table 5. Unless stated elsewhere, the assumptions and parameters are the same as those described in the model of Li et al. (2014), which accurately calculates the photodissociation of CO and N$_2$ (the two most abundant molecules after H$_2$) in the full 3D spherical geometry with isotropic incident radiation calculated by the Draine (1978) radiation field. Initially, parent species are injected at a radius of $r_i = 1 \times 10^{15}$ cm, where the molecular hydrogen number density is $n_{H_2} = 1.3 \times 10^7$ cm^{-3}, the visual extinction is $A_V = 13.8$ mag, and the kinetic temperature of the gas is $T = 575$ K. The final radius of the CSE is set at $r_f = 2 \times 10^{17}$ cm, where the gas density
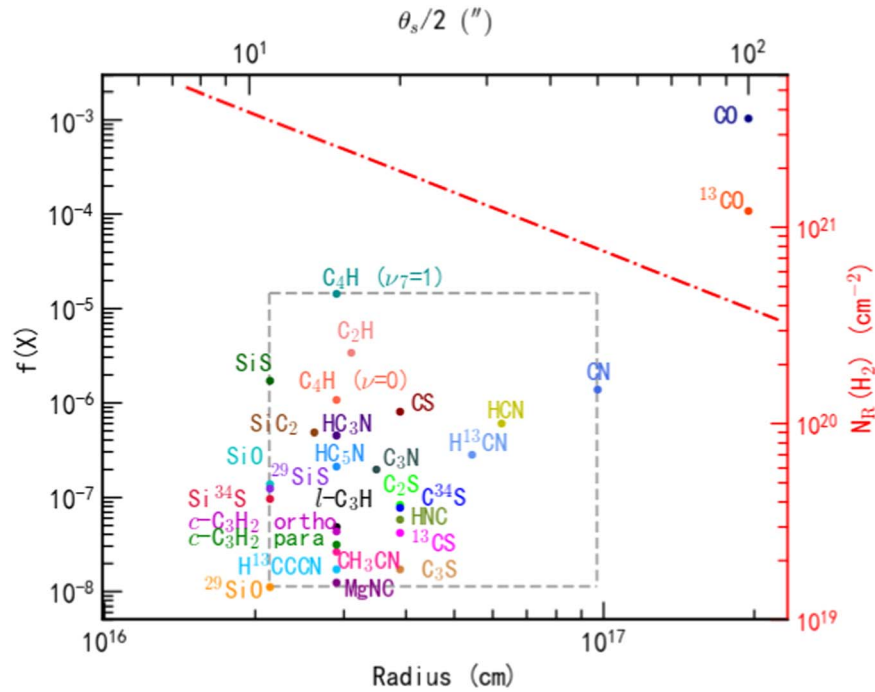
Figure 4. Observationally deduced fractional abundances (f), relative to H_2, of all the λ 3 mm band detected species (X) toward IRC+10216 by the PMO 13.7 m telescope, as a function of radius (R). In the plot, $f(X) = N(X)/N_R(H_2)$, where $N(X)$ depict the total column density of the species (X), and $N_R(H_2)$ (the red dashed–dotted line) represents the beam-averaged H_2 column density at radius R. Except for CO and ^{13}CO, the detected molecules are located within the area marked by the gray-dashed lines.

Table 5
Initial Abundances of Parent Species Relative to H_2, Updated from the CSE Model for IRC+10216 (Li et al. 2014)

Species	Abundance	Species	Abundance
N_2	4.0×10^{-5}	SiS	1.7×10^{-6a}
NH_3	6.0×10^{-8}	CH_4	3.5×10^{-6}
HCN	2.0×10^{-5}	H_2O	2.6×10^{-6}
He	1.7×10^{-1}	PN	3.0×10^{-10}
HF	8.0×10^{-9}	C_2H_4	2.0×10^{-8}
C_2H_2	8.0×10^{-5}	SiH_4	2.2×10^{-7}
CO	1.0×10^{-3a}	HCl	1.0×10^{-7}
H_2S	4.0×10^{-9}	HCP	2.5×10^{-8}
CS	8.1×10^{-7a}	SiC_2	4.9×10^{-7a}
SiO	1.4×10^{-7a}	...	...

Note.
[a] The observationally deduced abundance from this work.

decreases to $n_{H_2} = 26$ cm^{-3}, with $T = 10$ K and $A_V = 0.02$ mag. In the calculations, the mass-loss rate of the star is $1.5 \times 10^{-5} M_\odot$ yr^{-1} and the outflow expansion velocity is 14.5 km s^{-1}. The gas-phase reaction network of the UMIST database for astrochemistry 2012 (McElroy et al. 2013) is employed. Reasonably good agreements are found between the simulated and observed column densities (within an order of magnitude) for most of the detected species ($>70\%$), as summarized in Table 1.

4.4. Isotopic Ratios

Isotopic ratios are closely related to the physical conditions in the star's core where the isotopes are formed. Therefore, isotopic ratios provide information on understanding the

nucleosynthesis and the Galactic chemical evolution as well as the abundances of the interstellar medium (Kahane et al. 1988; Wilson & Rood 1994; Herwig 2005; Peng et al. 2013). AGB stars play an important role in the chemical evolution of galaxies. Thermal pulsing on the AGB creates a convective envelope, which transfers the products of He-shell burning (light elements, such as C, N, and F) and the elements produced by the slow neutron-capture process (s-process) (half of the elements heavier than Fe) to the stellar surface through the third dredge-up. This alters the composition (isotopic ratios) of the envelope (Busso et al. 1999; Herwig 2005; Cristallo et al. 2009; Zhang et al. 2013; Wasserburg et al. 2017; Battino et al. 2022). Peng et al. (2013) pointed out that the mass and metallicity of a star will affect the composition of its ejected material. This will influence its surrounding interstellar medium and the isotope ratios of its gas. In fact, IRC+10216 is a much younger star (IRC+10216 was born $\sim$1–5 $\times 10^8$ yr ago, assuming masses of 3–5 $M_\odot$) than the Sun (see Peng et al. 2013 and Portinari et al. 1998). Although the carbon-rich AGB star IRC+10216 is located in the solar neighborhood, extensive observational results show that its isotopic composition is remarkably nonsolar (Kahane et al. 1988, 1992; Cernicharo et al. 2000). This is likely due to the fact that the shell of IRC+10216 is highly enriched in processed material after the ultimate dredge-ups (Cernicharo et al. 2000).

Here, we also observed some rotational transitions of rare isotopes. We calculated the observed isotopic ratios of these molecules using the integrated intensities ratio of spectral lines and considering the correction factor ν^{-2} (Kahane et al. 1988; Cernicharo et al. 2000) since column density is proportional to ν^{-2}, where ν represents the rest frequency (Linke et al. 1977). Our results and some results from the literature are listed in Table 6. We have provided only a few key references, which

Table 6
Isotopic Ratios Obtained in IRC+10216, as Described in Section 4.4

Isotope Ratio	Method	Value	Local ISM[a]	Solar[b]
$[^{28}Si]/[^{29}Si]$	SiS	17.3 ± 5.3		19.7
	SiO	$>10.9 \pm 3.7$		
	SiS and SiC$_2$	$18.7^{+1.3c}_{-1.0}$		
	SiS and SiC$_2$	$>15.4 \pm 1.1^d$		
	SiC$_2$	17.2 ± 1.1^e		
	SiS and SiO	18 ± 2^f		
	SiS	$>15.1 \pm 0.7^g$		
	SiS	17^{+5h}_{-4}		
$[^{32}S]/[^{34}S]$	SiS	$>11.4 \pm 3.5$	24 ± 4	22.1
	CS	$>10.6 \pm 1.3$		
	SiS	$20.2^{+2.6c}_{-2.1}$		
	CS and SiS	21.8 ± 2.6^d		
	$^{29}Si^{32}S/^{28}Si^{34}S$, $^{30}Si^{32}S/^{28}Si^{34}S$	18.9 ± 1.3^e		
	SiS	22 ± 2.5^f		
	SiS	19.6 ± 1.3^g		
	SiS	$>14^{+6h}_{-4}$		
	CS	22 ± 4^i		
$[^{12}C]/[^{13}C]$	$^{12}C^{34}S/^{13}C^{32}S^j$	46.4 ± 0.1	54 ± 10	89.4
	HC$_3$N	$>24.1 \pm 6.9$		
	CO	$>9.6 \pm 0.3$		
	HCN	$>2.7 \pm 0.2$		
	CS	$>23.1 \pm 6.3$		
	$^{12}C^{34}S/^{13}C^{32}S$	47^{+6c}_{-5}		
	CS	45 ± 3^d		
	SiC$_2$	34.7 ± 4.3^e		
	CS	35 ± 3.5^f		
	CS	40^{+18g}_{-10}		

Notes.
[a] The local ISM values refer to 7.5 kpc $\leqslant R_{GC} \leqslant$ 8.5 kpc, and the data come from Yan et al. (2023).
[b] Asplund et al. (2009).
[c] Kahane et al. (1988).
[d] Cernicharo et al. (2000).
[e] He et al. (2008).
[f] Agúndez et al. (2012).
[g] Patel et al. (2009).
[h] Fonfría et al. (2015).
[i] Wannier & Linke (1978).
[j] Assuming that the $^{34}S/^{32}S$ ratio is solar.

include research results from the millimeter, submillimeter, and mid-infrared wavelength ranges. For optically thin molecules, the results obtained by this method are close to the isotopic ratios. Optically thick molecules may lead to a lower limit. In this work, the $[^{28}Si]/[^{29}Si]$ ratio is derived to be 17.3 ± 5.3 from the $^{28}SiS/^{29}SiS$ ($J = 5–4$) transitions, but is only 10.9 ± 3.7 from $^{28}SiO/^{29}SiO$ ($J = 2–1$). Thus, the ratio from the SiS ($J = 5–4$) transitions is close to the solar system value, 19.7 (Asplund et al. 2009), while the ratio from SiO ($J = 2–1$) is considerably smaller. In the following, we therefore emphasize ratios (see Table 6), where the lines used to determine isotope ratios are both (almost) optically thin. For the $[^{32}S]/[^{34}S]$ ratio with a solar system ratio of 22.1 (Asplund et al. 2009), this holds when analyzing the sulfur isotopic ratios, which are yielded by calculating optically thin spectral lines and are thus also close to the ratios obtained in the local ISM (Cernicharo et al. 2000; He et al. 2008; Patel et al. 2009; Agúndez et al. 2012). Fonfría et al. (2015) used the Texas Echelon-cross-Echelle Spectrograph at the NASA Infrared

Telescope Facility to obtain high-resolution mid-infrared spectra of SiS in the innermost envelope of IRC+10216. They find that the $[^{28}Si]/[^{29}Si]$ and $[^{32}S]/[^{34}S]$ ratios in the vicinity of the star are compatible with the previously measured values for the outer shells of the envelope.

We have also derived $[^{12}C]/[^{13}C]$ ratios from four carbon-bearing molecules: HC$_3$N, CO, HCN, and CS, and obtained lower limits in that these species are optically thick. The $[^{12}C]/[^{13}C]$ ratios deduced from HC$_3$N/H^{13}CCCN ($J = 10–9$), ^{12}CO/^{13}CO ($J = 1–0$), H^{12}CN/H^{13}CN ($J = 1–0$), and ^{12}CS/^{13}CS are 24.1 ± 6.9, 9.6 ± 0.3, 2.7 ± 0.2, and 23.1 ± 6.3, respectively. Unlike the optically thick species, we also observed C^{34}S and ^{13}CS, both of which are optically thin. Therefore, we are able to deduce a reliable isotopic ratio of $[^{12}C^{34}S]/[^{13}C^{32}S] = 2.1 \pm 0.7$, rather than a lower limit. Because the $[^{32}S]/[^{34}S]$ ratio in IRC+10216 is confirmed to be consistent with the solar value, 22.1, Asplund et al. (2009), we estimate a $[^{12}C]/[^{13}C]$ ratio of 46.4 ± 0.1. This value is in good agreement with existing results (Kahane et al. 1988, 1992; Cernicharo et al. 2000; Agúndez et al. 2012). Therefore, we confirm that the $[^{12}C]/[^{13}C]$ ratio in IRC+10216 is much smaller than the solar value (89.4, see Asplund et al. 2009) and local ISM value (54 ± 10, see Yan et al. 2023). This indicates that there is a nonstandard mixing mechanism or cool-bottom processing (Charbonnel 1995; Zhang et al. 2013) in the CSE of IRC+10216. A more detailed discussion on the effect of $[^{12}C]/[^{13}C]$ on AGB nucleosynthesis can be found in Milam et al. (2009). All of the isotopic ratios discussed here are included in Table 6.

In IRC+10216, the sulfur and silicon isotope ratio calculated by the optically thin spectral lines is close to solar, while the carbon isotope ratio is nonsolar (Cernicharo et al. 2000; He et al. 2008). Fonfría et al. (2015) pointed out that in the past 1000 yr, the nucleosynthesis of the most abundant silicon and sulfur isotopes is not expected to change significantly. In this work, we detected in several cases the same transitions and obtained close results to those described by Kahane et al. (1988, 1992) and Park et al. (2008). Note that we ignored the impact of the beam dilution and did not consider the time variation of the intensities of the spectra. These effects might be important in some cases (He et al. 2017, 2019; Pardo et al. 2018), and might lead to discrepancies in the observationally deduced isotopic ratios.

4.5. Line Surveys toward Other Evolved Stars

In addition to the widely studied AGB star IRC+10216, detailed studies of other carbon stars have also been reported. For instance, IRAS 15194-5115 (II Lup), the brightest carbon star in the Southern Hemisphere at 12 μm, and also the third brightest in both hemispheres, with only IRC+10216 and CIT6 being brighter (Epchtein et al. 1987), was also well investigated. Nyman et al. (1993) used the 15 m Swedish-ESO Submillimeter Telescope (SEST) to make a molecular line survey in the 3 and 1. 3 mm bands toward II Lup, and found that the gas composition of this object is very similar to that of IRC+10216. Subsequently, Woods et al. (2003) conducted a detailed study of the molecules in seven carbon stars with high mass-loss rates (IRAS 15082-4808, IRAS 07454-7112, CIT 6, AFGL 3068, IRC+40540, IRC+10216, and II Lup) in the northern and southern skies. They found that the chemical compositions of these carbon stars were similar, too. However, there was a significant difference in the $[^{12}C]/[^{13}C]$ ratio, which is related to nucleosynthesis and reflects the evolutionary

Table 7
Published Radio Line Surveys of Evolved Stars around the λ 3 mm Band

Source Name	Evolutionary Stage	Chemical Type	Covered Frequencies (GHz)	Telescope	References
IK Tau	AGB	O-rich	79–116	IRAM 30 m	Velilla Prieto et al. (2017)
IRC+10216	AGB	C-rich	84.5–115.8	PMO 13.7 m	This work
IRC+10216	AGB	C-rich	72.2–91.1	Onsala 20 m	Johansson et al. (1984, 1985)
II Lup	AGB	C-rich	80.5–115.5[a]	Mopra-22 m	Smith et al. (2015)
RAFGL 4211	AGB	C-rich	80.5–115.5[a]	Mopra-22 m	Smith et al. (2015)
AI Vol	AGB	C-rich	80.5–115.5[a]	Mopra-22 m	Smith et al. (2015)
RAFGL 4211	AGB	C-rich	~85.10–115.75[b]	SEST–15 m	Woods et al. (2003)
RAFGL 4078	AGB	C-rich	~85.10–115.75[b]	SEST–15 m	Woods et al. (2003)
CIT 6	AGB	C-rich	~85.10–115.75[b]	SEST–15 m	Woods et al. (2003)
CIT 6	AGB	C-rich	90–116	ARO 12 m	Yang et al. (2023)
AFGL 3068	AGB	C-rich	~85.10–115.75[b]	SEST–15 m	Woods et al. (2003)
IRC +40540	AGB	C-rich	~85.10–115.75[b]	SEST–15 m	Woods et al. (2003)
II Lup	AGB	C-rich	~85.10–115.75[b]	SEST–15 m	Nyman et al. (1993)
Red Rectangle	Post-AGB	O-rich	84.50–92.25	IRAM 30 m	Gallardo Cava et al. (2022)
HD 52961	Post-AGB	O-rich	84.40–92.15	IRAM 30 m	Gallardo Cava et al. (2022)
AI Canis Minoris	Post-AGB	O-rich	84.40–92.15	IRAM 30 m	Gallardo Cava et al. (2022)
IRAS 20056 +1834	Post-AGB	O-rich	84.40–92.20	IRAM 30 m	Gallardo Cava et al. (2022)
R Scuti	Post-AGB	O-rich	83.40–92.30	IRAM 30 m	Gallardo Cava et al. (2022)
89 Herculis	Post-AGB	C-rich	83.40–92.50	IRAM 30 m	Gallardo Cava et al. (2022)
CRL 2688	Post-AGB	C-rich	75.7–83.5 and 91.4–99.2	IRAM 30 m	Qiu et al. (2022)
CRL 2688	Post-AGB	C-rich	71–111	ARO 12 m	Zhang et al. (2013)
CRL 2688	Post-AGB	C-rich	85–116	TRAO 14 m	Park et al. (2008)
CRL 618	Post-AGB	C-rich	80.25–115.75	IRAM 30 m	Pardo et al. (2007)
AC Herculis	Post-AGB	O-rich	84.40–92.15	IRAM 30 m	Gallardo Cava et al. (2022)
IRAS 19157 -0257	Post-AGB	…	84.40–92.20	IRAM 30 m	Gallardo Cava et al. (2022)
IRAS 18123 +0511	Post-AGB	…	84.40–92.15	IRAM 30 m	Gallardo Cava et al. (2022)
IRAS 19125 +0343	Post-AGB	…	84.40–92.15	IRAM 30 m	Gallardo Cava et al. (2022)
NGC 7027	PN	C-rich	71–111	ARO 12 m	Zhang et al. (2008)
IC 4406	PN	O-rich	80.5–115.5[a]	Mopra-22 m	Smith et al. (2015)
NGC 6537	PN	O-rich	80.5–115.5[a]	Mopra-22 m	Smith et al. (2015)
NML Cyg	RSG[c]	O-rich	68–116	OSO 20 m	Andrews et al. (2022)
IRC +10420	YHG[d]	N-rich	~83.2–117.1	IRAM 30 m	Quintana-Lacaci et al. (2016)

Notes. Note that the published line surveys toward IRC+10216 are summarized in Table 2.
[a] Note that 98.5–107.5 GHz is uncovered in the observation.
[b] The frequency range is directly taken from the reference.
[c] Red supergiant (RSG) star.
[d] Yellow hypergiant (YHG) star.

status of these stars. Moreover, Zhang et al. (2009a, 2009b, 2020) conducted spectral line surveys toward CIT6 and CRL 3068, and found that only the most abundant molecules could be detected and that the gas compositions of these two sources were very similar to IRC+10216, too.

In short, it is found that the gas compositions of the evolved stars are highly determined by their chemical types (namely, their [C]/[O] ratios), and could be simply classified as C-rich, O-rich, and S-type cases. In principle, the gas compositions of all three types of AGB stars will be well simulated by the corresponding chemical models based on the parent species and physical conditions. This conclusion is further confirmed by the results of other line surveys toward other types of evolved stars in the λ 3 mm band, as summarized in Table 7.

5. Conclusions

We present the first unbiased λ 3 mm (between 84.5 and 115.8 GHz) line survey toward the carbon-rich envelope of IRC+10216 using the PMO 13.7 m telescope, and provide a comprehensive analysis of the molecular spectra by making use of the results from previous studies. A total of 75 spectral lines were detected and assigned to 19 different molecules. The

detected molecules are C_2H, l-C_3H, C_4H, CN, C_3N, HC_3N, HC_5N, HCN, HNC, CH_3CN, MgNC, CO, c-C_3H_2, SiC_2, SiO, SiS, CS, C_2S, and C_3S. The $J = 13$–12 transition of $H^{13}CCCN$ is detected in IRC+10216 for the first time. The excitation temperatures and column densities of these molecules are derived by assuming LTE with excitation temperatures ranging from 5.3–73.4 K, and molecular column densities ranging from 3.27×10^{13} to $4.03 \times 10^{17}\,cm^{-2}$. Except for HCN, the observationally deduced excitation temperatures and column densities roughly agree with previous studies. We find that the fractional abundances of the detected species range between 1.14×10^{-8} and 1.04×10^{-3}. We also find that HC_5N, HC_7N and HC_9N, together with higher J transitions of HC_3N, C_3S, CH_3CN, SiS, C_4H ($\nu = 0$), and C_4H ($\nu = 1$), trace the warmer molecular layers in IRC+10216. Moreover, we detected several isotopologues and derived their isotopic ratios. The $[^{28}Si]/[^{29}Si]$ ratio, for example, is found to be 17.3 ± 5.3, which is roughly consistent with earlier determinations and close to the solar system value. Last but not least, we have summarized all of the 106 species detected in IRC+10216 to date with their observed and modeled column densities for the convenience of future studies.

Acknowledgments

Appendix A
Zoomed-in Plots of Observed Spectra

This appendix includes the spectra of the survey of IRC +10216 ranging from 84.5–115.8 GHz, displayed in consecutive 475 MHz frequency segments with a 0.244 MHz frequency resolution, as shown in Figure A1. The observed molecular spectral lines whose S/N is greater than 3 are marked in blue. Molecules marked with a ? indicate that the S/N of the spectral line is between 2 and 3.
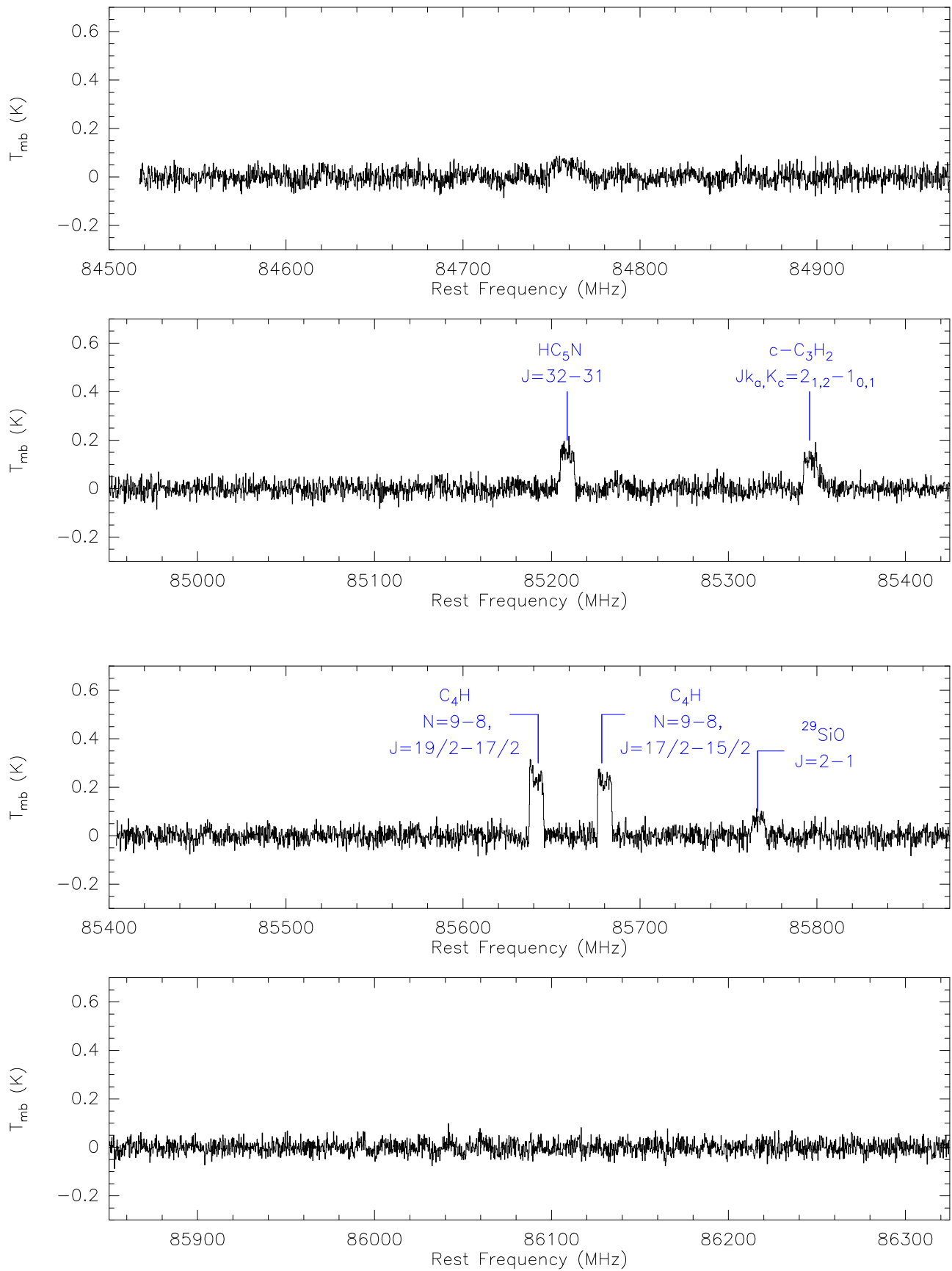
Figure A1. 84.5–115.8 GHz spectrum of IRC+10216 displayed in consecutive 475 MHz frequency segments with 0.244 MHz spectral resolution.
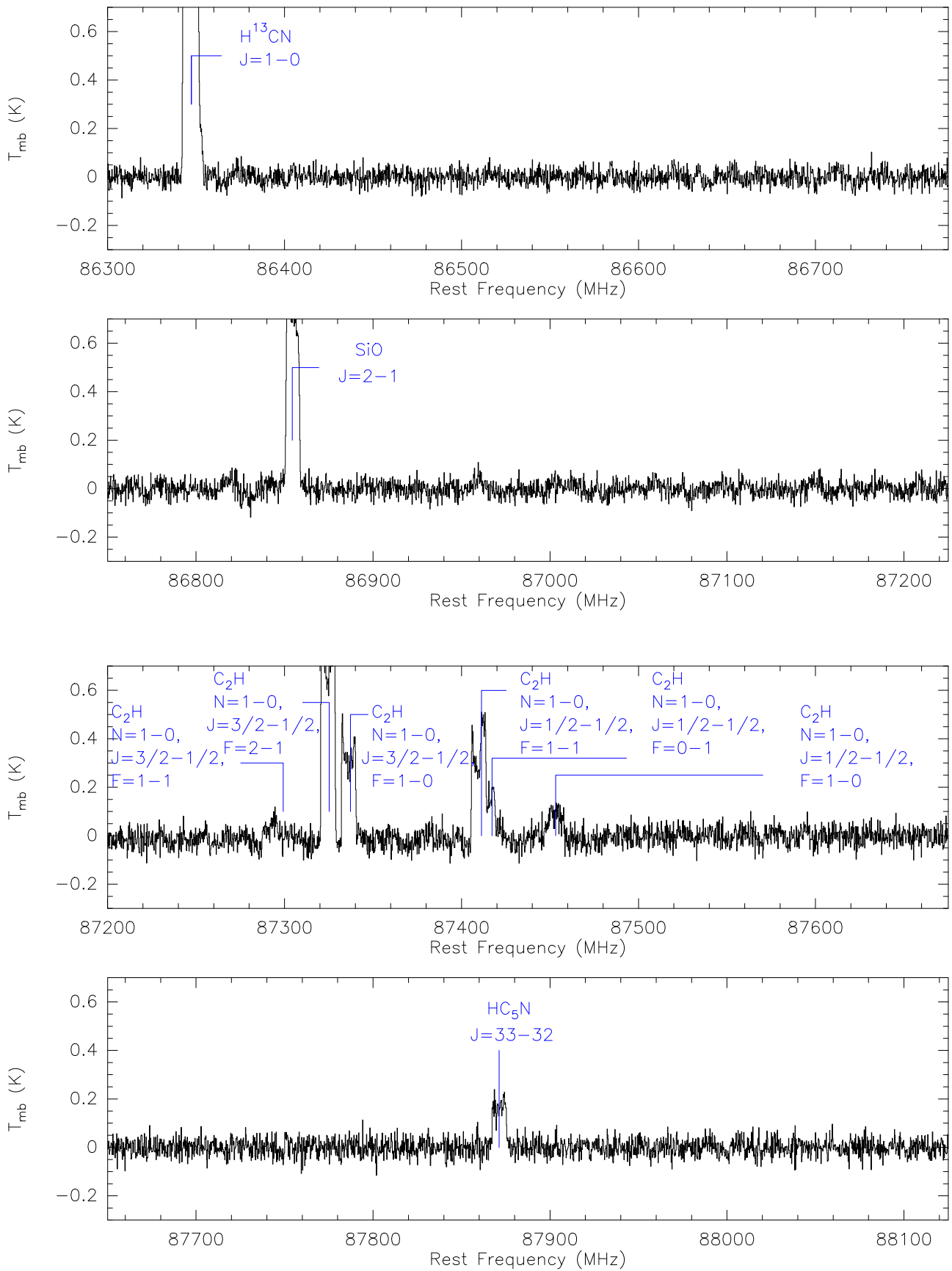
Figure A1. (Continued.)
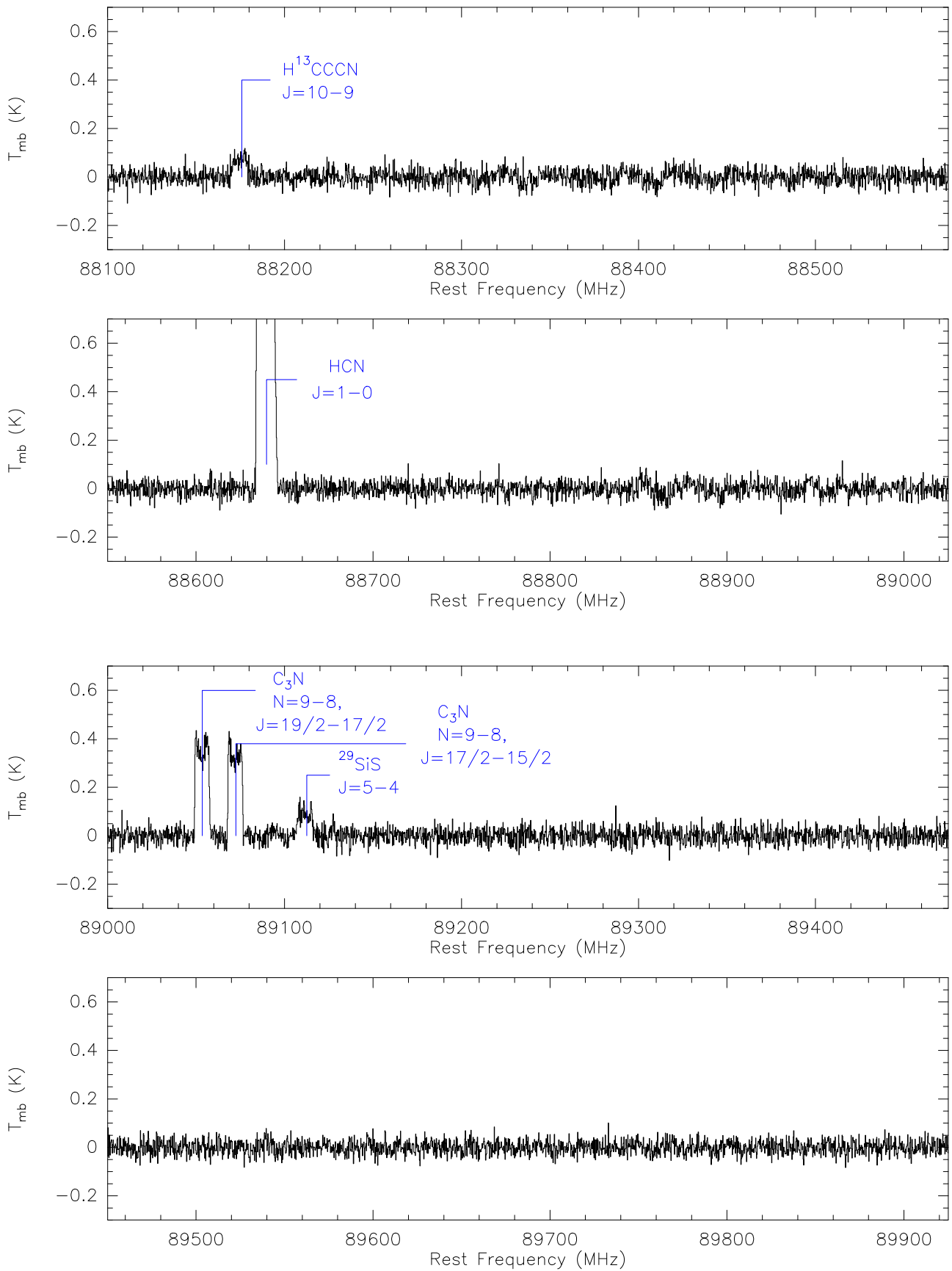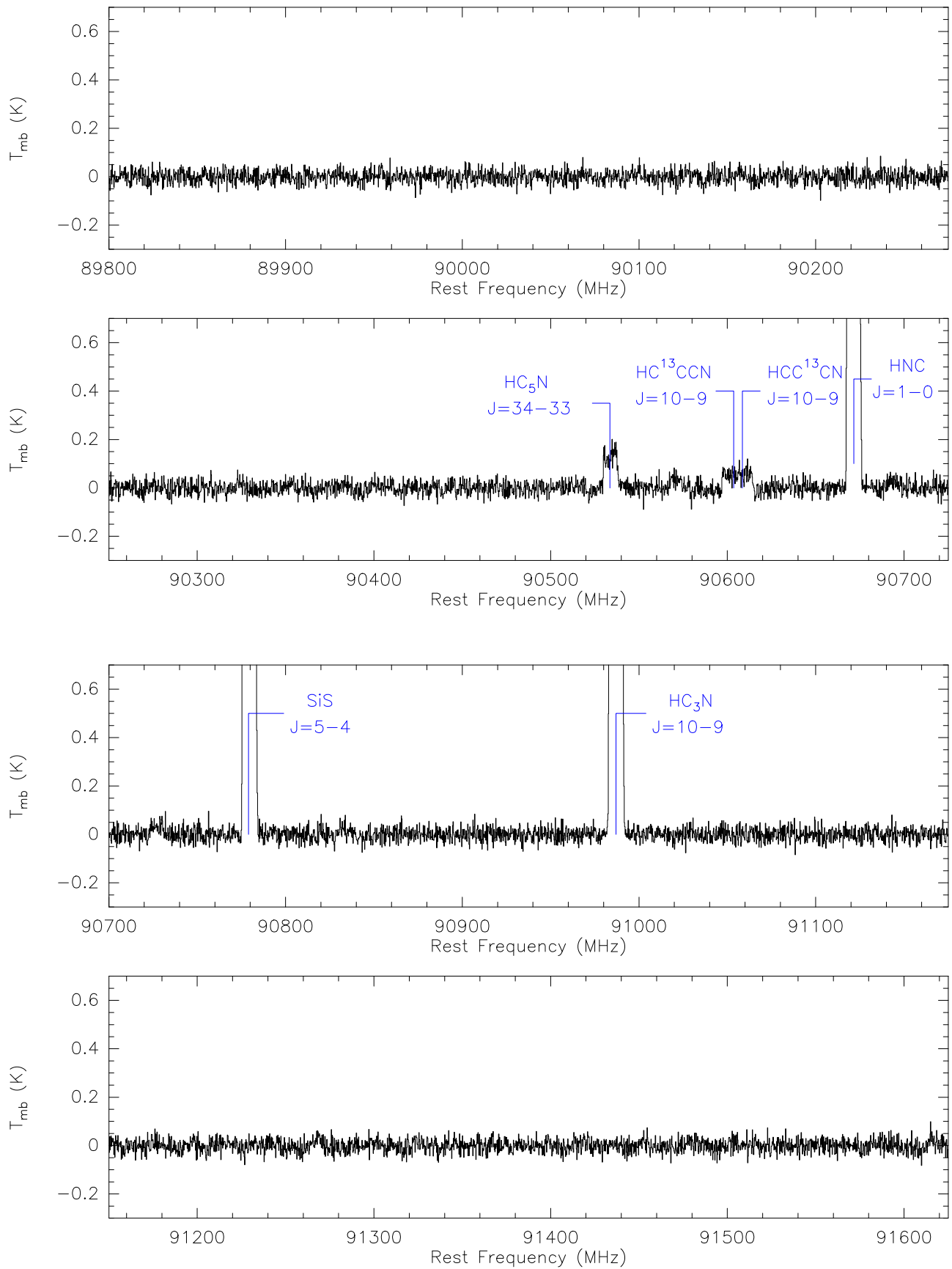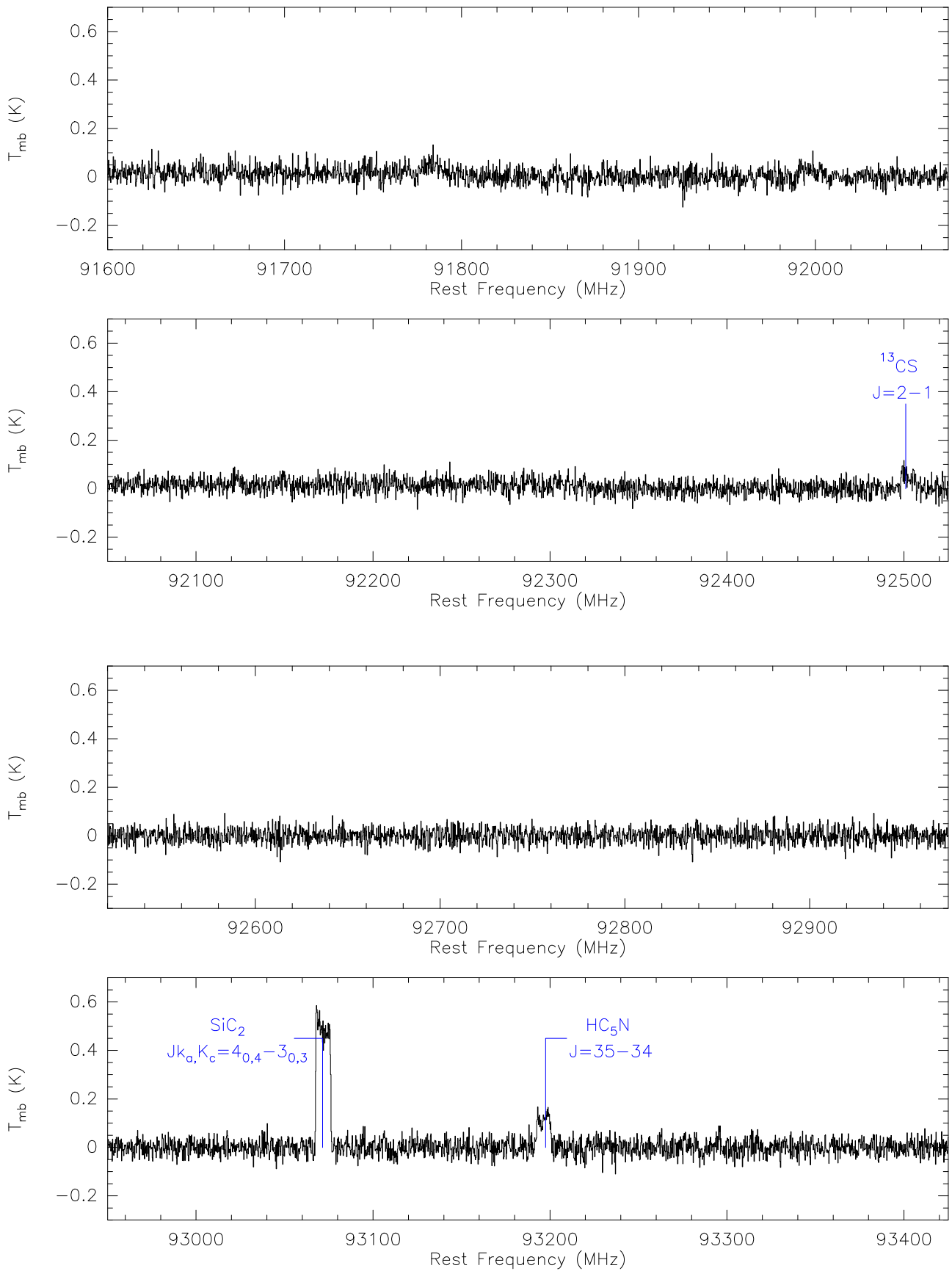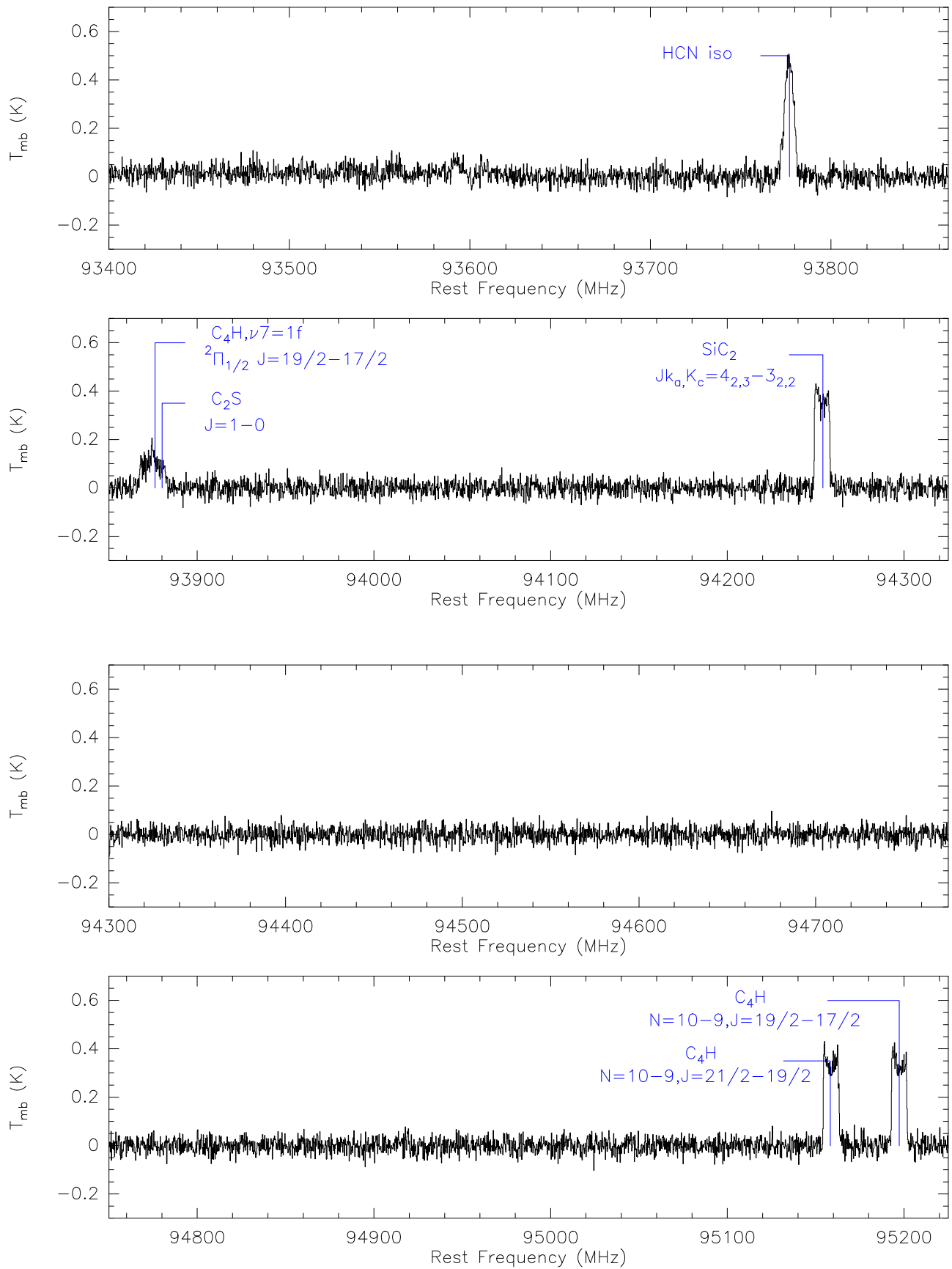
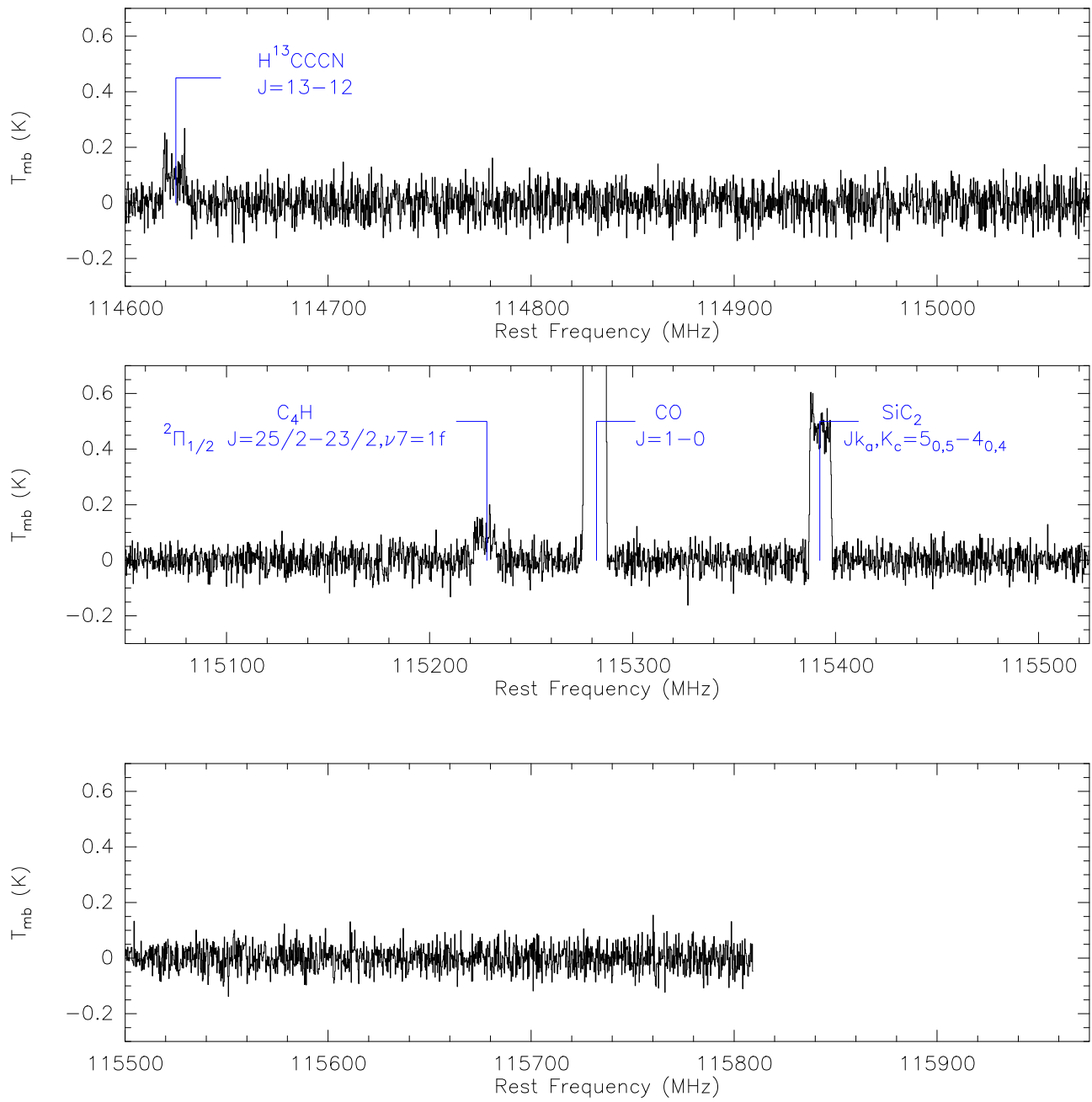**Figure A1.** (Continued.)

Figure A1. (Continued.)

Figure A1. (Continued.)

Figure A1. (Continued.)
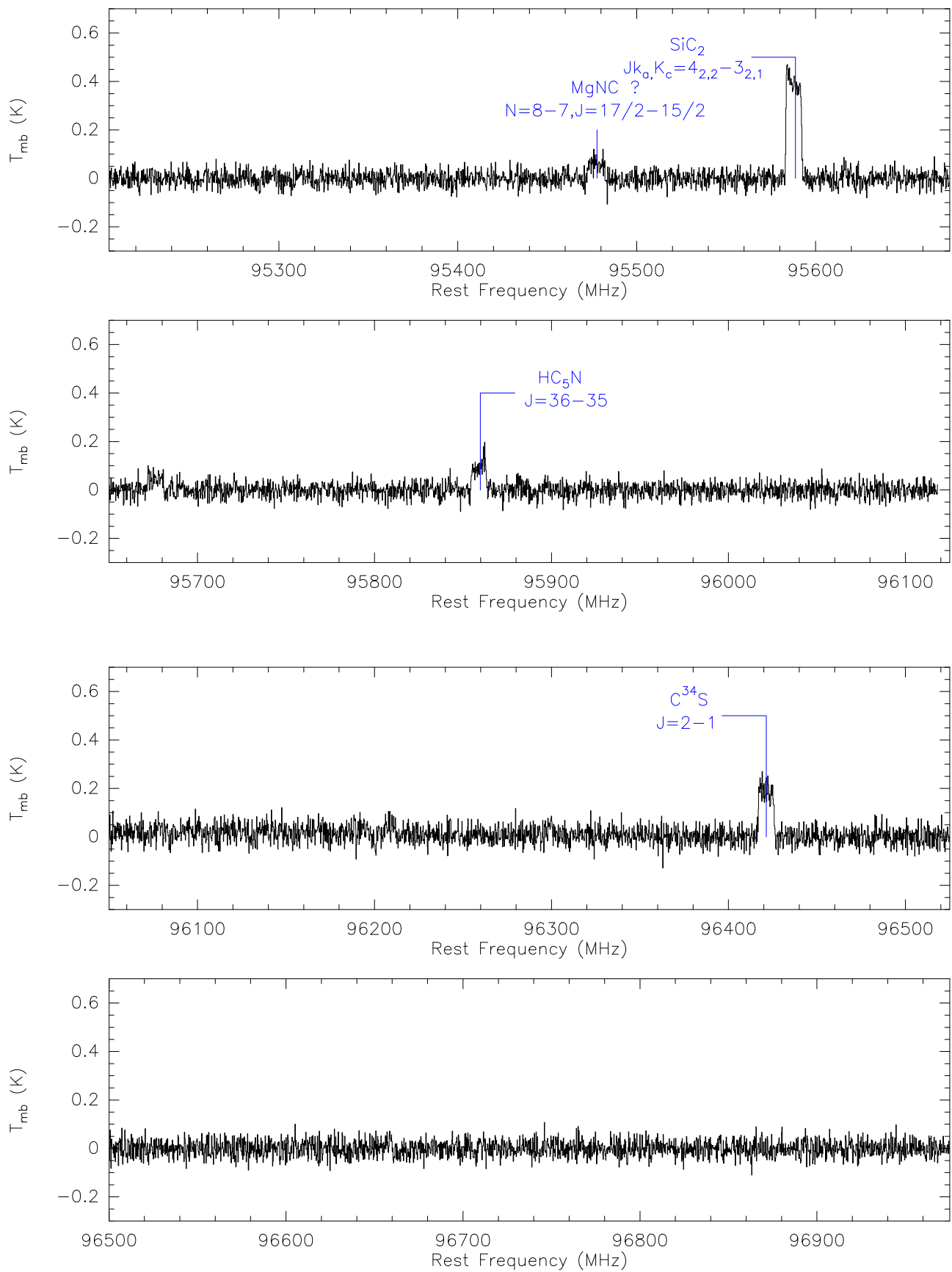
Figure A1. (Continued.)
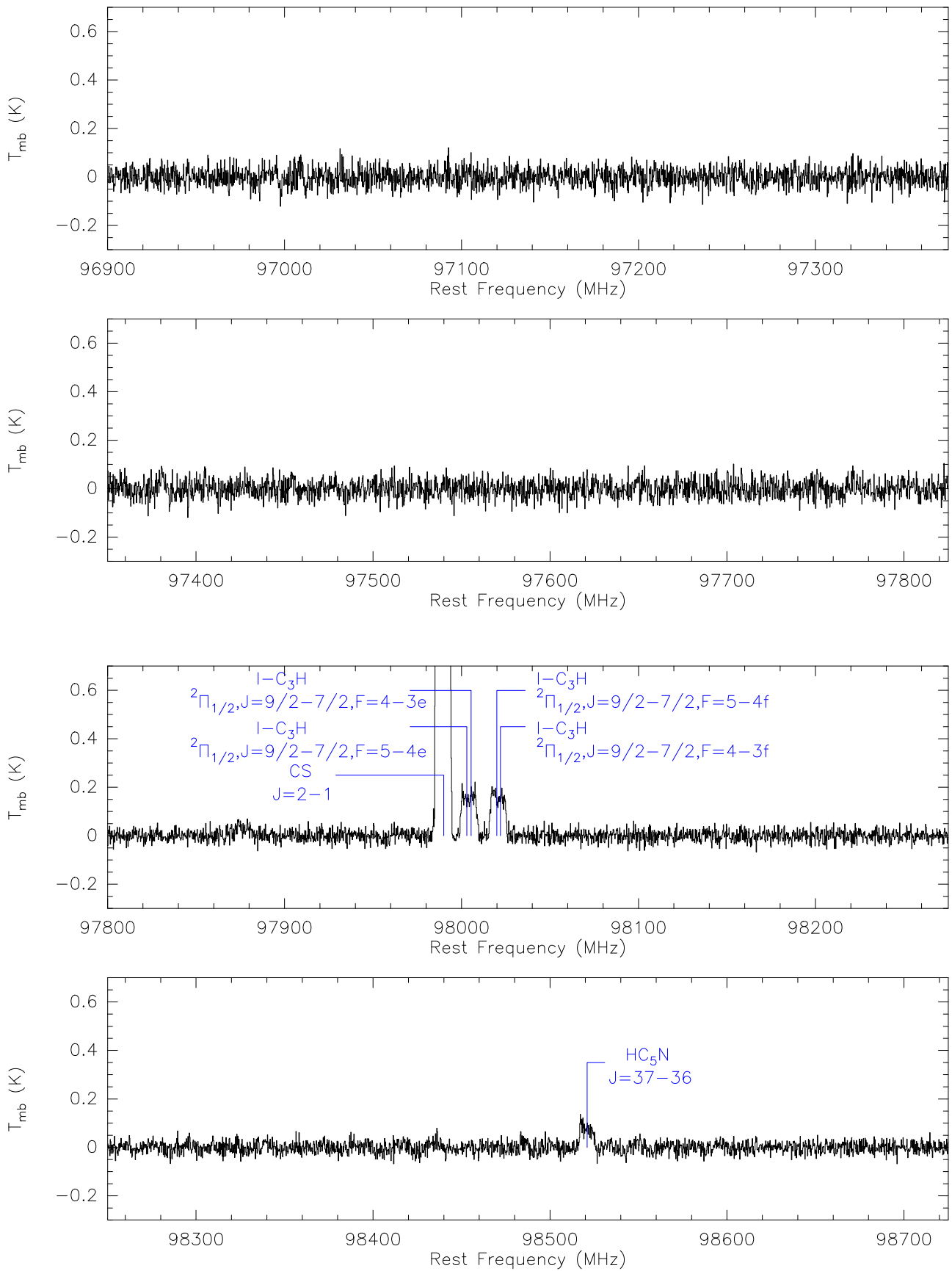
Figure A1. (Continued.)
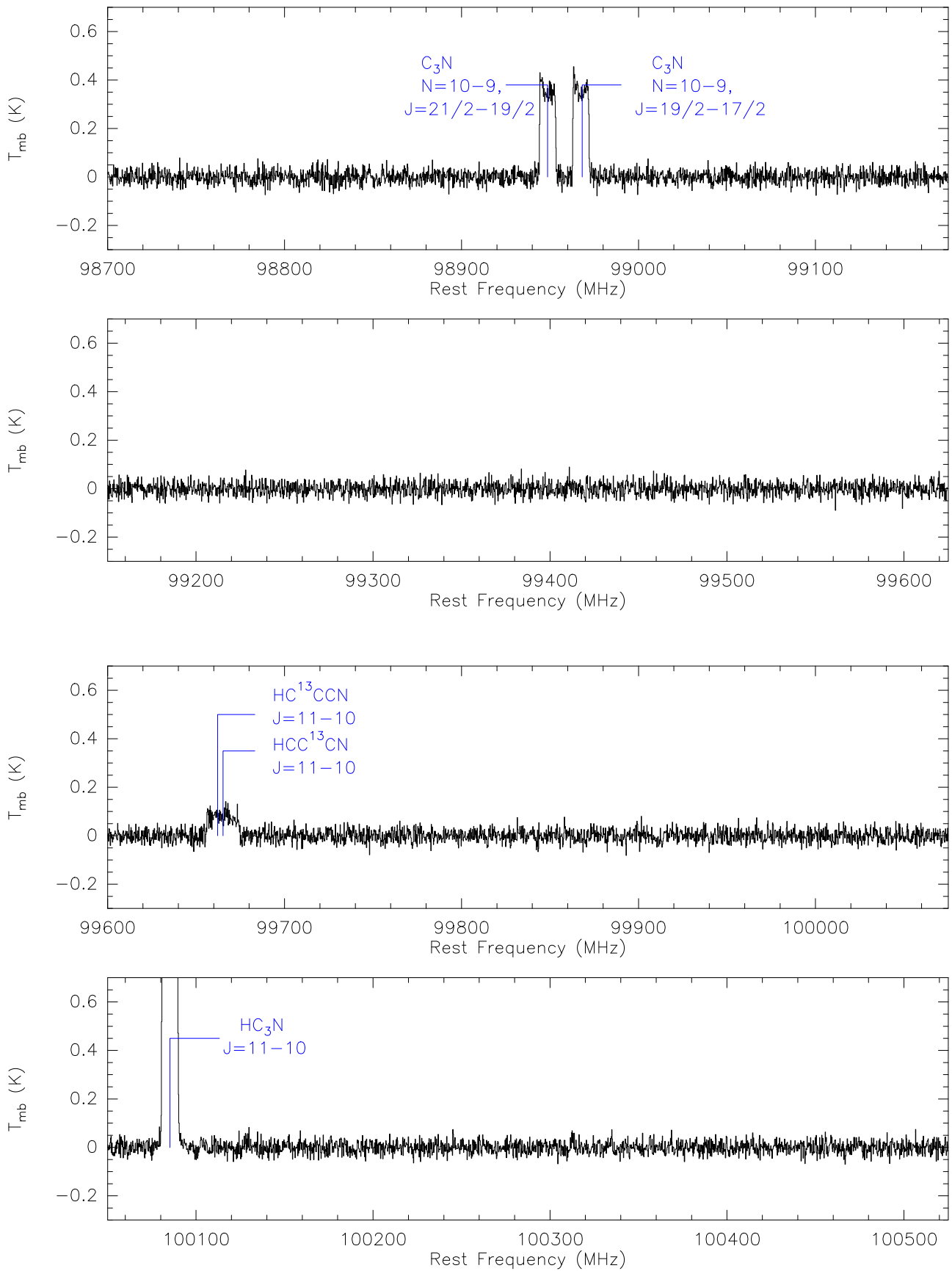
Figure A1. (Continued.)
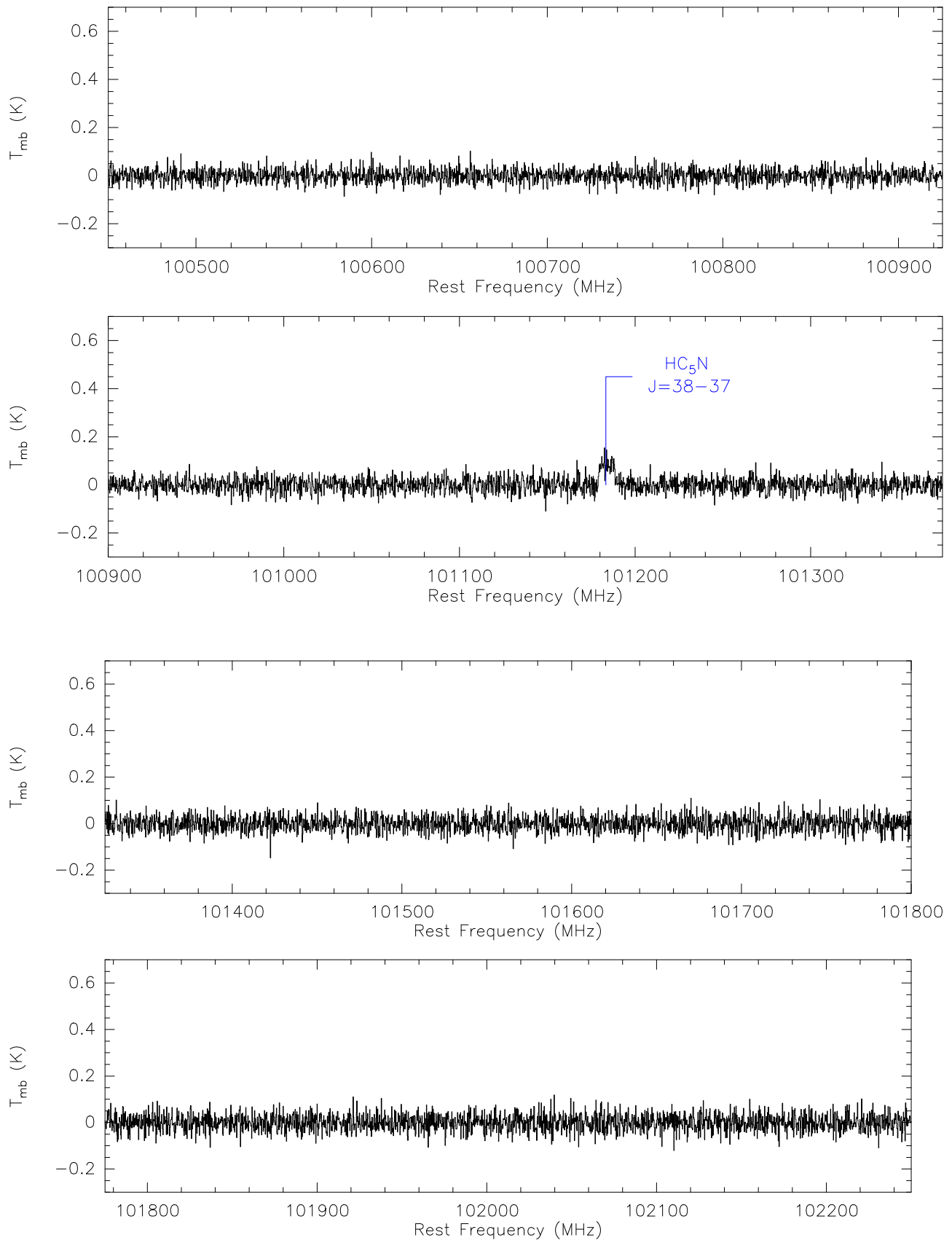
Figure A1. (Continued.)
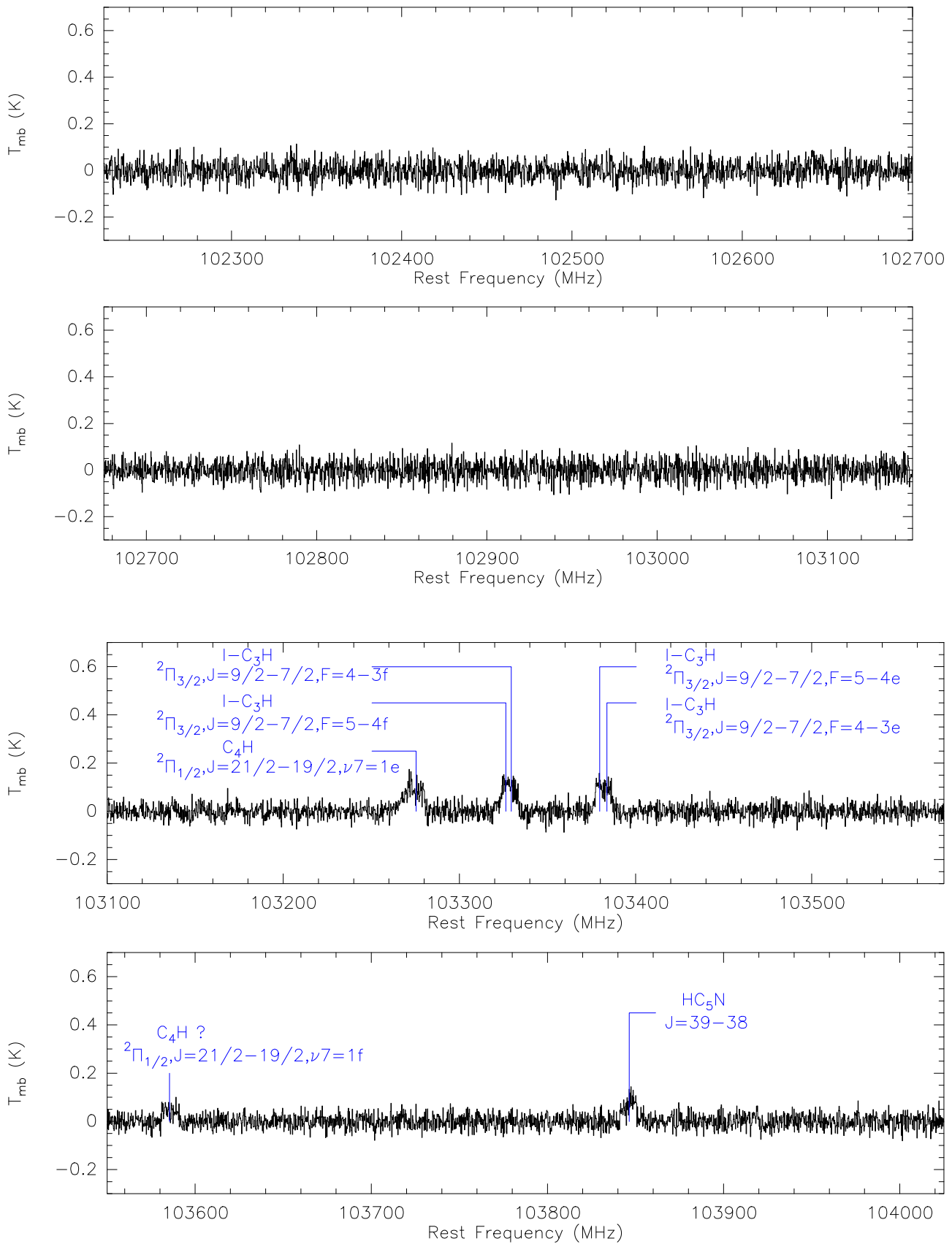
Figure A1. (Continued.)
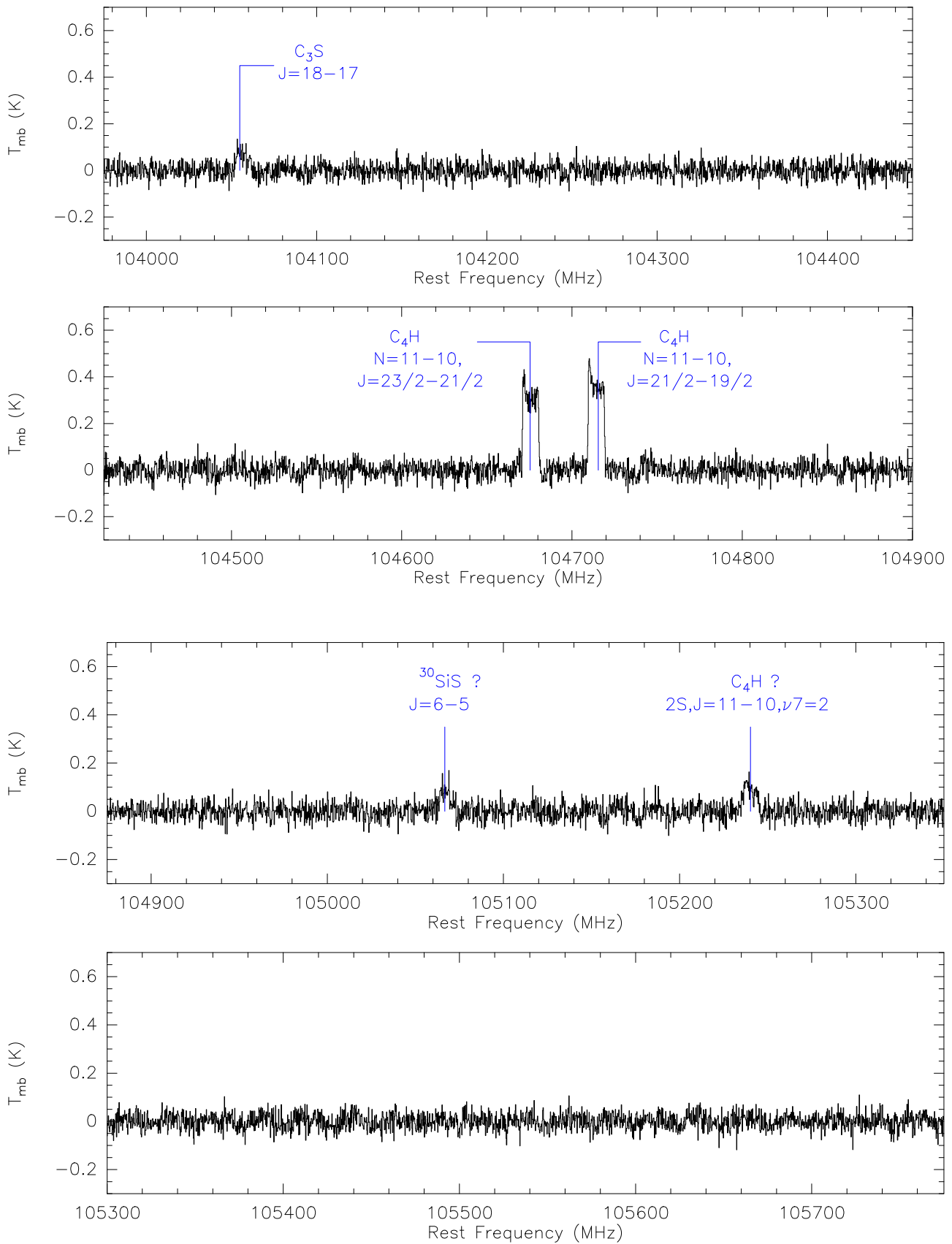
Figure A1. (Continued.)
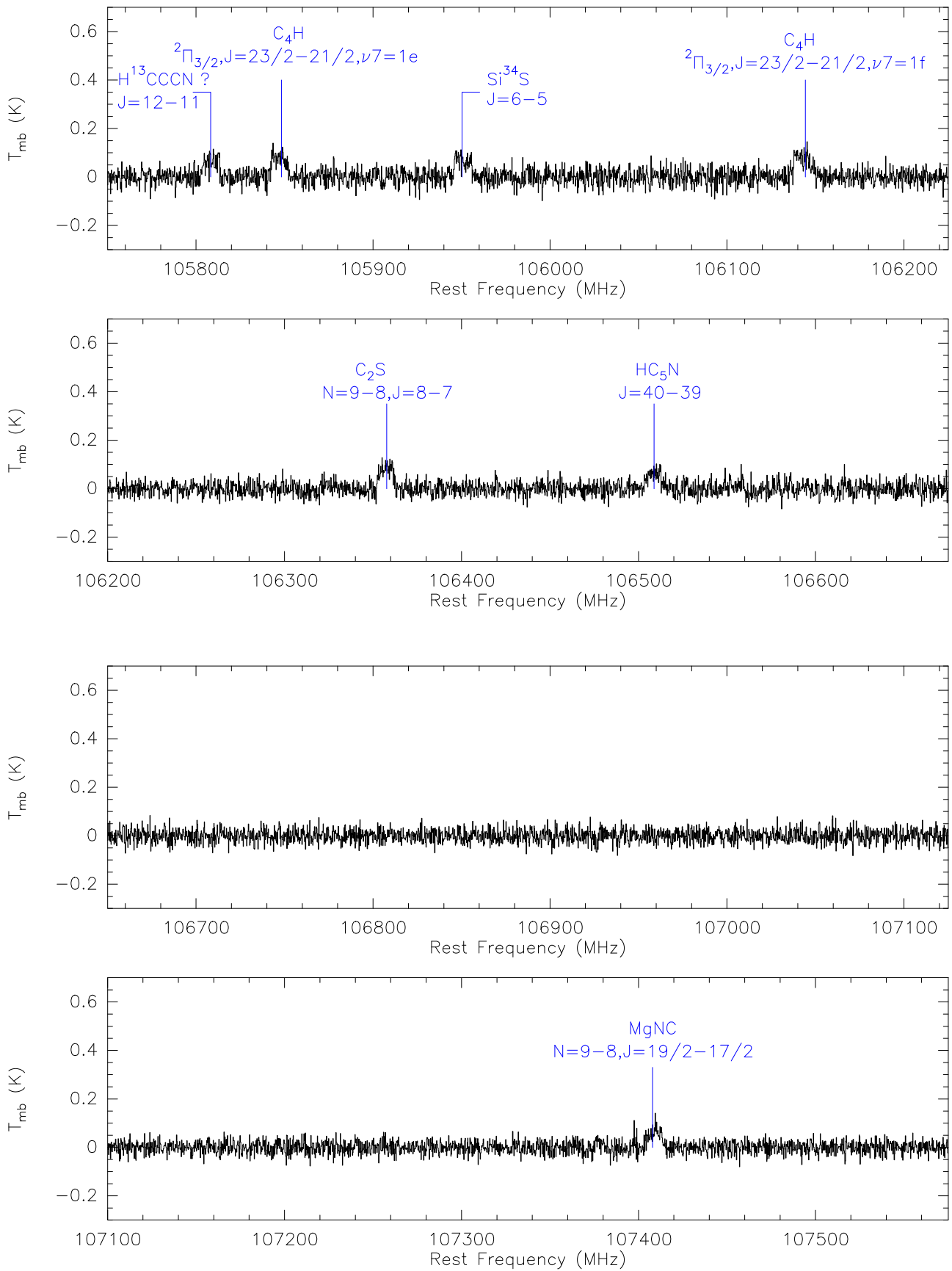
Figure A1. (Continued.)
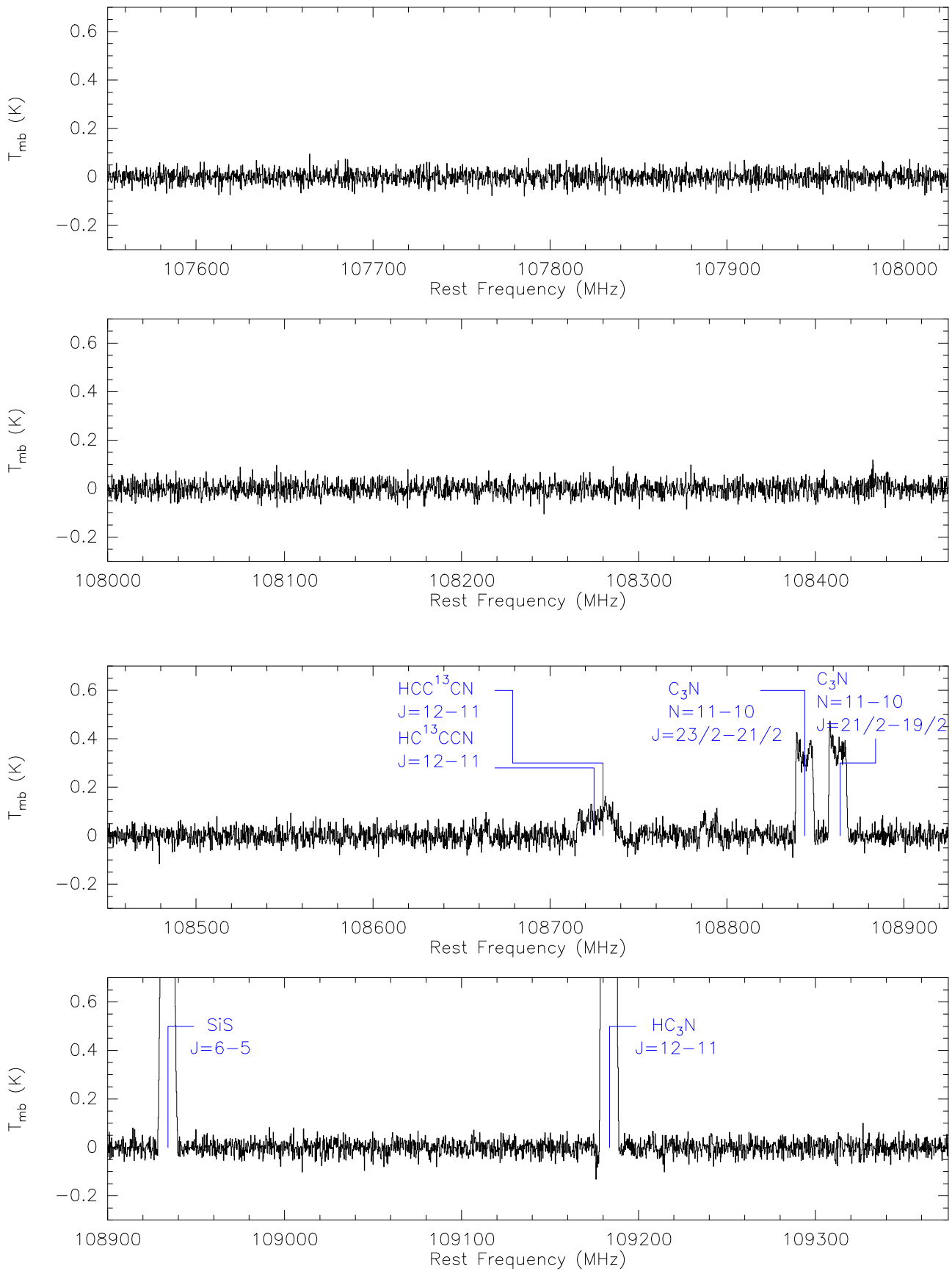
Figure A1. (Continued.)
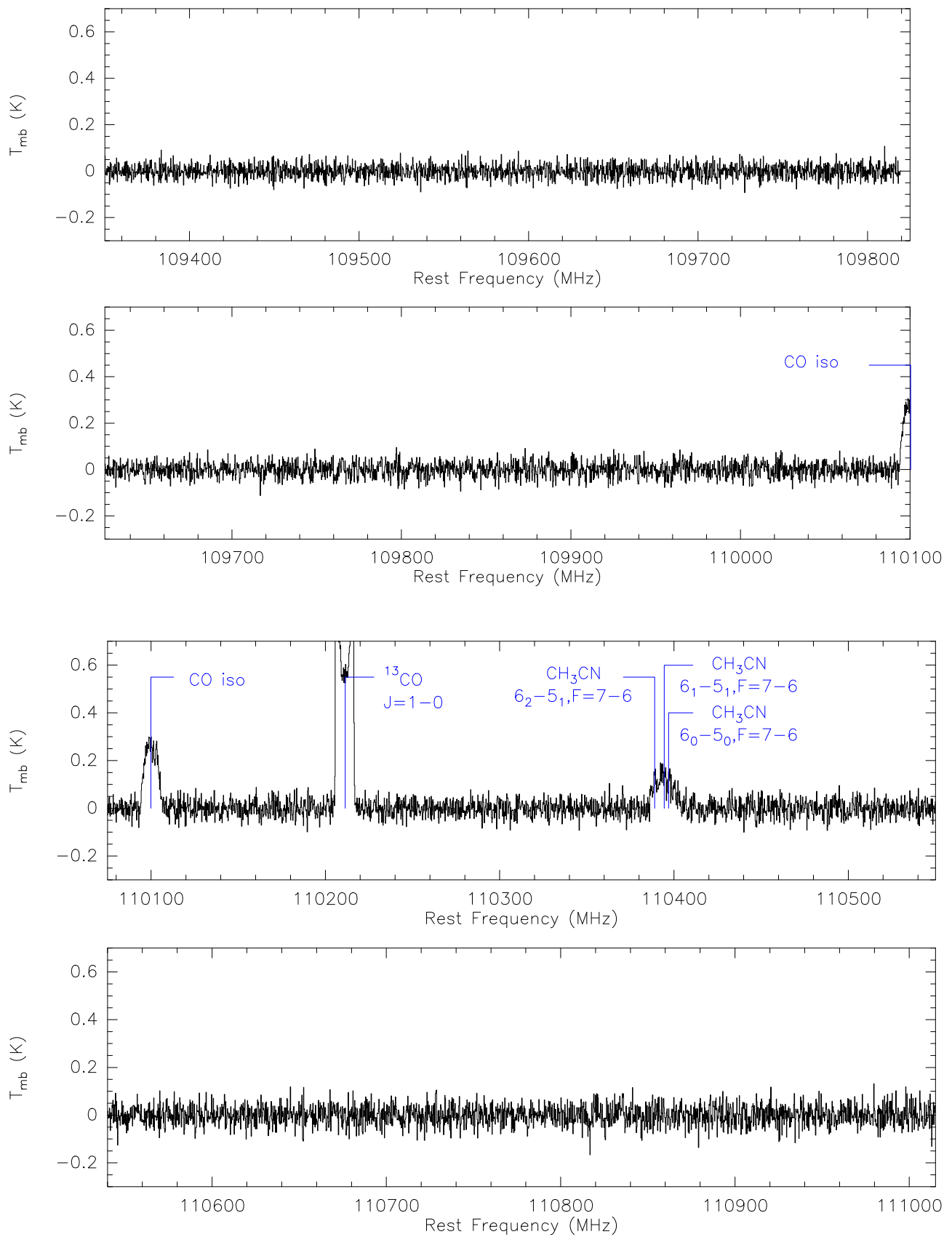
Figure A1. (Continued.)
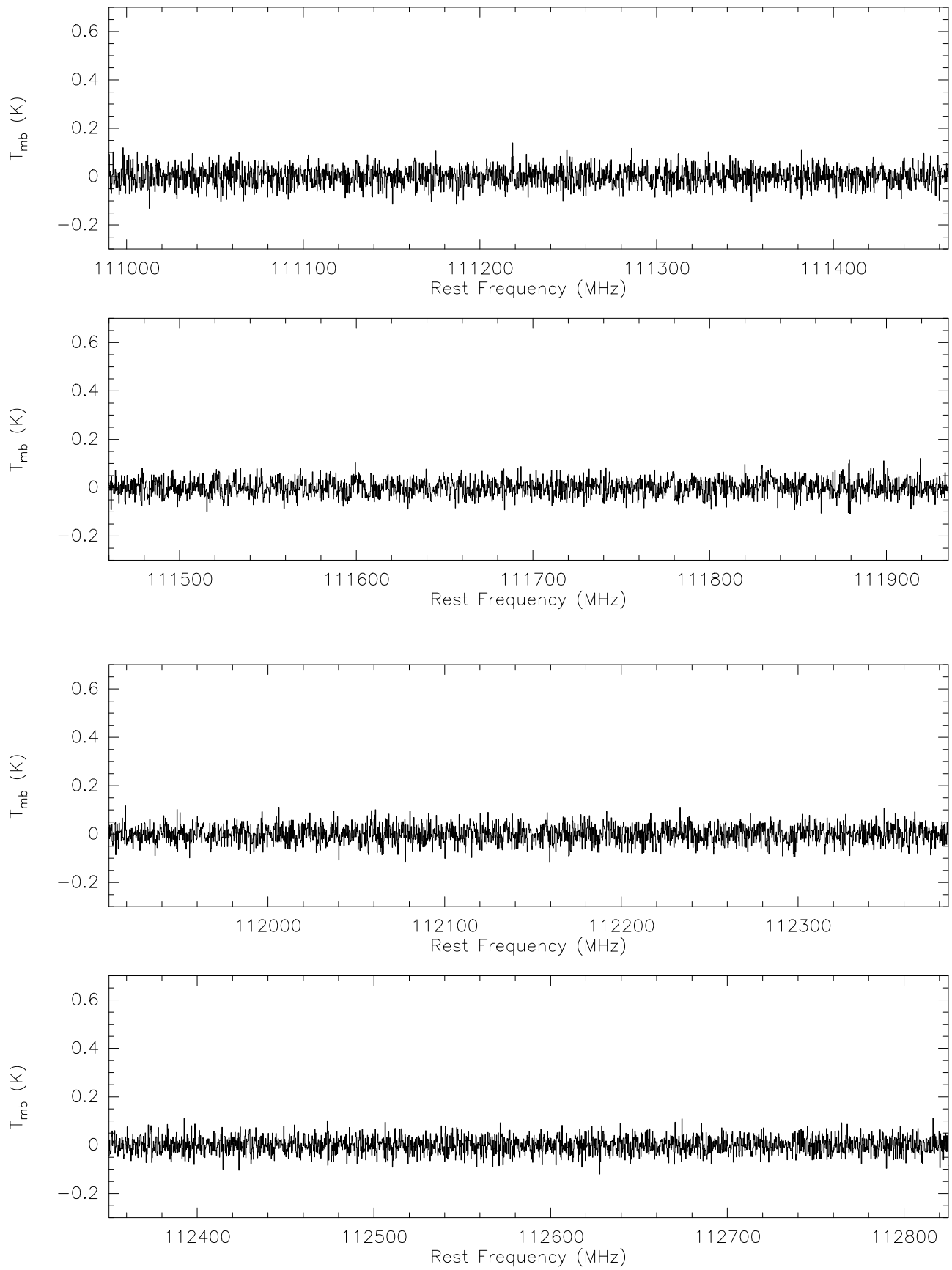
Figure A1. (Continued.)
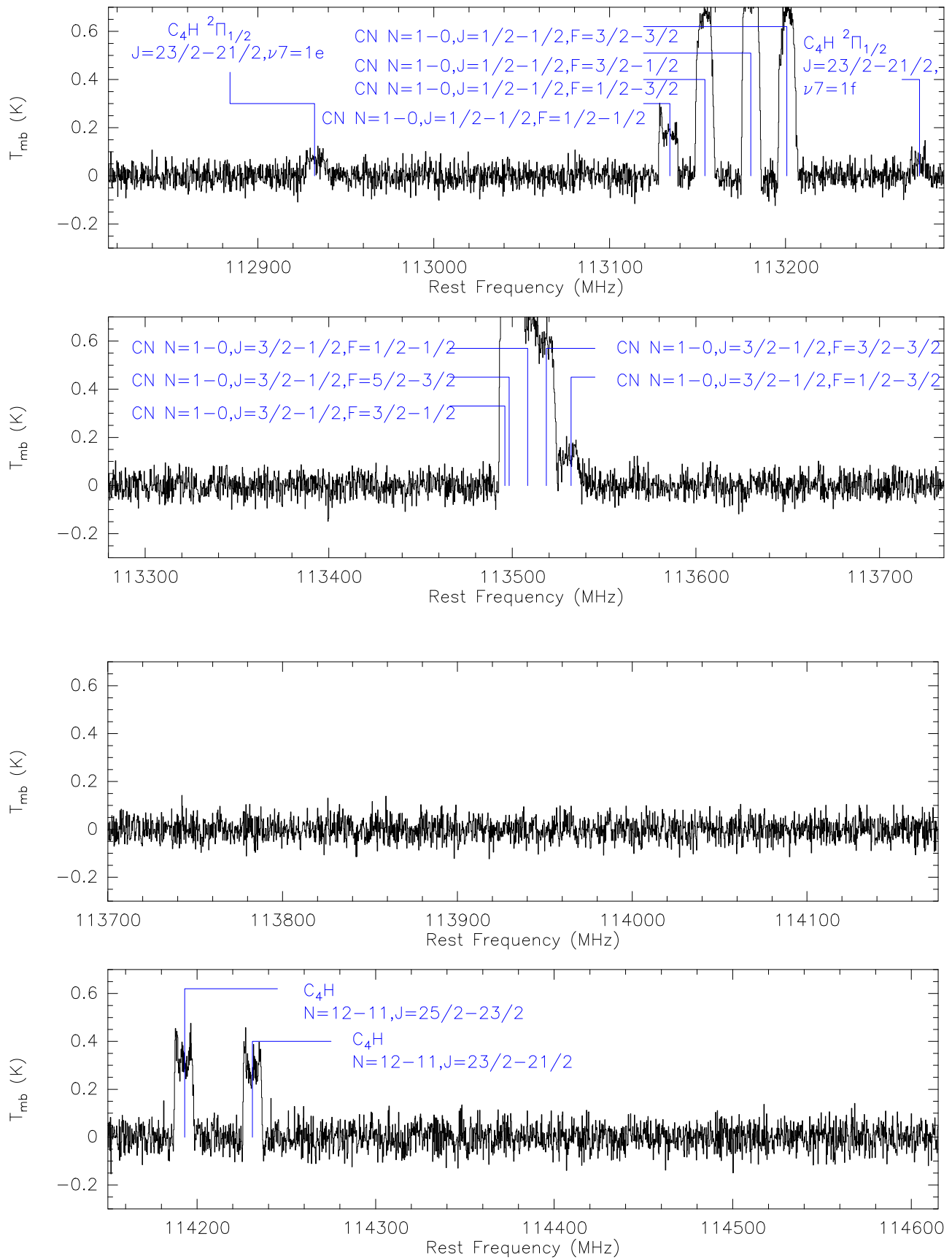
Figure A1. (Continued.)

Figure A1. (Continued.)

Appendix B
Spectral Line Parameters of All the Identified Species

The spectral line parameters of all the identified species from this survey toward IRC+10216 are listed in Table B1.

Table B1
Spectral Line Parameters of all the Identified Species from This Survey toward IRC+10216

No.	Molecule	Transitions	Rest Freq. (MHz)	$\int T_{mb}dv$ (K km s^{-1})	V_{lsr} (km s^{-1})	V_{exp} (km s^{-1})	T_{mb} (K)	Notes
(1)	(2)	(3)	(4)	(5)	(6)	(7)	(8)	
(1)	C$_2$H	$N = 1$–0, $J = 3/2$–1/2, $F = 1$–1	87,284.156	2.15(0.606)	−25.96(0.839)	14.988(0.157)	0.066(0.021)	
(2)	C$_2$H	$N = 1$–0, $J = 3/2$–1/2, $F = 2$–1	87,316.925	22.00(0.904)	−25.75(0.419)	14.035(0.094)	0.693(0.031)	
(3)	C$_2$H	$N = 1$–0, $J = 3/2$–1/2, $F = 1$–0	87,328.624	9.38(1.070)	−25.44(0.419)	13.830(0.028)	0.281(0.037)	
(4)	C$_2$H	$N = 1$–0, $J = 1/2$–1/2, $F = 1$–1	87,402.004	13.40(0.837)	*	*	0.341(0.037)	1
(5)	C$_2$H	$N = 1$–0, $J = 1/2$–1/2, $F = 0$–1	87,407.165	⋯	⋯	⋯	⋯	1
(6)	C$_2$H	$N = 1 - 0$, $J = 1/2$–1/2, $F = 1$–0	87,446.512	1.86(0.599)	−23.94(0.837)	14.461(0.008)	0.070(0.021)	
(7)	l-C$_3$H	$^2\Pi_{1/2}$, $J = 9/2$–7/2, $F = 5$–4e	97,995.212	4.01(0.599)	−26.87(0.747)	14.137(0.094)	0.142(0.021)	1
(8)	l-C$_3$H	$^2\Pi_{1/2}$, $J = 9/2$–7/2, $F = 4$–3e	97,995.951	⋯	⋯	⋯	⋯	
(9)	l-C$_3$H	$^2\Pi_{1/2}$, $J = 9/2$–7/2, $F = 5$–4f	98,011.649	4.60(0.667)	−26.79(0.747)	14.552(0.080)	0.167(0.023)	1
(10)	l-C$_3$H	$^2\Pi_{1/2}$, $J = 9/2$–7/2, $F = 4$–3f	98,012.576	⋯	⋯	⋯	⋯	
(11)	l-C$_3$H	$^2\Pi_{3/2}$, $J = 9/2$–7/2, $F = 5$–4f	103,319.278	2.31(0.667)	−26.67(0.708)	13.754(0.181)	0.079(0.023)	1
(12)	l-C$_3$H	$^2\Pi_{3/2}$, $J = 9/2$–7/2, $F = 4$–3f	103,319.818	⋯	⋯	⋯	⋯	
(13)	l-C$_3$H	$^2\Pi_{3/2}$, $J = 9/2$–7/2, $F = 5$–4e	103,372.506	2.24(0.725)	−24.96(0.708)	13.452(0.145)	0.075(0.025)	1
(14)	l-C$_3$H	$^2\Pi_{3/2}$, $J = 9/2$–7/2, $F = 4$–3e	103,373.129	⋯	⋯	⋯	⋯	
(15)	C$_4$H	$N = 9 - 8$, $J = 19/2$–17/2	85,634.000	6.73(0.552)	−25.73(1.709)	13.692(0.068)	0.282(0.019)	
(16)	C$_4$H	$N = 9$–8, $J = 17/2$–15/2	85,672.570	6.26(0.651)	−26.63(1.709)	14.227(0.102)	0.217(0.022)	
(17)	C$_4$H	$N = 10$–9, $J = 21/2$–19/2	95,150.320	9.69(0.623)	−26.45(1.528)	14.332(0.068)	0.326(0.021)	
(18)	C$_4$H	$N = 10$–9, $J = 19/2$–17/2	95,188.940	8.63(0.605)	−25.94(1.528)	13.840(0.071)	0.289(0.021)	
(19)	C$_4$H	$N = 11$–10, $J = 23/2$–21/2	104,666.560	8.17(0.893)	−26.31(0.699)	13.894(0.046)	0.262(0.031)	
(20)	C$_4$H	$N = 11$–10, $J = 21/2$–19/2	104,705.100	10.3(0.824)	−25.62(0.699)	13.924(0.038)	0.351(0.028)	
(21)	C$_4$H	$N = 12$–11, $J = 25/2$–23/2	114,182.510	8.99(0.984)	−26.11(1.282)	13.666(0.089)	0.291(0.034)	
(22)	C$_4$H	$N = 12 - 11$, $J = 23/2$–21/2	114,221.040	9.75(1.046)	−26.19(1.282)	13.859(0.079)	0.327(0.036)	
(23)	C$_4$H	$^2\Pi_{1/2}$ $J = 19/2$–17/2, $\nu7 = 1f$	93,863.300	3.36(0.551)	×	×	0.080(0.019)	B1
(24)	C$_4$H	$^2\Pi_{1/2}$ $J = 21/2$–19/2, $\nu7 = 1e$	103,266.081	2.66(0.609)	−27.09(1.418)	14.154(0.289)	0.090(0.021)	
(25)	C$_4$H	$^2\Pi_{1/2}$ $J = 23/2$–21/2, $\nu7 = 1e$	112,922.500	1.59(0.580)	−26.95(1.296)	13.801(0.339)	0.061(0.020)	
(26)	C$_4$H	$^2\Pi_{1/2}$ $J = 23/2$–21/2, $\nu7 = 1f$	113,265.900	2.48(0.667)	−26.49(1.292)	13.919(0.233)	0.084(0.023)	
(27)	C$_4$H	$^2\Pi_{3/2}$ $J = 23/2$–21/2, $\nu7 = 1e$	105,838.000	1.96(0.475)	−25.52(1.383)	13.801(0.193)	0.090(0.016)	
(28)	C$_4$H	$^2\Pi_{3/2}$ $J = 23/2$–21/2, $\nu7 = 1f$	106,132.800	1.48(0.551)	−26.54(1.379)	13.048(0.286)	0.057(0.019)	
(29)	C$_4$H	$^2\Pi_{3/2}$ $J = 25/2$–23/2, $\nu7 = 1f$	115,216.800	2.09(0.638)	−25.68(1.271)	14.674(0.331)	0.068(0.022)	
(30)	CN	$N = 1$–0, $J = 3/2$–1/2, $F = 3/2$–1/2	113,488.140	86.4(0.841)	⋯	⋯	1.916(0.029)	1
(31)	CN	$N = 1$–0, $J = 3/2$–1/2, $F = 5/2$–3/2	113,490.982	⋯	⋯	⋯	⋯	
(32)	CN	$N = 1$–0, $J = 3/$–1/2, $F = 1/2$–1/2	113,499.639	⋯	⋯	⋯	⋯	
(33)	CN	$N = 1$–0, $J = 3/2$–1/2, $F = 3/2$–3/2	113,508.944	⋯	⋯	⋯	⋯	
(34)	CN	$N = 1$–0, $J = 3/2$–1/2, $F = 1/2$–3/2	113,520.414	⋯	⋯	⋯	⋯	
(35)	CN	$N = 1$–0, $J = 1/2$–1/2, $F = 1/2$–1/2	113,123.337	6.24(0.696)	−25.91(0.647)	14.363(0.051)	0.235(0.024)	
(36)	CN	$N = 1$–0, $J = 1/2$–1/2, $F = 1/2$–3/2	113,144.192	20.00(0.957)	−26.01(0.647)	13.350(0.057)	0.789(0.033)	
(37)	CN	$N = 1$–0, $J = 1/2$–1/2, $F = 3/2$–1/2	113,170.528	15.80(0.783)	−25.96(0.647)	13.594(0.061)	0.679(0.027)	
(38)	CN	$N = 1$–0, $J = 1/2$–1/2, $F = 3/2$–3/2	113,191.317	18.60(1.218)	−25.81(0.647)	13.264(0.080)	0.804(0.042)	
(39)	C$_3$N	$N = 9$–8, $J = 19/2$–17/2	89,045.590	9.71(0.879)	−26.28(0.822)	13.807(0.049)	0.320(0.030)	
(40)	C$_3$N	$N = -8$, $J = 17/2-15/2$	89,064.360	9.41(0.963)	−25.80(0.822)	13.891(0.053)	0.315(0.033)	
(41)	C$_3$N	$N = 10$–9, $J = 21/2 - 19/2$	98,940.020	8.84(0.883)	−25.67(0.740)	13.734(0.049)	0.297(0.031)	
(42)	C$_3$N	$N = 10$–9, $J = 19/2 - 17/2$	98,958.780	10.40(0.835)	−25.88(0.740)	13.781(0.043)	0.358(0.029)	
(43)	C$_3$N	$N = 11$–10, $J = 23/2 - 21/2$	108,834.270	5.63(0.546)	−25.81(0.673)	14.027(0.049)	0.193(0.019)	
(44)	C$_3$N	$N = 11$–10, $J = 21/2 - 19/2$	108,853.020	5.51(0.491)	−26.09(0.672)	14.365(0.041)	0.185(0.017)	
(45)	HC$_3$N	$J = 10$–9	90,978.989	56.30(1.018)	−25.88(0.402)	13.854(0.014)	2.448(0.035)	
(46)	HC$_3$N	$J = 11$–10	100,076.386	45.20(0.744)	−25.22(1.463)	13.399(0.047)	1.938(0.026)	
(47)	HC$_3$N	$J = 12$–11	109,173.638	41.10(0.745)	−25.96(1.341)	13.435(0.047)	1.764(0.026)	
(48)	H^{13}CCCN	$J = 10$–9	88,166.808	2.19(0.626)	−27.68(1.660)	14.177(0.311)	0.076(0.022)	
(49)	H^{13}CCCN	$J = 13$–12	114,615.021	3.17(0.918)	−27.34(1.277)	14.173(0.271)	0.094(0.031)	NS
(50)	HC^{13}CCN	$J = 10$–9	90,593.059	×	×	×	×	B2
(51)	HCC^{13}CN	$J = 10$–9	90,601.791	4.56(0.551)	×	×	0.077(0.019)	B2
(52)	HC^{13}CCN	$J = 11$–10	99,651.863	2.55(0.435)	×	×	0.045(0.015)	B3
(53)	HCC^{13}CN	$J = 11$–10	99,661.471	×	×	×	×	B3
(54)	HC^{13}CCN	$J = 12$–11	108,710.523	2.63(0.406)	×	×	0.048(0.014)	B4
(55)	HCC^{13}CN	$J = 12$–11	108,721.008	×	×	×	×	B4
(56)	HC$_5$N	$J = 32$–31	85,201.346	4.43(0.434)	−26.10(1.718)	14.345(0.130)	0.148(0.015)	
(57)	HC$_5$N	$J = 33$–32	87,863.630	4.75(0.645)	−26.30(1.666)	14.042(0.160)	0.166(0.022)	
(58)	HC$_5$N	$J = 34$–33	90,525.890	3.54(0.460)	−26.81(1.617)	13.911(0.156)	0.124(0.016)	
(59)	HC$_5$N	$J = 35$–34	93,188.123	3.22(0.750)	−26.45(1.571)	13.336(0.230)	0.118(0.026)	
(60)	HC$_5$N	$J = 36$–35	95,850.335	3.30(0.641)	−28.05(1.527)	13.111(0.181)	0.112(0.022)	

Table B1
(Continued)

| No.	Molecule	Transitions	Rest Freq. (MHz)	$\int T_{mb}dv$ (K km s^{-1})	V_{lsr} (km s^{-1})	V_{exp} (km s^{-1})	T_{mb} (K)	Notes
(1)	(2)	(3)	(4)	(5)	(6)	(7)	(8)	
(61)	HC$_5$N	$J = 37$–36	98,512.524	1.96(0.414)	−25.21(1.486)	13.377(0.172)	0.074(0.014)	
(62)	HC$_5$N	$J = 38$–37	101,174.677	2.66(0.577)	−27.46(1.447)	13.756(0.232)	0.096(0.020)	
(63)	HC$_5$N	$J = 39$–38	103,836.817	2.25(0.513)	−26.59(1.410)	13.266(0.181)	0.089(0.018)	
(64)	HC$_5$N	$J = 40$–39	106,498.910	2.42(0.530)	−25.02(1.374)	14.428(0.288)	0.067(0.018)	
(65)	c-C$_3$H$_2$	$J_{Ka,Kc} = 2_{1,2} - 1_{0,1}$	85,338.906	2.97(0.509)	−25.77(1.715)	13.869(0.202)	0.099(0.018)	
(66)	HNC	$J = 1$–0, $F = 0$–1	90,663.450	⋯	⋯	⋯	⋯	
(67)	HNC	$J = 1$–0, $F = 2$–1	90,663.574	22.30(0.702)	−25.93(0.807)	13.740(0.019)	0.199(0.024)	1
(68)	HNC	$J = 1$–0, $F = 1$–1	90,663.656	⋯	⋯	⋯	⋯	
(69)	HCN	$J = 1$–0, $F = 1$–1	88,630.416	⋯	⋯	⋯	⋯	
(70)	HCN	$J = 1$–0, $F = 2$–1	88,631.847	174(9.918)	−22.87(0.159)	16.211(0.052)	8.135(0.342)	1
(71)	HCN	$J = 1$–0, $F = 0$–1	88,633.936	⋯	⋯	⋯	⋯	
(72)	H^{13}CN	$J = 1$–0, $F = 1$–1	86,338.737	⋯	⋯	⋯	⋯	
(73)	H^{13}CN	$J = 1$–0, $F = 2$–1	86,340.176	60.70(3.915)	−24.16(0.424)	16.925(0.055)	2.645(0.135)	1
(74)	H^{13}CN	$J = 1$–0, $F = 0$–1	86,342.255	⋯	⋯	⋯	⋯	
(75)	CO	$J = 1$–0	115,271.202	228.00(2.697)	−26.02(0.159)	14.220(0.006)	9.673(0.093)	
(76)	^{13}CO	$J = 1$–0	110,201.354	21.80(0.732)	−26.07(0.664)	14.547(0.009)	0.455(0.025)	
(77)	SiO	$J = 2$–1, $\nu = 0$	86,846.995	18.20(0.921)	−25.81(0.843)	13.518(0.040)	0.722(0.032)	
(78)	^{29}SiO	$J = 2$–1, $\nu = 0$	85,759.188	1.63(0.551)	−27.88(1.707)	13.460(0.047)	0.058(0.019)	
(79)	^{29}SiS	$J = 5$–4, $\nu = 0$	89,103.720	1.70(0.551)	−25.84(1.643)	14.044(0.266)	0.065(0.019)	
(80)	Si^{34}S	$J = 6$–5, $\nu = 0$	105,941.503	1.97(0.609)	−24.42(1.382)	14.679(0.231)	0.070(0.021)	
(81)	SiS	$J = 5$–4, $\nu = 0$	90,771.561	30.40(0.725)	−25.93(0.843)	13.742(0.018)	1.102(0.025)	
(82)	SiS	$J = 6$–5, $\nu = 0$	108,924.297	23.80(0.551)	−26.22(1.344)	13.466(0.043)	1.009(0.019)	
(83)	SiC$_2$	$J_{Ka,Kc} = 4_{0,4} - 3_{0,3}$	93,063.639	14.30(0.986)	−26.95(0.787)	13.845(0.037)	0.501(0.034)	
(84)	SiC$_2$	$J_{Ka,Kc} = 4_{2,3} - 3_{2,2}$	94,245.393	9.44(0.838)	−25.40(1.553)	13.987(0.069)	0.332(0.029)	
(85)	SiC$_2$	$J_{Ka,Kc} = 4_{2,2} - 3_{2,1}$	95,579.381	10.30(0.559)	−25.98(0.153)	13.815(0.059)	0.335(0.019)	
(86)	SiC$_2$	$J_{Ka,Kc} = 5_{0,5} - 4_{0,4}$	115,382.375	13.40(0.870)	−25.92(1.269)	13.855(0.029)	0.468(0.030)	
(87)	CS	$J = 2$–1	97,980.953	61.20(4.421)	−25.85(0.187)	13.275(0.015)	2.522(0.049)	
(88)	^{13}CS	$J = 2$–1	92,494.270	2.36(0.696)	−23.24(1.583)	13.908(0.310)	0.079(0.024)	
(89)	C^{34}S	$J = 2$–1	96,412.950	5.46(0.638)	−25.59(1.518)	14.292(0.134)	0.197(0.022)	
(90)	C$_2$S	$N = 8$–7, $J = 7$–6	93,870.098	×	×	×	×	B1
(91)	C$_2$S	$N = 9$–8, $J = 8$–7	106,347.740	1.94(0.405)	−27.16(1.376)	13.352(0.253)	0.070(0.014)	
(92)	C$_3$S	$J = 1$–17	104,048.451	1.71(0.535)	−23.46(1.759)	13.553(0.394)	0.057(0.018)	
(93)	MgNC	$N = 9$–8, $J = 19/2$–17/2	107,399.420	1.67(0.609)	−25.97(0.682)	14.001(0.230)	0.064(0.021)	
(94)	CH$_3$CN	$J_K = 6$–5$_2$, $F = 7$–6	110,375.049	2.01(0.783)	⋯	⋯	0.081(0.026)	1
(95)	CH$_3$CN	$J_K = 6_1 - 5_1$, $F = 7$–6	110,381.400	⋯	⋯	⋯	⋯	
(96)	CH$_3$CN	$J_K = 6_0$–5$_0$, $F = 7$–6	110,383.518	⋯	⋯	⋯	⋯	

Notes. The numbers in parentheses represent the 1σ error. The rms noise on a main-beam brightness temperature scale is obtained by statistics in areas without clear spectral lines, and the measurement uncertainty of the integrated intensities is the product of the rms noise and the width of the line of about 29 km s^{-1}. The error in the expansion velocity is obtained by shell function fitting, and the error in the LSR velocity is the velocity width of a channel. The information for each column in the table is as follows: column (1): number; column (2): molecule name; column (3): quantum numbers; column (4): rest frequency (rest frequency is adopted from JPL (Pickett et al. 1998), CDMS (Müller et al. 2005), and the Splatalogue databases as well as the online Lovas line list (Lovas 2004) for astronomical spectroscopy); column (5): integrated intensity (in main beam brightness temperature); column (6): LSR velocity; column (7): expansion velocity; column (8): main beam brightness temperature. ⋯ means the values cannot be obtained because of unresolved hfs, × implies that the values cannot be obtained due to two blended spin-rotation components, and * addresses values that cannot be derived from our detection. (1) The hfs is not resolved. (B1) $^2\Pi_{1/2}$ C$_4$H $J = 19/2$–17/2, $\nu 7 = 1f$ blended with C$_2$S $N = 8$–7, $J = 7$–6. (B2) HC^{13}CCN $J = 10$–9 is blended with HCC^{13}CN $J = 10$–9. (B3) HC^{13}CCN $J = 11$–10 is blended with HCC^{13}CN $J = 11$–10. (B4) HC^{13}CCN $J = 12$–11 is blended with HCC^{13}CN $J = 12$–11. (NS) Transitions that are detected for the first time toward the source are marked with "NS."

Appendix C
Spectral Line Profiles of the Detected Species

In this appendix, we give all the observed spectral profiles of the identified species in Figures C1–C10. Note that we have fitted each spectrum by one of the four line profiles shown in Figure 2.
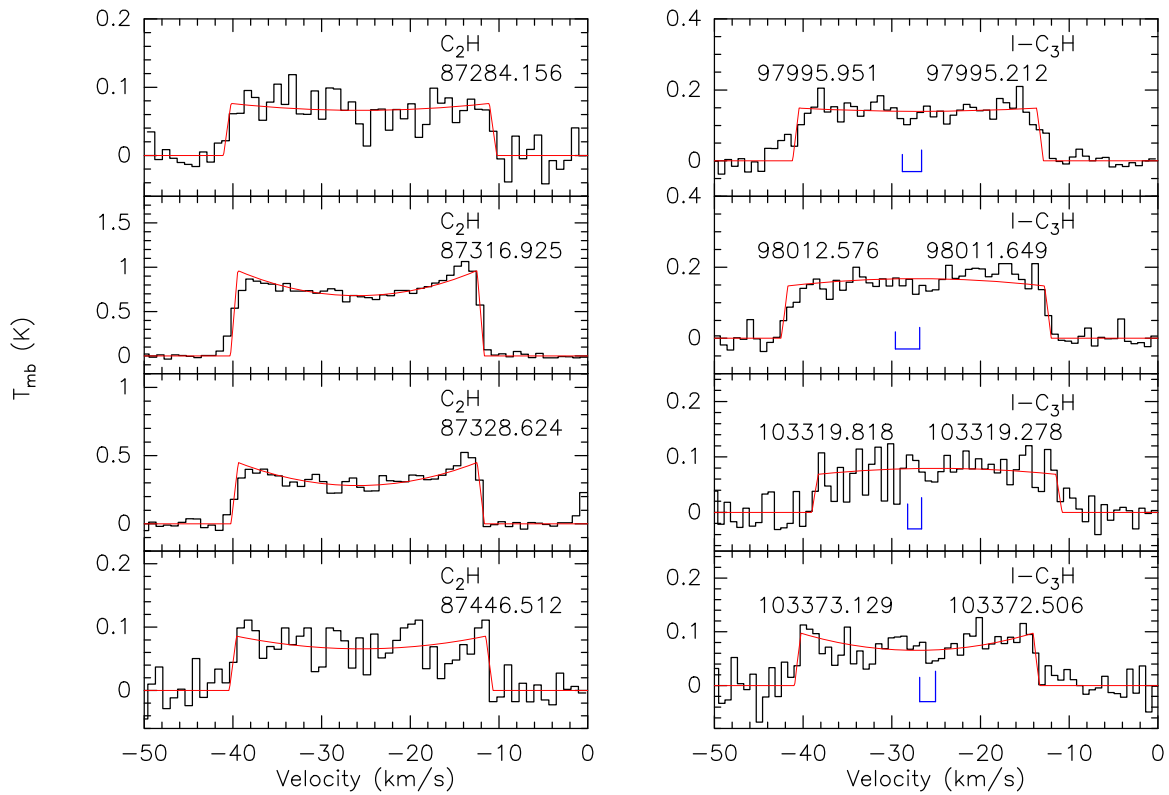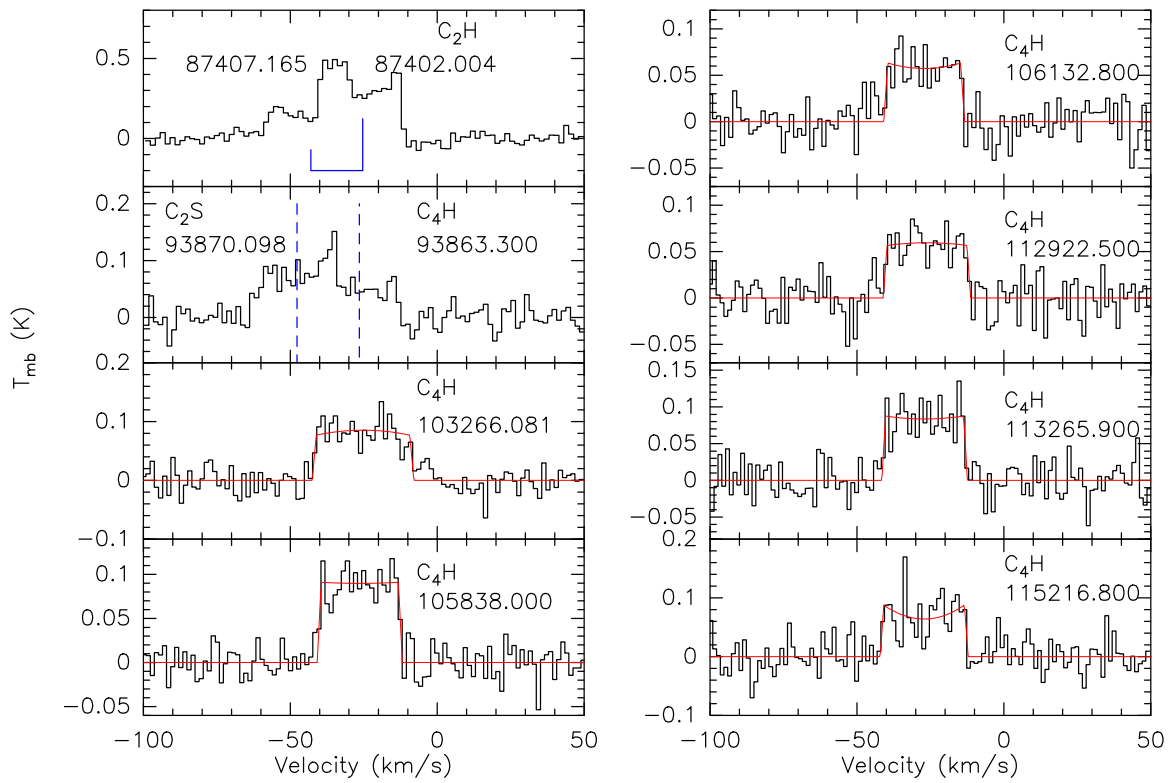
Figure C1. Same as Figure 2 but for C_2H and I-C_3H. The solid blue line indicates the hfs components of the molecule. The rest frequencies in MHz are shown in each panel's upper right corner for single structure components, and in the upper left and right corners for lines with two fine structure components.
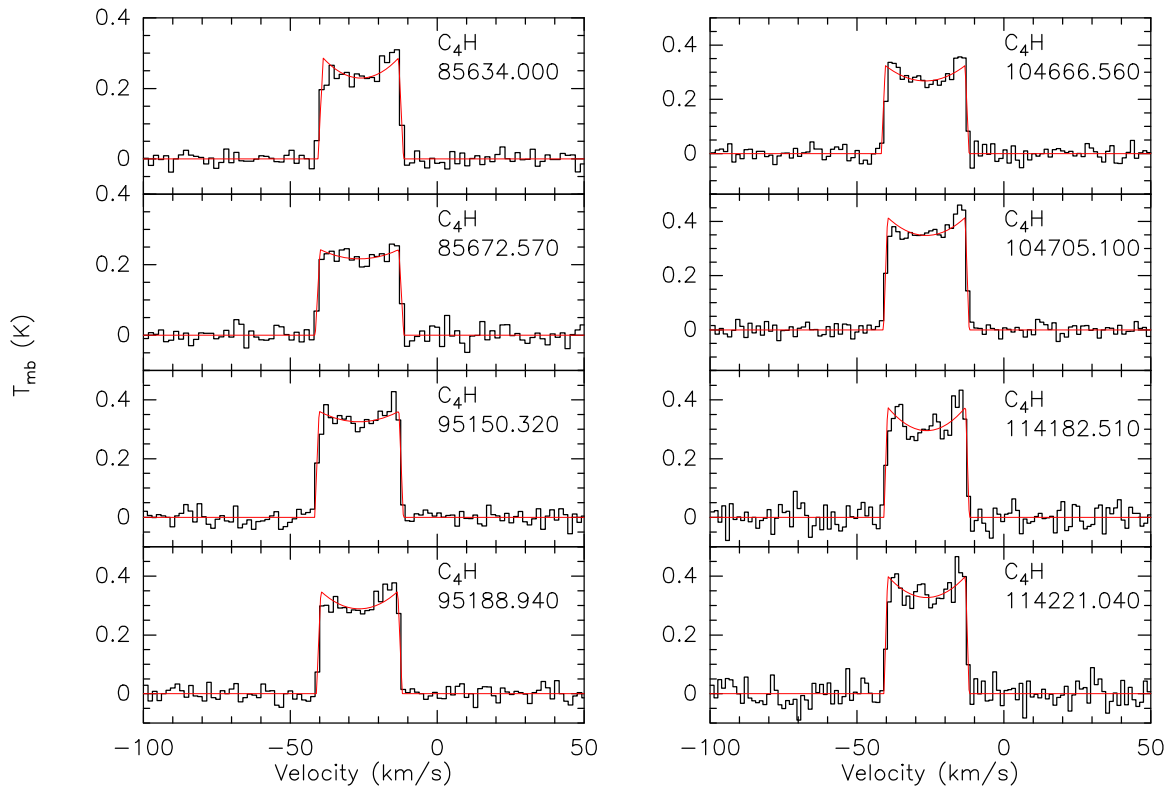
Figure C2. Same as Figure 2 but for C_4H.

Figure C3. Same as Figures 2 and C1 but for C_2H, $C_4H(\nu = 1)$, C_2S and CN. The blue-dashed lines represent the blended spectral lines.
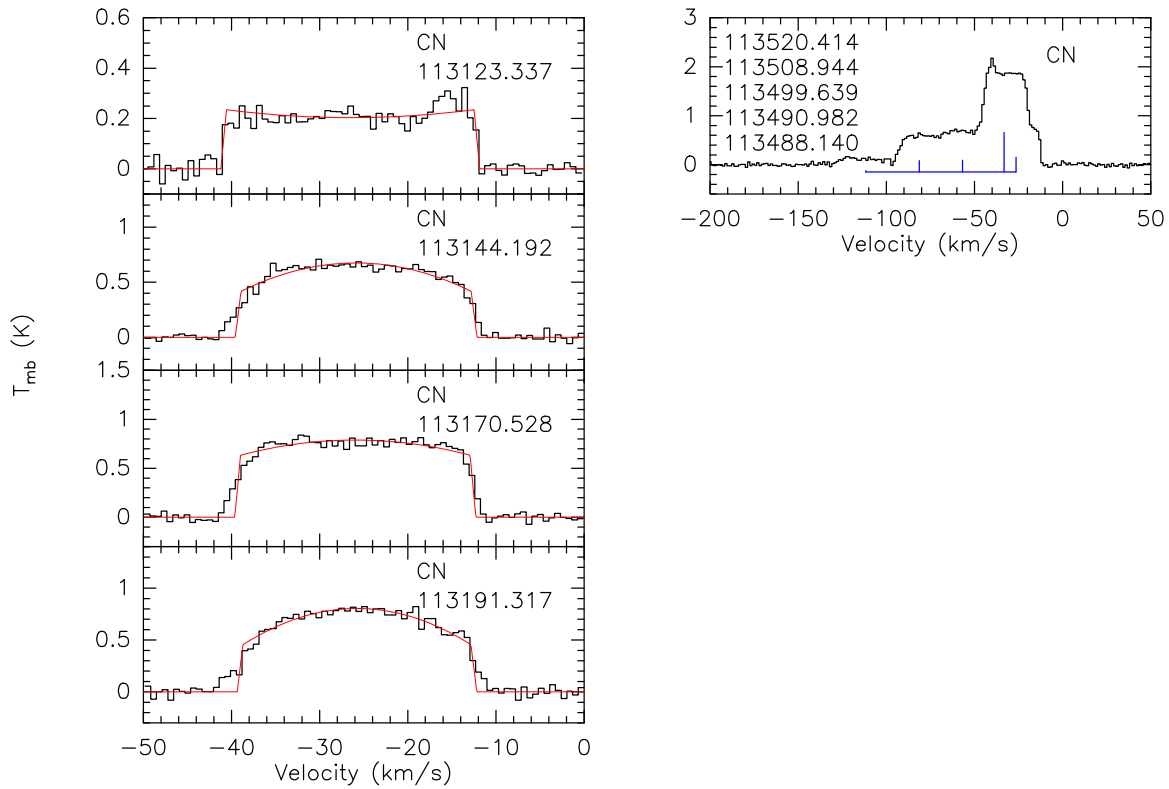
Figure C4. Same as Figures 2 and C1 but for CN. The rest frequencies in MHz of spectral lines of more than two fine structure components are displayed in the upper left corner of each panel.
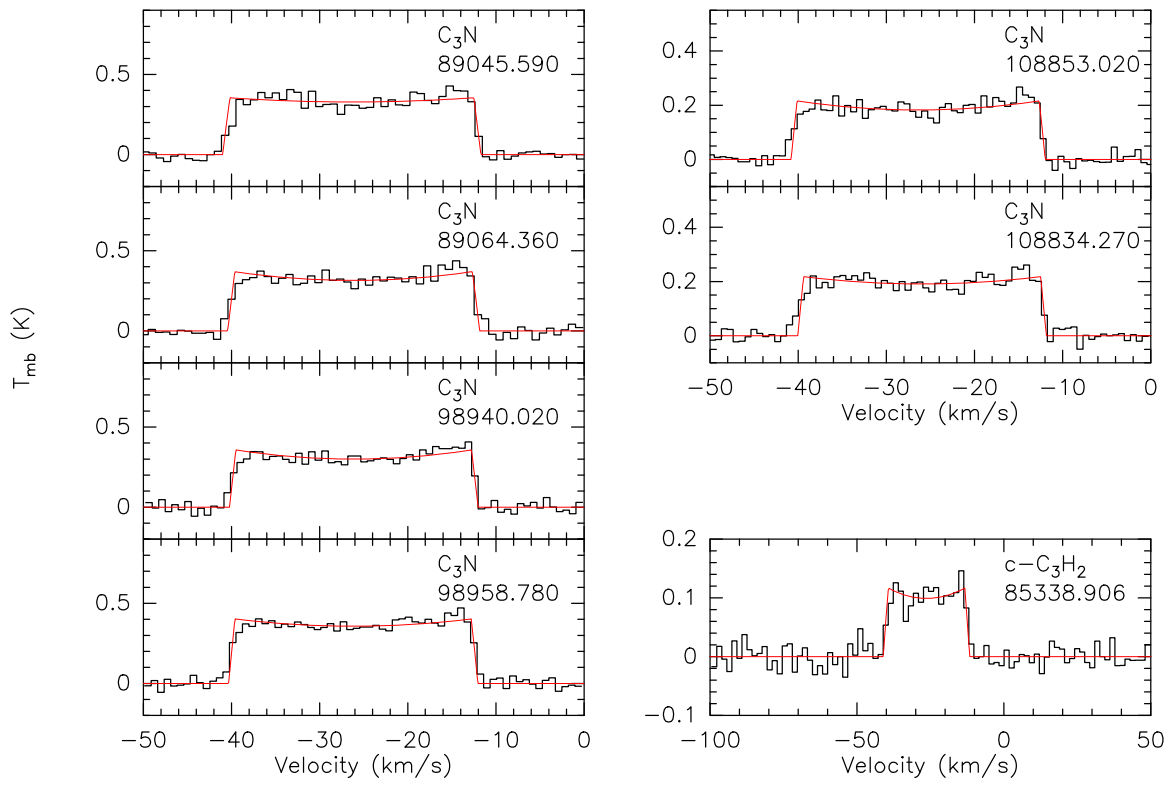
Figure C5. Same as Figure 2 but for C₃N and *c*-C₃H₂.
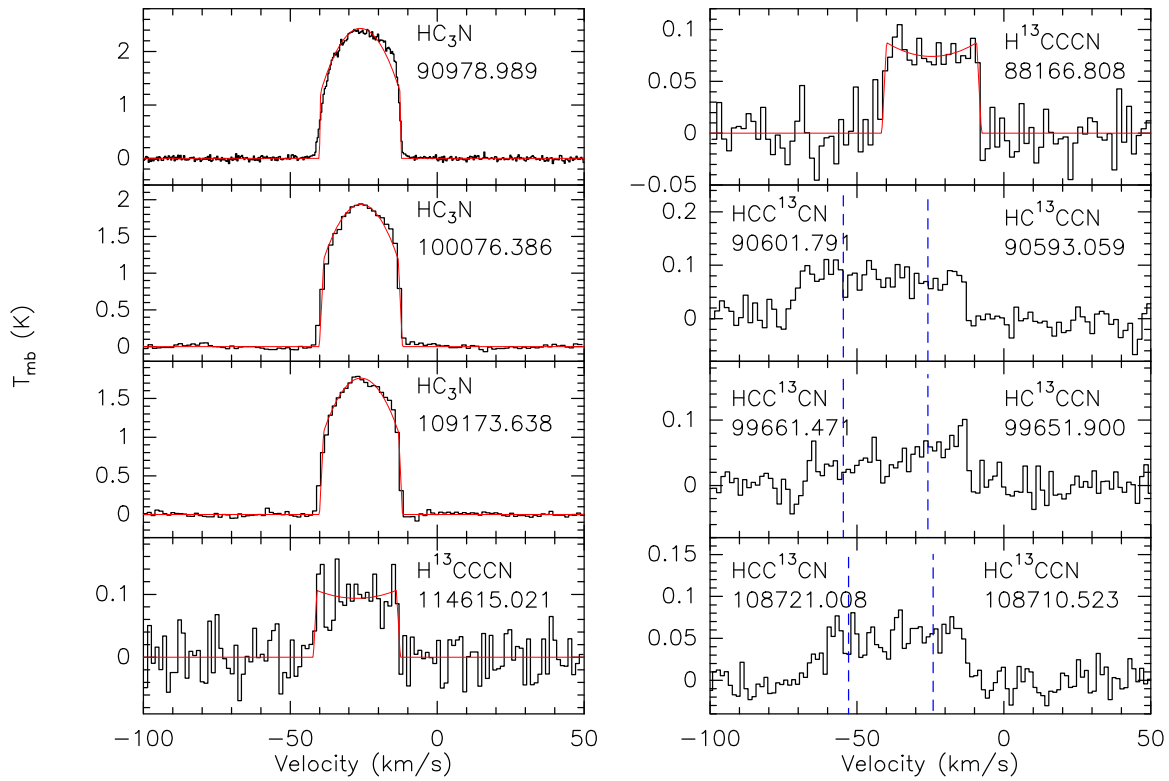
Figure C6. Same as Figures 2 and C3 but for HC₃N, and its isotopologues.
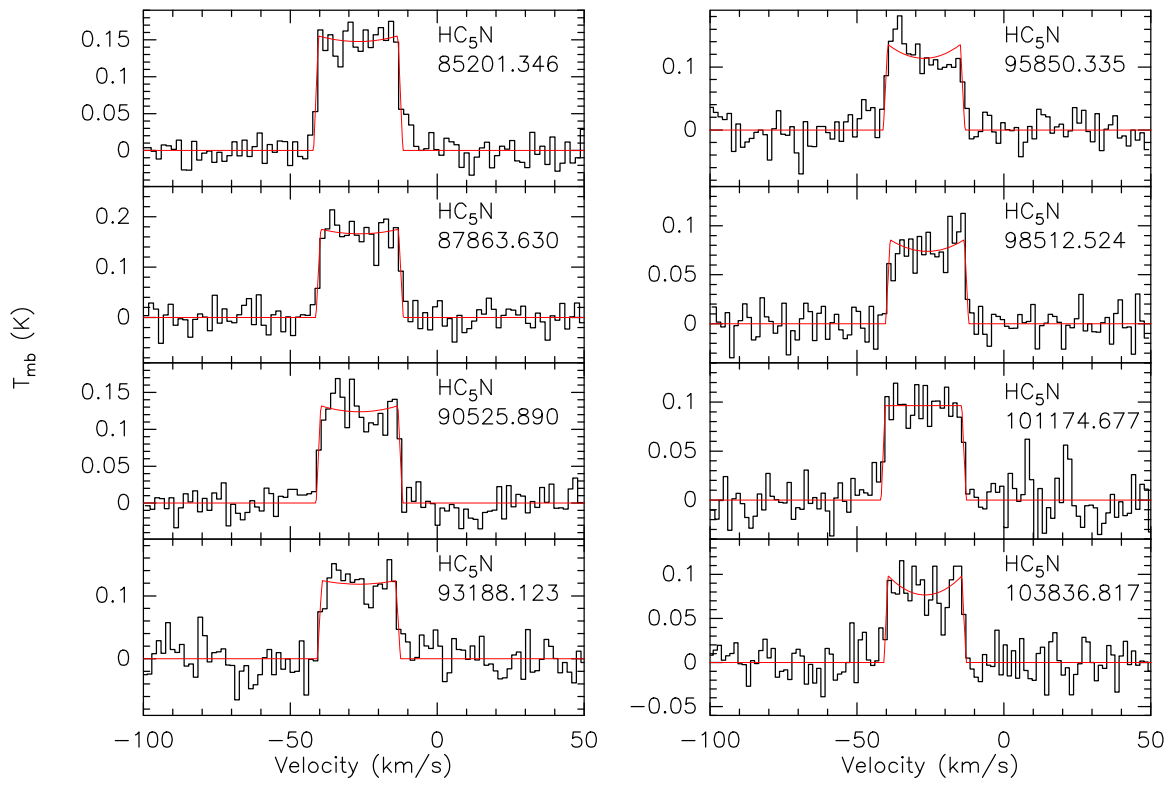
Figure C7. Same as Figure 2 but for HC$_5$N.
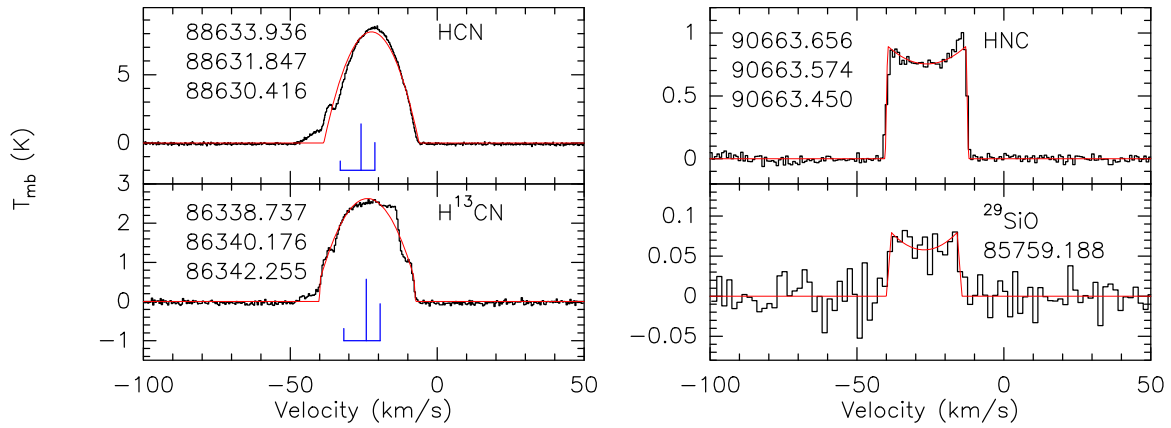
Figure C8. Same as Figures 2 and C1 but for HCN, H^{13}CN, HNC, and ^{29}SiO.
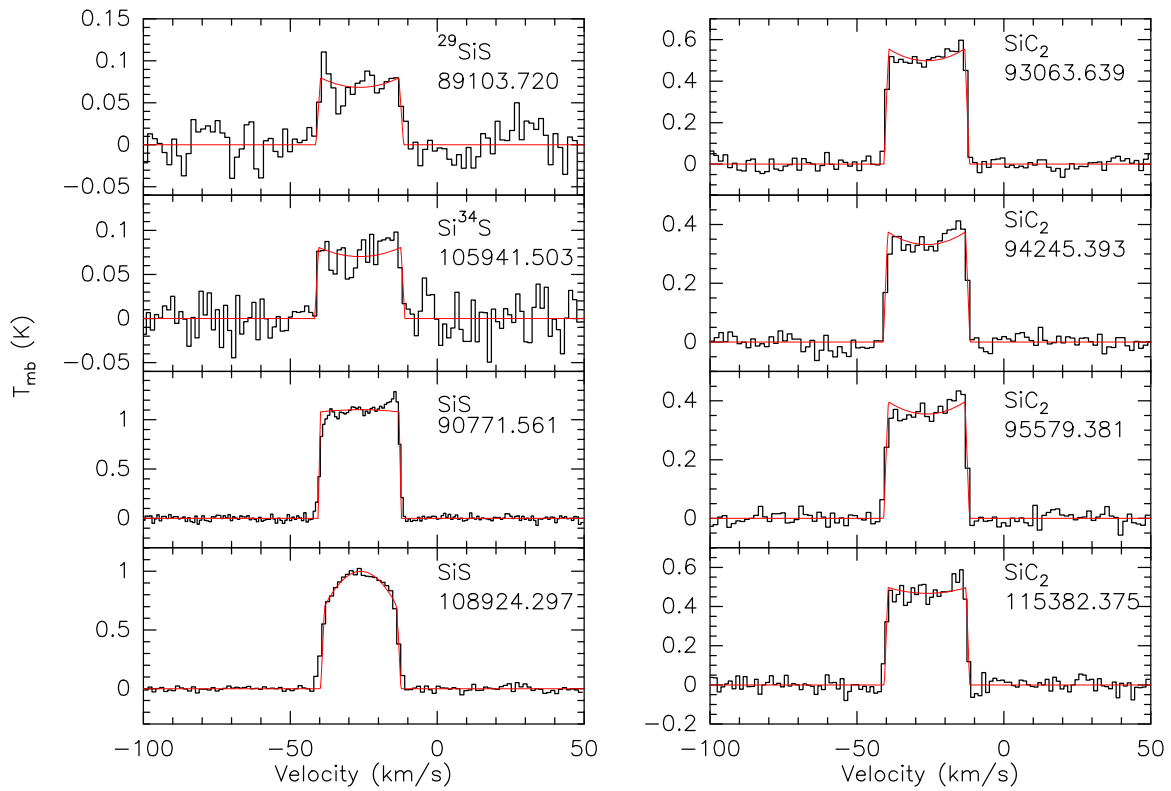
Figure C9. Same as Figure 2 but for SiS, ^{29}SiS, Si^{34}S and SiC$_2$.
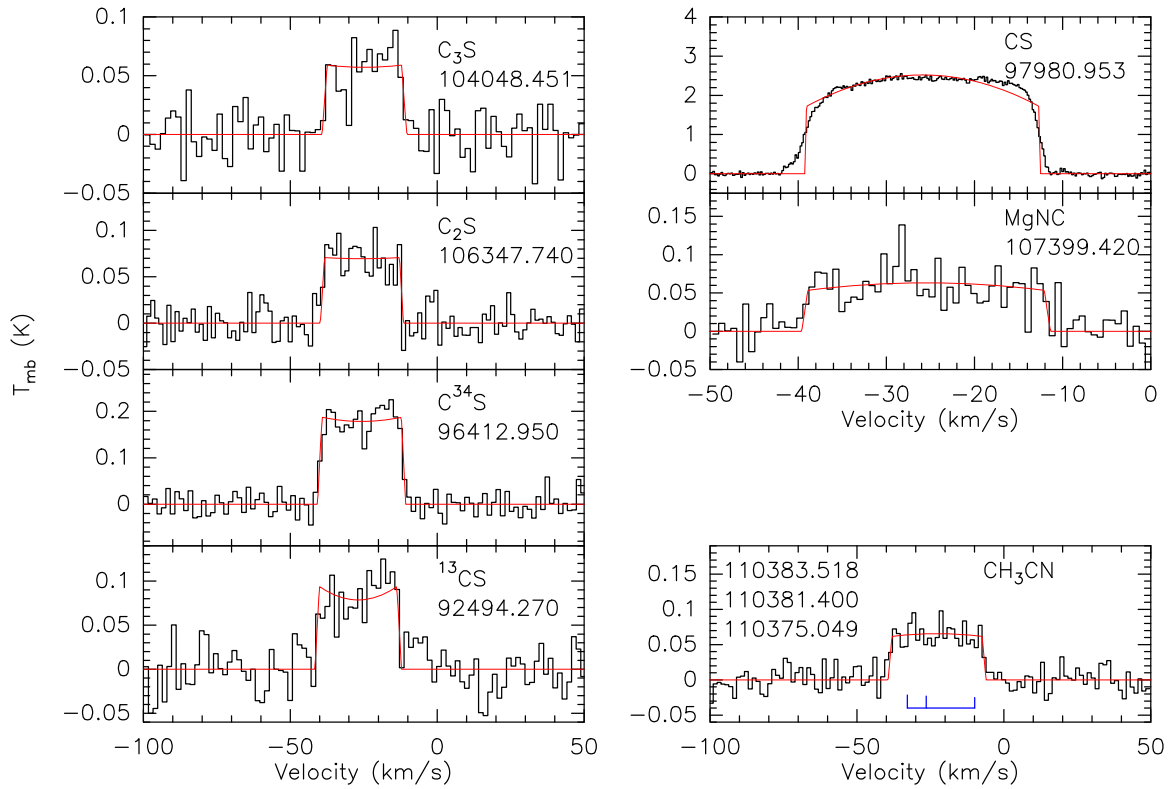
Figure C10. Same as Figures 2 and C1 but for CS, ^{13}CS, C^{34}S, C$_2$S, C$_3$S, MgNC, and CH$_3$CN.

Appendix D
Detected Species

A detailed description of the detected molecules, together with their previous observations, is provided in this appendix.

C_2H. The ethynyl radical C_2H was first detected and identified by Tucker et al. (1974) in several galactic sources, including IRC+10216. In this source, the $N = 1$–0 to $N = 4$–3 and $N = 6$–5 to $N = 9$–8 transitions of C_2H have been reported by De Beck et al. (2012). We detected the two spin-rotation fine-structure components of C_2H $N = 1$–0 ($J = 3/2$–1/2 and $J = 1/2$–1/2) in which the nuclear spin of hydrogen further causes the spin rotation to split into six hyperfine components: ($J = 3/2$–1/2, $F = 1$–1), ($J = 3/2$–1/2, $F = 2$–1), ($J = 3/2$–1/2, $F = 1$–0), ($J = 1/2$–1/2, $F = 1$–1 and $F = 0$–1), and ($J = 1/2$–1/2, $F = 1$–0). Among these components, C_2H ($J = 1/2$–1/2, $F = 1$–1) is blended with C_2H ($J = 1/2$–1/2, $F = 0$–1), producing two blended U-shaped spectral lines with the overlapping part showing stronger intensity than both sides. The transitions are presented in the left panel of Figure C1 and the top left panel of Figure C3. These spectral lines have also been detected by Johansson et al. (1984), Truong-Bach et al. (1987), and Kahane et al. (1988).

l-C_3H. The linear propynylidyne radical l-C_3H was initially identified by Thaddeus et al. (1985a) in IRC+10216 and TMC-1. Interestingly, Johansson et al. (1984) had previously detected l-C_3H at frequencies of 76,202, 97,995, and 98,011 MHz, but had classified these spectral lines as U lines and presumptively attributed them to transitions of l-C_3H. The $J = 3/2$–1/2, $J = 13/2$–11/2, and $J = 21/2$–19/2 transitions of this molecule have also been detected in other line surveys in this source (Kawaguchi et al. 1995; He et al. 2008). The right panel of Figure C1 shows eight hyperfine components that we have identified from the l-C_3H rotational lines $^2\Pi_{1/2}$ $J = 9/2$–7/2 ($F = 5$–4e, $F = 4$–3e, $F = 5$–4f, $F = 4$–3f) and $^2\Pi_{3/2}$ $J = 9/2$–7/2 ($F = 5$–4f, $F = 4$–3f, $F = 5$–4e, $F = 4$–3e). These transitions have been previously reported by Thaddeus et al. (1985a), Yamamoto et al. (1987), and Nyman et al. (1993).

C_4H. The butadiynyl radical $C_4H(\nu = 0)$ was first identified by Guélin et al. (1978) in the CSE of IRC+10216. Yamamoto et al. (1987) subsequently confirmed the transitions of C_4H in the CSE of IRC+10216 caused by the $^2\Pi_{1/2}$, $^2\Pi_{3/2}$, and Δ states through the use of experimental microwave spectroscopy. Further, other transitions of C_4H have also been detected in this source such as $N = 2$–1, $N = 3$–2 through $N = 5$–4, $N = 8$–7, $N = 14$–13 through $N = 16$–15, and $N = 24$–23 through $N = 28$–27 (Johansson et al. 1984; Kawaguchi et al. 1995; He et al. 2008; Gong et al. 2015). A total of 15 transitions of C_4H have been detected in our work. There are four rotational transitions ($N = 9$–8 through $N = 12$–11) of $C_4H(\nu = 0)$, each of these rotational transitions is split into spin-rotation doublets due to fine structure, and these are presented in Figure C2. Additionally, seven transitions of $C_4H(\nu = 1)$ are shown in Figure C3. However, the $^2\Pi_{1/2}$ C_4H $J = 19/2$–17/2, $\nu7 = 1f$ line (93,863.300 MHz) is blended with C_2S $N = 8$–7 and $J = 7$–6 (93870.098 MHz), as shown in the second figure in the left panel of Figure C3.

CN. The rotational emission from the cyanide radical CN was first detected by Jefferts et al. (1970a) toward W 51. Subsequently, the $N = 1-0$ transition of this molecule was also detected in IRC+10216 (Wilson et al. 1971). Further transitions such as $N = 2$–1 and $N = 3$–2 of CN were also detected in this source by Avery et al. (1992). We have detected the two spin-rotation fine-structure lines of CN $N = 1$–0 ($J = 3/2$–1/2 and $J = 1/2$–1/2), which are then further split into nine hyperfine components, due to the nuclear spin of nitrogen. These components include $J = 3/2$–1/2 ($F = 3/2$–1/2, $F = 5/2$–3/2, $F = 1/2$–1/2, $F = 3/2$–3/2, $F = 1/2$–3/2) and $J = 1/2$–1/2 ($F = 1/2$–1/2, $F = 1/2$–3/2, $F = 3/2$–1/2, $F = 3/2$–3/2). The spectral line profiles are shown in Figure C4, although we note that the five hyperfine lines of CN $N = 1$–0, $J = 3/2$–1/2 are blended.

C_3N. Guélin & Thaddeus (1977) detected a new molecule toward the CSE of IRC+10216, identifying it as the cyanoethynyl radical C_3N based on theoretical considerations. The $N = 2$–1, $N = 3$–2 through $N = 5$–4, $N = 8$–7 through $N = 11$–10, $N = 13$–12, $N = 14$–13 through $N = 17$–16, $N = 23$–22, $N = 24$–23, and $N = 27$–26 transition lines of C_3N in this source have been reported (Guélin & Thaddeus 1977; Johansson et al. 1984; Henkel et al. 1985; Kawaguchi et al. 1995; Cernicharo et al. 2000; He et al. 2008; Thaddeus et al. 2008; Gong et al. 2015). A total of six fine structure lines of C_3N have been detected in our work, and displayed in Figure C5. These lines derive from three rotational transitions ($N = 9$–8 through $N = 11$–10) of C_3N. All of the detected rotational transition lines are split into spin-rotation doublets, due to the interactions of fine structure.

c-C_3H_2. A strong unidentified line at 85.339 GHz was first detected by Thaddeus et al. (1981) toward Ori A, Sgr B2 (OH), and TMC-1. This line was subsequently identified as cyclopropenylidene c-C_3H_2 by Thaddeus et al. (1985b). The rotational transitions of c-C_3H_2 have also been detected in other spectral line surveys of this source (Kawaguchi et al. 1995; Cernicharo et al. 2000; He et al. 2008; Gong et al. 2015; Zhang et al. 2017). In our work, we have detected one transition of c-C_3H_2, shown at the bottom of the right panel in Figure C5.

HC_3N. Cyanoacetylene, HC_3N, was detected by Turner (1970, 1971) toward Sgr B2. Morris et al. (1975) also detected this molecule in IRC+10216 using the NRAO 11 m telescope. Various transitions of HC_3N and its isotopologues have been reported in this source. For instance, the $J = 2$–1 transitions of HC_3N, $H^{13}CCCN$, $HC^{13}CCN$, and $HCC^{13}CN$ were detected by Zhang et al. (2017), the $J = 4$–3 and $J = 5$–4 transitions of HC_3N and its isotope were detected by Kawaguchi et al. (1995), and the $J = 9$–8 and $J = 10$–9 transitions of HC_3N and its isotope were detected by Johansson et al. (1984). Nyman et al. (1993) detected HC_3N $J = 10$–9 and $J = 12$–11 in this source, as well as $HC^{13}CCN$ and $HCC^{13}CN$. We detected three lines ($J = 10$–9 through $J = 12$–11) of HC_3N and two relatively weak isotopic lines ($H^{13}CCCN$ $J = 10$–9 and $H^{13}CCCN$ $J = 13$–12). We also detected three transitions of $HC^{13}CCN$ ($J = 10$–9 through $J = 12$–11) and three transitions of $HCC^{13}CN$ ($J = 10$–9 through $J = 12$–11), but all detected $HC^{13}CCN$ lines are blended with $HCC^{13}CN$ transitions. These lines are shown in Figure C6. To the best of our knowledge, the $J = 13$–12 transition of $H^{13}CCCN$ is detected in IRC+10216 for the first time.

HC_5N. Cyanodiacetylene, HC_5N, is a linear molecule, which was observed in Sgr B2 by Avery et al. (1976). In IRC+10216, Winnewisser & Walmsley (1978) confirmed the HC_5N transition reported by Churchwell et al. (1978). The $J = 2$–1, $J = 5$–4 to $J = 9$–8, $J = 28$–27 to $J = 40$–39, and $J = 49$–48 to $J = 54$–53 transitions of HC_5N have been detected in IRC +10216 (Johansson et al. 1984; Cernicharo et al. 1986b, 2000; Araya et al. 2003; Gong et al. 2015; Agúndez et al. 2017;

Zhang et al. 2017). We have detected nine rotational transition lines of HC$_5$N from $J = 32$–31 to $J = 40$–39. These lines are shown in Figures 2 and C7.

HCN. Hydrogen cyanide, HCN, was first detected in W49, W51, W3 (OH), Orion A, DR 21 (OH), and Sgr A (NH$_3$A) (Howard et al. 1970; Snyder & Buhl 1971). HCN has been detected in IRC+10216 by Morris et al. (1971). The transitions of $J = 2$–1 (Menten et al. 2018), $J = 3$–2 and $J = 4$–3 (Avery et al. 1992) of HCN, and the $J = 1$–0, $J = 3$–2, $J = 4$–3, and $J = 8$–7 transitions of H^{13}CN (Schöier et al. 2007) have been detected as well. The $J = 1$–0 transitions from HCN and H^{13}CN were detected in our line survey. The HCN $J = 1$–0 transition contains hfs, so the frequency intervals between the individual features are too small (Olofsson et al. 1982) causing us to detect both absorption and emission in the line profile in Figure C8 (see also Dayal & Bieging 1995).

HNC. An unidentified emission line at 89.190 GHz was detected by Buhl & Snyder (1970) in W3(OH), Orion, L134, Sgr A (NH$_3$A), and W 51, first attributed by Snyder & Buhl (1972) to the $J = 1$–0 transition of hydrogen isocyanide HNC. Brown et al. (1976) reported that HNC had been detected in IRC+10216. Using the IRAM 30 m telescope and the HIFI instrument on board the Herschel Space Observatory, the transitions of HNC $J = 3$–2, $J = 1$–0, and $J = 6$–5 through $J = 12$–11 were detected in IRC+10216 (Daniel et al. 2012). In our work, we detected the $J = 1$–0 transition from HNC, as shown in Figure C8. Although HNC $J = 1$–0 contains hfs, the frequency interval between these structures is too small to be detected in IRC+10216 (Olofsson et al. 1982).

CO. Carbon monoxide, CO, at 115 GHz was observed by Jefferts et al. (1970b) in at least five galactic sources, including Orion A, Sgr A, Sgr B2, W39, and W51. Subsequently, CO was also observed in IRC+10216 (Solomon et al. 1971). Other transitions of CO and ^{13}CO in IRC+10216 have also been reported (Avery et al. 1992; Cernicharo et al. 2015a). In our work, we have detected the $J = 1$–0 transitions from CO and ^{13}CO, as shown in Figure 2.

SiO. The $J = 3$–2 transition of silicon monoxide, SiO, was detected in Sgr B2 by Wilson et al. (1971). Subsequently, Morris et al. (1975) observed the $J = 2$–1 transition of SiO in the CSE of IRC+10216. The transitions observed by previous research include $J = 1$–0 through $J = 8$–7 (Avery et al. 1992; Kawaguchi et al. 1995; Cernicharo et al. 2000; He et al. 2008; Tenenbaum et al. 2010b; Agúndez et al. 2012). In our study, we detected the $J = 2$–1 rotational transitions of SiO and ^{29}SiO, and their line profiles are illustrated in Figures 2 and C8.

SiS. Silicon monosulfide, SiS, was first detected by Morris et al. (1975) toward IRC+10216. The maser and quasi-thermal emission of the SiS $J = 1$–0, and $J = 2$–1 lines in the CSE of IRC+10216 have been studied by Gong et al. (2017). The transitions of SiS and ^{29}SiS observed by Agúndez et al. (2012) include $J = 5$–4, $J = 6$–5, and $J = 8$–7 through $J = 19$–18. Among them, the $J = 11$–10, $J = 14$–13, and $J = 15$–14 transitions are masers, which was also reported by Fonfría Expósito et al. (2006) and Fonfría et al. (2018). The $J = 5$–4, $J = 6$–5, and $J = 8$–7 through $J = 20$–19 from Si^{34}S were also detected by Agúndez et al. (2012). We have detected the $J = 5$–4 and $J = 6$–5 lines from SiS, as well as the $J = 5$–4 transitions from ^{29}SiS and the $J = 6$–5 line from Si^{34}S. The line profiles are presented in Figure C9.

SiC$_2$. Silacyclopropynylidene, SiC$_2$, was the first ring molecule identified in an astronomical source. Its millimeter-

and centimeter-wave transitions were identified by Thaddeus et al. (1984) and Snyder et al. (1985), respectively, in the CSE of IRC+10216. High-resolution spectra (channel width 195 kHz) of SiC$_2$ at 70–350 GHz (Cernicharo et al. 2018), 554.5–636.5 GHz (Cernicharo et al. 2010b), and the spatial distribution of SiC$_2$ in IRC+10216 (Fonfría et al. 2014; Velilla Prieto et al. 2015; Velilla Prieto et al. 2019) have also been reported. We have detected the $J_{K_a,K_c} = 4_{0,4}$–$3_{0,3}$, $J_{K_a,K_c} = 4_{2,3}$–$3_{2,2}$, $J_{K_a,K_c} = 4_{2,2}$–$3_{2,1}$, and $J_{K_a,K_c} = 5_{0,5}$–$4_{0,4}$ transitions of SiC$_2$, and the line profiles are shown in Figure C9.

CS. The $J = 3$–2 transition of carbon monosulfide, CS, was detected in IRC+10216, Orion A, W51, and DR 21 by Penzias et al. (1971). The transitions of $J = 1$–0 through $J = 7$–6 from CS and the transitions of $J = 1$–0 through $J = 3$–2 and $J = 5$–4 through $J = 7$–6 from ^{13}CS and C^{34}S in the CSE of IRC +10216 have also been extensively reported (Johansson et al. 1984; Avery et al. 1992; Kawaguchi et al. 1995; Lucas et al. 1995; He et al. 2008; Agúndez et al. 2012; Velilla Prieto et al. 2019). We detected strong CS $J = 2$–1 emission and its isotopic lines, ^{13}CS $J = 2$–1 and C^{34}S $J = 2$–1. The line profiles of CS, ^{13}CS, and C^{34}S are depicted in Figure C10.

C$_2$S. An unknown interstellar line at 45.379 GHz from Sgr B2, TMC-1, TMC-1 (NH$_3$), and TMC2 was detected by Suzuki et al. (1984). Kaifu et al. (1987) detected seven unknown strong lines in the frequency regions of 22–24 and 36–50 GHz from TMC-1. The four unknown lines at 45.379, 43.981, 38.866, and 22.344 GHz were identified to trace the linear C$_2$S radical (Saito et al. 1987). Twelve spectral lines of C$_2$S in the frequency range of 81–157 GHz have also been detected by Cernicharo et al. (1987a) toward IRC+10216. In our work, we have detected two transitions of C$_2$S, $N = 9$–8, $J = 8$–7, and $N = 8$–7, $J = 7$–6, but the transition of C$_2$S $N = 8$–7, $J = 7$–6 is blended with the $^2\Pi_{1/2}$ C$_4$H $\nu 7 = 1f$ line. The second figure in the left panel of Figure C3 shows the C$_2$S spectral line blended with C$_4$H. Figure C10 shows a single C$_2$S spectral line.

C$_3$S. Kaifu et al. (1987) detected seven unknown strong lines in the frequency regions of 22–24 and 36–50 GHz from TMC-1, of which three were identified as linear C$_3$S radicals at 3.123, 40.465, and 46.246 GHz by Yamamoto et al. (1987). Meanwhile, Cernicharo et al. (1987a) used the IRAM 30 m telescope to detect 11 transition lines of C$_3$S between 75 and 168 GHz in IRC+10216. Only one transition line of C$_3$S $J = 18$–17 was detected in our work, and the spectral line is shown in Figure C10.

MgNC. Guélin et al. (1986) observed six unidentified spectral lines in IRC+10216 with the IRAM 30 m telescope, and they considered that these molecules were likely to be HSiCC (or its isomer HCCSi) or HSCC. Subsequently, Kawaguchi et al. (1993) detected linear MgNC radicals for the first time using microwave spectroscopy in the laboratory, and they confirmed that these unrecognized lines were linear MgNC free radicals.

The $N = 2$–1 through $N = 4$–3 rotational transitions, as well as the rotational transitions of $N = 12$–11 and $N = 13$–12 of MgNC in the CSE of IRC+10216 have been observed by Kawaguchi et al. (1995), He et al. (2008), and Gong et al. (2015). In our work, we only detected the $N = 8$–7 $J = 19/2$–17/2 rotational transition of MgNC, which is displayed in the second subpicture of the right panel of Figure C10.

CH$_3$CN. Methyl cyanide, CH$_3$CN, has been detected by Solomon et al. (1971) in Sgr B and Sgr A. Johansson et al. (1984)

detected CH_3CN, the first species containing the methyl group, in IRC+10216. In this source, the $J = 2–1$ transitions in the $K = 0$ and $K = 1$ states of CH_3CN were detected by Kawaguchi et al. (1995). The $J = 8–7$, $J = 12–11$, and $J = 13–12$ transitions in the $K = 0, 1, 2, 3$ states, and the $J = 14–13$ transitions in the $K = 0$ and $K = 1$ states of CH_3CN were detected by He et al. (2008). Other higher J lines of CH_3CN in the frequency range of 293.9–354.8 GHz were observed by Patel et al. (2011). We only detected the $J = 6–5$ transitions in the $K = 0$, $K = 1$, and $K = 2$

states of CH_3CN, and these blended emission lines are shown in the last subpicture on the right panel of Figure C10.

Appendix E
Rotational Diagrams for the Identified Species

The rotational diagrams for the identified species from this survey are shown in Figures E1 and E2.
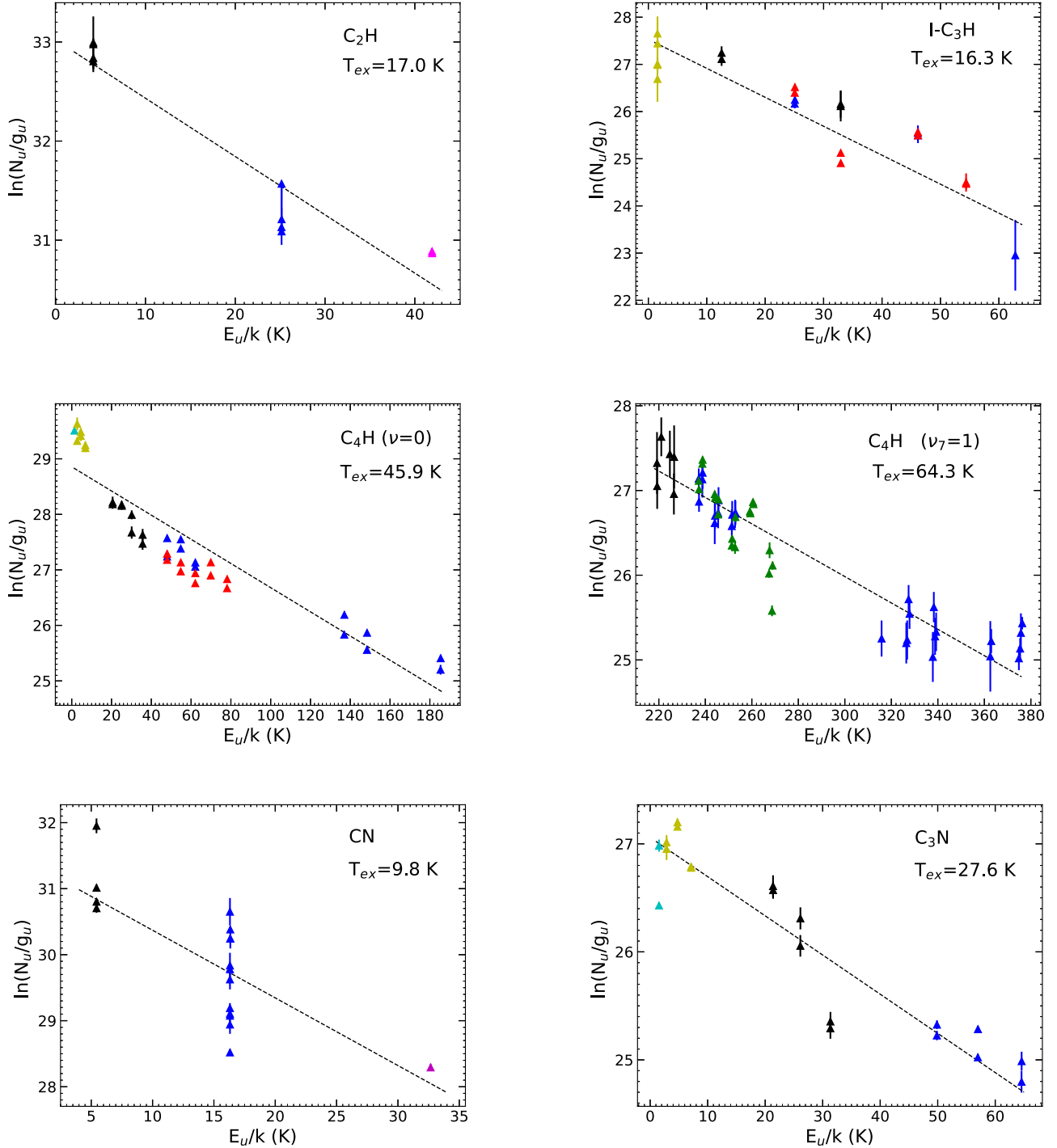
Figure E1. Rotational diagrams for the identified molecules in IRC+10216 in the λ 3 mm wavelength band. The results obtained from the linear least squares fitting are plotted in black-dashed lines. The adopted data points with error bars are from our PMO 13.7 m observations (black triangles), He et al. (2008) (blue triangles), Gong et al. (2015) (cyan triangles), Zhang et al. (2017) (dark orange triangles), Kawaguchi et al. (1995) (yellow-green triangles), Cernicharo et al. (2000) (red triangles), Agúndez et al. (2012) (green triangles), and Groesbeck et al. (1994) (magenta triangles), respectively. Note that the error bars are invisible if their values are smaller than the adopted data points.
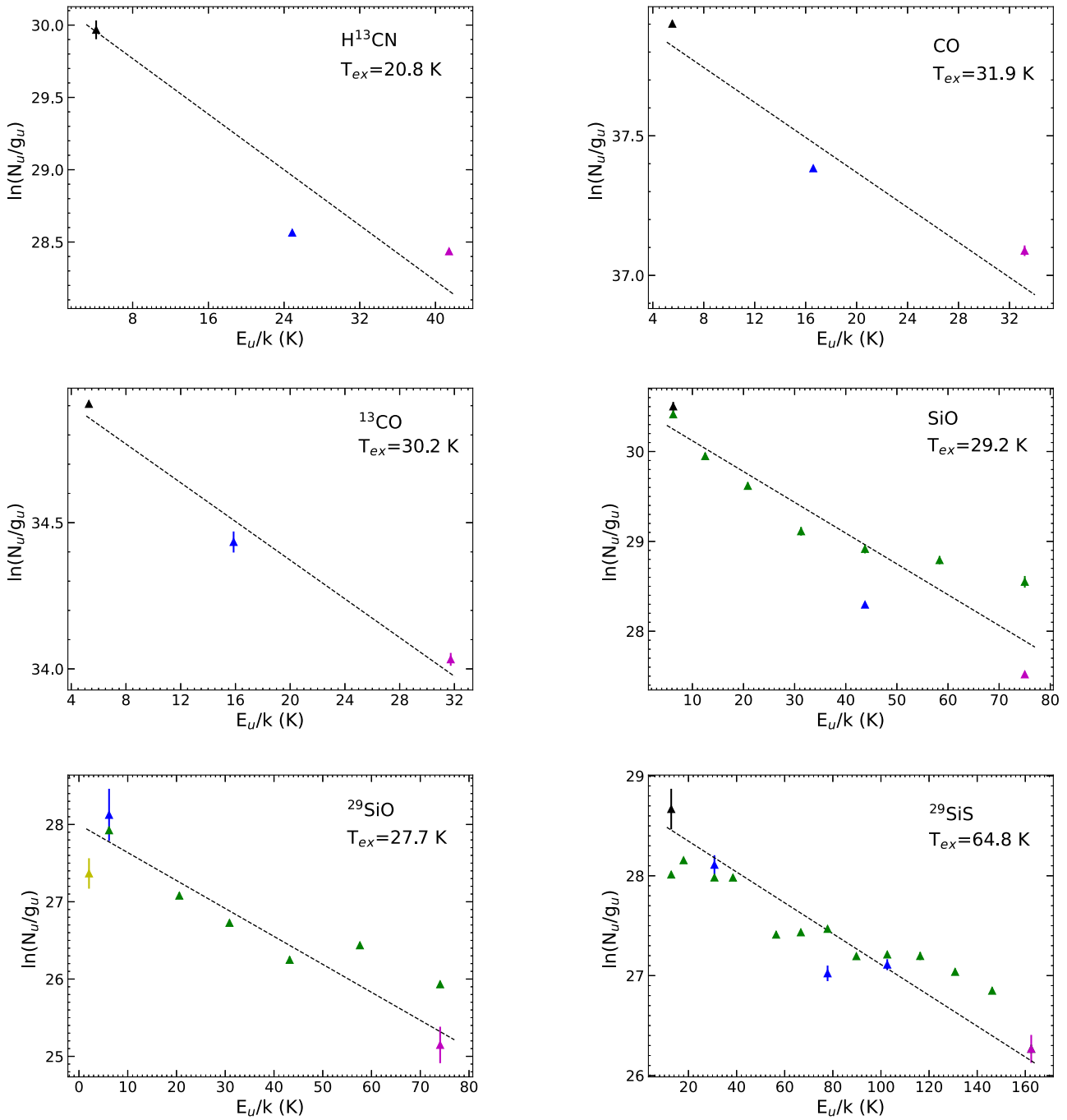
Figure E1. (Continued.)
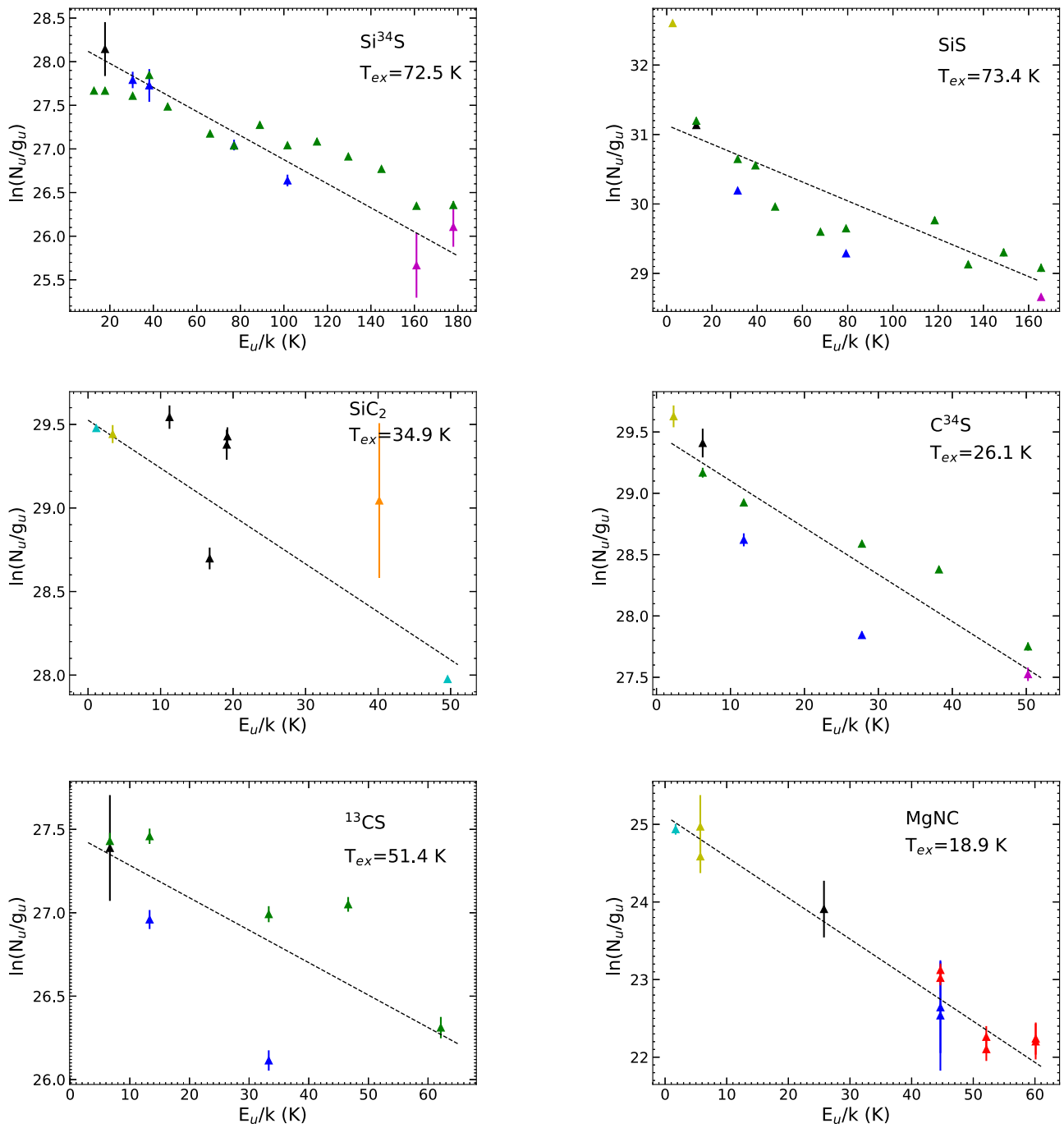
Figure E1. (Continued.)
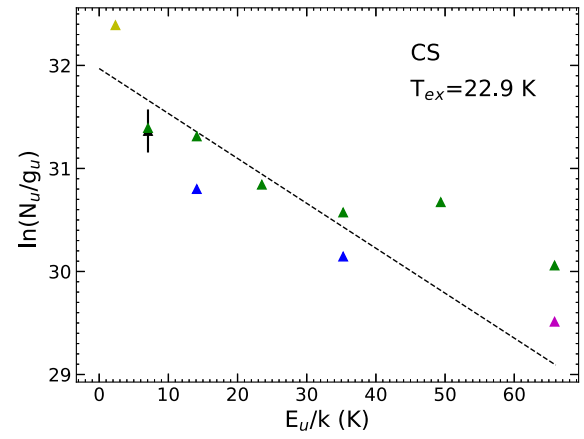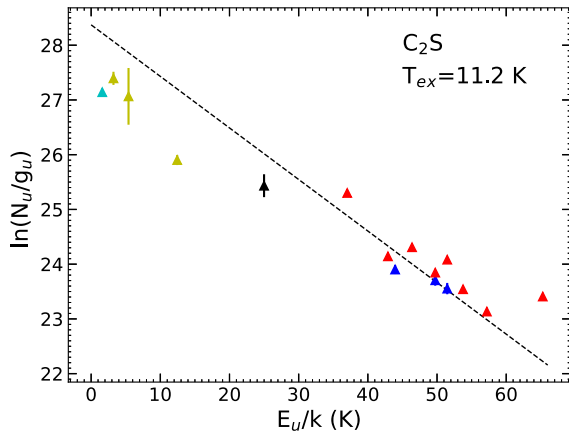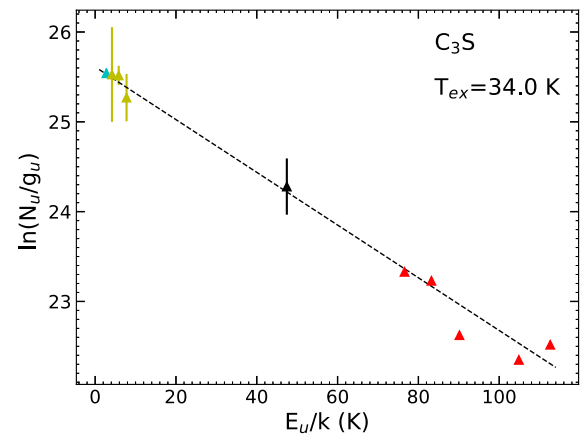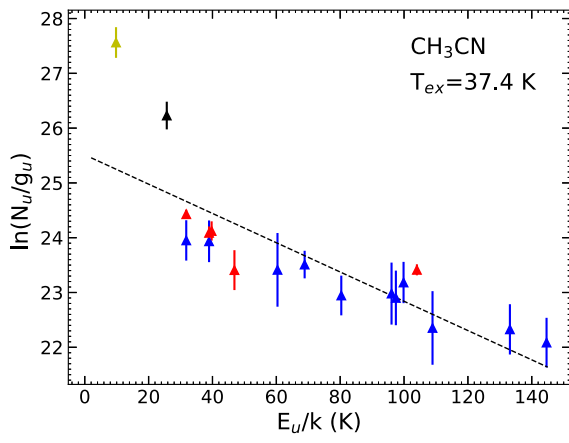
Figure E1. (Continued.)
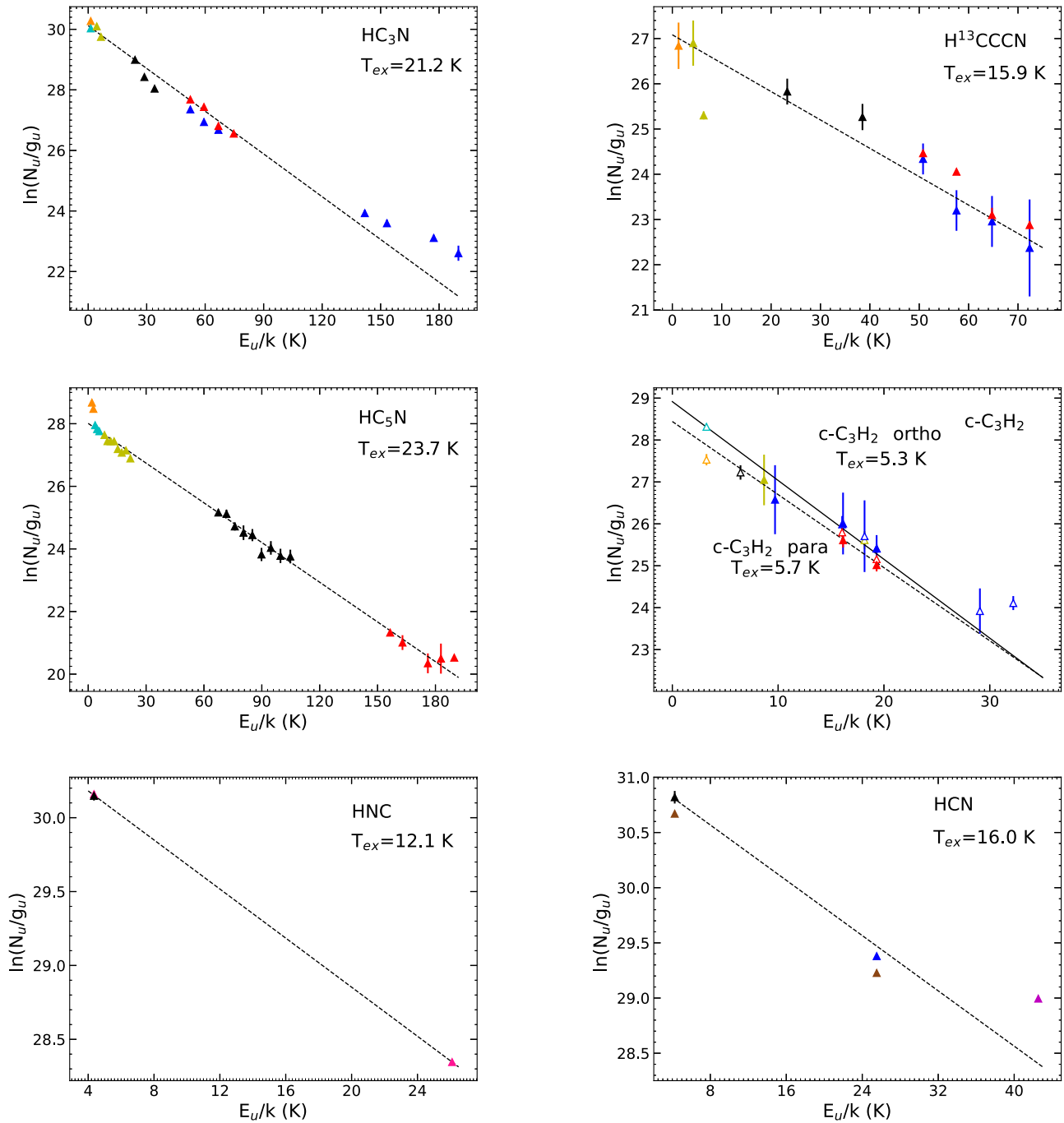
Figure E2. Same as Figure E1, but for different molecular species. Note, molecular c-C_3H_2 is separated into ortho (open triangles) and para (filled triangles) states and fitted in solid (ortho) and dotted (para) lines. The data shown in saddle-brown triangles with error bars are obtained from Nyman et al. (1993).

Appendix F
Multicomponents of the CSE Species

Both HC_3N and HC_5N in the CSE of IRC+10216 have two temperature components, tracing a warm region probed by high-energy rotational lines and a cooler region probed by low-energy lines. Bell et al. (1992b) find that HC_3N has a cold component with $T_{ex} = 12.7 \pm 1$ K and $N = (7.9 \pm 0.2) \times 10^{14}$ cm^{-2}, and a warm component with $T_{ex} = 48 \pm 6$ K and $N = (2.1 \pm 1.4) \times 10^{14}$ cm^{-2}. Meanwhile, they find that HC_5N has a cold component with $T_{ex} \sim 13$ K and $N = 3.2 \times 10^{14}$ cm^{-2} and a warm component with $T_{ex} \sim 25$ K and $N = 3.7 \times 10^{14}$ cm^{-2}. Zhang et al. (2017) also compared the excitation temperatures of HC_5N, HC_7N, and

HC_9N at different frequency ranges and found that the excitation temperature obtained by fitting the high rotation transition of these molecules was correspondingly higher, indicating that the high rotational transitions of these molecules in the CSE of IRC+10216 trace the warm inner molecular region. We also compare the excitation temperatures of HC_3N and HC_5N at different upper-state energy levels. Our results show that the excitation temperatures gradually increase with higher excited rotational transitions.

In Figures F1 and F2, we compare the excitation temperatures obtained from different upper-state energy levels. For HC_3N, the ratios of these are estimated to be scaled as $HC_3N(E_u/k < 10$ K): $HC_3N(20$ K $< E_u/k < 35$ K): HC_3N $(50$ K $< E_u/k < 80$ K): and HC_3N $(E_u/k > 140$ K$) = 1$: 1.7: 3.4: 5.9. The excitation
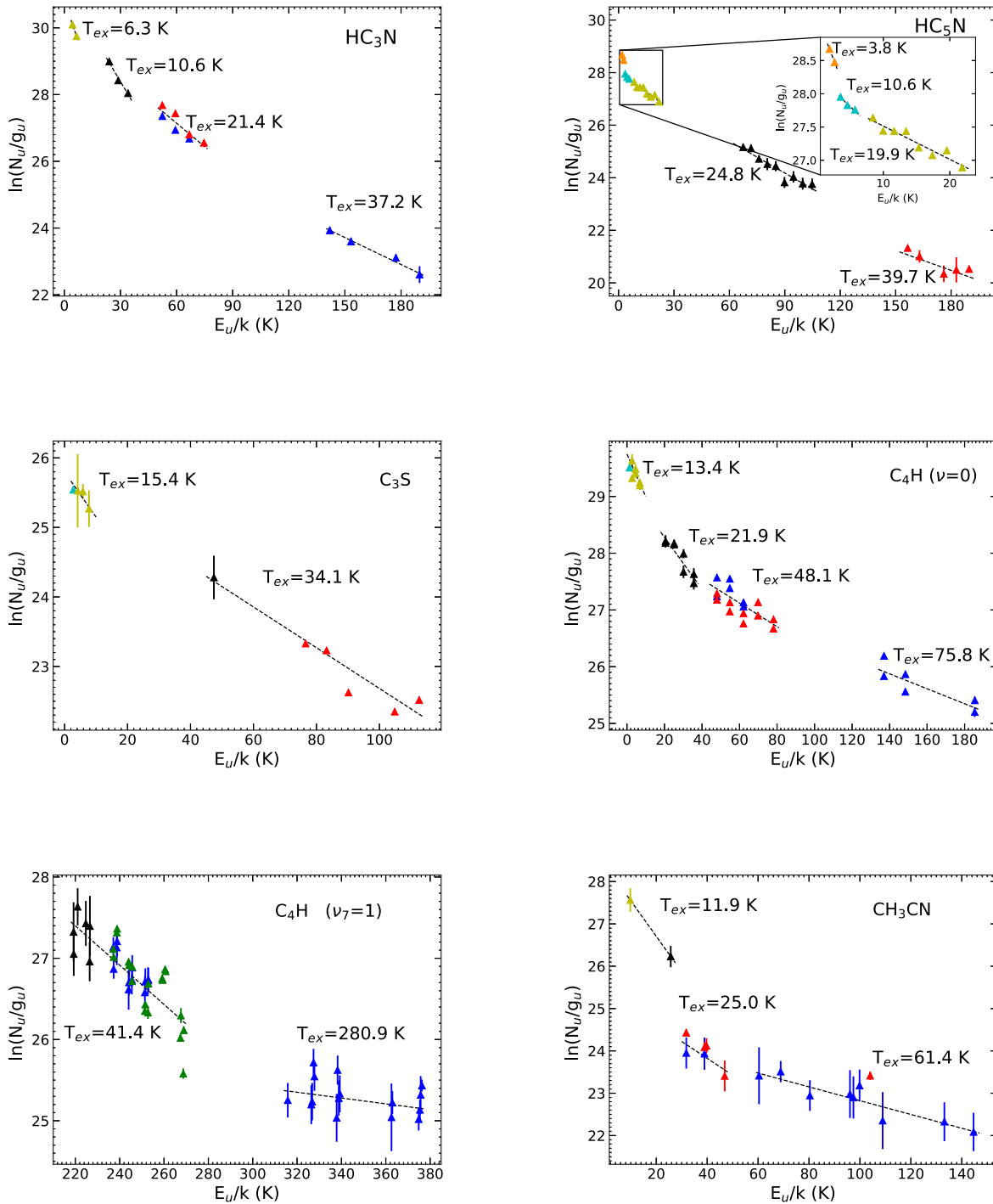
Figure F1. Multicomponents revealed in the rotational diagrams of several species: HC_3N, HC_5N, C_3S, C_4H ($\nu = 0$), C_4H ($\nu = 1$), and CH_3CN. The results obtained from the linear least squares fitting are plotted in black-dashed lines. The adopted data points with error bars are from our PMO 13.7 m observations (black triangles), He et al. (2008) (blue triangles), Gong et al. (2015) (cyan triangles), Zhang et al. (2017) (dark orange triangles), Kawaguchi et al. (1995) (yellow-green triangles), Cernicharo et al. (2000) (red triangles), Agúndez et al. (2012) (green triangles), and Groesbeck et al. (1994) (magenta triangles), respectively. Note that the error bars are invisible if their values are smaller than the adopted data points.

temperatures of HC_5N are estimated to be scaled as HC_5N ($E_u/k < 3$ K): $HC_5N(3 \text{ K} < E_u/k < 6 \text{ K})$: $HC_5N(8 \text{ K} < E_u/k < 25 \text{ K})$: HC_5N ($60 \text{ K} < E_u/k < 105 \text{ K})$: HC_5N ($E_u/k > 150 \text{ K}) = 1$: 2.8: 5.2: 6.5: 10.4. This indicates that the high-J transitions of the HC_3N molecules in the CSE of IRC+10216 also trace the warmer molecular regions.

Bell et al. (1993) find that C_3S also has at least two excitation temperature components, of which the excitation temperature of the low-energy part is about 17 K and that of the high energy

part is about 47 K. We also compare the excitation temperature of C_3S at different upper-state energies. When E_u/k is less than 10 K, the excitation temperature is 15.4 K, and when E_u/k is greater than 40 K, the excitation temperature is 34.1 K.

Our analysis using the rotational diagram method shows that C_4H ($\nu = 0$), C_4H ($\nu = 1$), CH_3CN, and SiS also have different excitation temperature components. Therefore, we also compared the excitation temperatures of these molecules at different upper-state energies. For CH_3CN, the scaled ratios are estimated

Table F1
Multicomponent Fits for C$_4$H, HC$_3$N, HC$_5$N, CH$_3$CN, C$_3$S, and SiS

Species	E_u/k (K)	T_{ex} (K)	N (cm^{-2})	$f(N/N_{H_2})$
HC$_3$N	$E_u/k < 10$	6.3 (0.0)	6.88 (0.01) $\times 10^{14}$	2.67×10^{-7}
	$20 < E_u/k < 35$	10.6 (1.4)	1.78 (0.70) $\times 10^{15}$	6.92×10^{-7}
	$50 < E_u/k < 80$	21.4 (4.7)	1.00 (0.67) $\times 10^{15}$	3.89×10^{-7}
	$E_u/k > 140$	37.1 (3.0)	1.93 (0.74) $\times 10^{14}$	7.51×10^{-8}
HC$_5$N	$E_u/k < 3$	3.8 (0.0)	2.81 (0.00) $\times 10^{14}$	1.09×10^{-7}
	$3 < E_u/k < 6$	10.6 (2.1)	3.19 (0.69) $\times 10^{14}$	1.24×10^{-7}
	$8 < E_u/k < 25$	19.9 (2.8)	4.59 (0.82) $\times 10^{14}$	1.78×10^{-7}
	$60 < E_u/k < 105$	24.8 (3.3)	4.65 (2.28) $\times 10^{14}$	1.81×10^{-7}
	$E_u/k > 150$	39.7 (17.4)	4.53 (9.00) $\times 10^{13}$	1.76×10^{-8}
C$_3$S	$E_u/k < 10$	15.4 (4.0)	1.79 (0.49) $\times 10^{13}$	9.25×10^{-9}
	$E_u/k > 40$	34.1 (2.4)	3.29 (0.46) $\times 10^{13}$	1.70×10^{-8}
C$_4$H ($\nu = 0$)	$E_u/k < 10$	13.4 (5.2)	1.96 (0.81) $\times 10^{15}$	7.60×10^{-7}
	$20 < E_u/k < 40$	21.9 (3.7)	1.84 (0.51) $\times 10^{15}$	7.14×10^{-7}
	$40 < E_u/k < 80$	48.1 (12.3)	1.77 (0.71) $\times 10^{15}$	6.87×10^{-7}
	$E_u/k > 130$	75.8 (20.1)	1.46 (0.92) $\times 10^{15}$	5.67×10^{-7}
C$_4$H ($\nu = 1$)	$E_u/k < 260$	41.4 (4.2)	1.67 (1.00) $\times 10^{17}$	6.49×10^{-5}
	$E_u/k > 315$	280.9 (209.1)	3.59 (4.68) $\times 10^{15}$	1.39×10^{-6}
CH$_3$CN	$E_u/k < 30$	11.9 (0.0)	2.07 (0.27) $\times 10^{14}$	8.03×10^{-8}
	$30 < E_u/k < 50$	25.0 (10.4)	3.35 (3.10) $\times 10^{13}$	1.30×10^{-8}
	$E_u/k > 50$	61.4 (10.9)	5.06 (2.30) $\times 10^{13}$	1.97×10^{-8}
SiS	$E_u/k < 15$	7.3 (0.3)	3.17 (0.32) $\times 10^{15}$	9.02×10^{-7}
	$20 < E_u/k < 80$	44.3 (8.5)	3.84 (1.28) $\times 10^{15}$	1.09×10^{-6}
	$E_u/k > 115$	76.8 (33.3)	6.32 (5.96) $\times 10^{15}$	1.80×10^{-6}
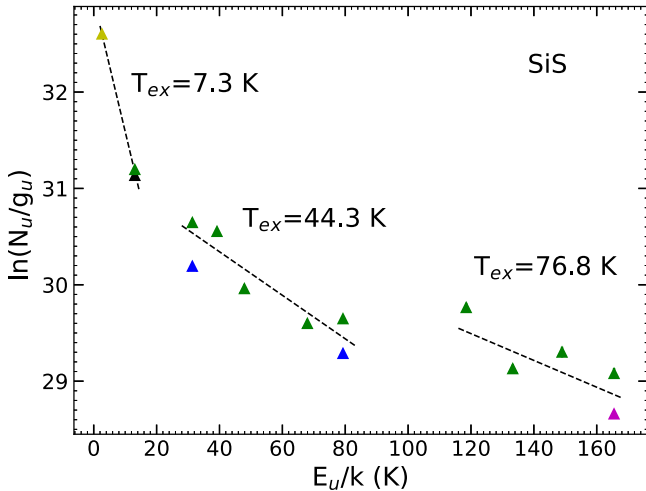
Figure F2. Same as Figure F1 but for SiS.

to be CH$_3$CN($E_u/k < 30$ K): CH$_3$CN(30 K $< E_u/k <$ 50 K): CH$_3$CN($E_u/k > 50$ K) = 1: 1.4: 3.5. For SiS, these are estimated to be SiS($E_u/k < 15$ K): SiS(20 K $< E_u/k <$ 80 K): SiS ($E_u/k > 115$ K) = 1: 6.1: 10.5. For C$_4$H ($\nu = 0$), these are estimated to be C$_4$H($E_u/k < 10$ K): C$_4$H(20 K $< E_u/k <$ 40 K): C$_4$H (40 K $< E_u/k <$ 80 K): C$_4$H($E_u/k > 130$ K) = 1: 1.6: 3.6: 5.7. The excitation temperatures of C$_4$H($\nu = 1$) are estimated to be C$_4$H($E_u/k < 260$ K): C$_4$H($E_u/k > 315$ K) = 1: 6.8.

Table F1 gives information about the excitation temperature, column density in specific levels, and fractional abundances of the molecules, relative to H$_2$, for C$_4$H($\nu = 0$), C$_4$H ($\nu = 1$), HC$_3$N, HC$_5$N, CH$_3$CN, C$_3$S, and SiS, at different upper energy levels. Figures F1 and F2 show that the thermal structures of HC$_3$N, HC$_5$N, C$_3$S, CH$_3$CN, SiS, C$_4$H($\nu = 0$), and C$_4$H($\nu = 1$)

are stratified (Chau et al. 2012). Similarly to HC$_3$N and HC$_5$N, their excitation temperatures increase with the increase of rotational energy level. Therefore, like HC$_5$N, HC$_7$N, and HC$_9$N, the high-J transitions of these molecules in the CSE of IRC+10216 can trace the warmer molecular regions. The column density and abundance derived from different transitions of the same molecule are different, which may be due to opacity effects (Zhang et al. 2017).

The low rotational lines observed in the CSE of AGB stars are seen to trace the low-temperature region, while the information on warmer regions is determined by the higher energy lines. Some molecules with stratified excitation temperatures have already been mapped with high resolution, allowing us to determine the extended ranges of the cold and warm components based on the results. These findings have been summarized in Table F2.

Thanks to previously obtained maps of C$_4$H ($\nu = 0$) by high-resolution telescopes or interferometers, we have discovered that the spatial distribution of low rotational transitions ($N = 9$–8 through $N = 12$–11) form a hollow shell structure with a width of about 3″ and a radius of about 15″ (Agúndez et al. 2017). In contrast, high rotational transitions ($N = 36$–35) show a compact spatial distribution (radius $\leqslant 2.″7$) (Patel et al. 2011). The spatial distribution between low and high rotational transitions ($N = 27$–26) has both characteristics, that is, there is a compact distribution in the center and a bright shell structure outside (Cooksy et al. 2015).

The molecule at issue is CH$_3$CN. Agúndez et al. (2015) observed the spatial distribution of CH$_3$CN ($J = 14$–13) using the ALMA telescope, which showed a hollow shell with a radius of about 2″ and a width of about 1″. However, the CH$_3$CN observed by Patel et al. (2011) using SMA ($J = 16$–15 to $J = 19$–18) indicated a compact spatial distribution with a radius of about 3″. Agúndez et al. (2015) point out that the

Table F2
Cold and Warm Components of the Extended Radius of Molecular C_4H, HC_3N, HC_5N, CH_3CN, and SiS

Species	Radial Extent (r) ($''$)	References	Telescope	Comments
HC_3N (warm)	$r \leqslant 5$	(1)	ALMA	$J = 28$–27, $J = 30$–29, and $J = 38$–37
HC_3N (cool)	$7 \leqslant r \leqslant 18.5$	(2)	ALMA	$J = 10$–9 to $J = 12$–11
HC_5N (warm)	$13 \leqslant r \leqslant 18$	(2)	ALMA	$J = 32$–31 to $J = 43$–42
C_4H ($\nu = 0$) (warm)	$r \leqslant 2.7$	(3)	SMA	$N = 36$–35
C_4H ($\nu = 0$) (cool)	$12 \leqslant r \leqslant 20$	(2)	ALMA	$N = 9$–8 to $N = 12$–11
C_4H ($\nu = 1$) (cool)	$12 \leqslant r \leqslant 18$	(4, 5)	IRAM, SMA	$N = 27$–26
CH_3CN (warm)	$r \leqslant 3.2$	(3)	SMA	$J = 16$–15 to $J = 19$–18
SiS (warm)	$r \leqslant 2$	(6)	CARMA	$J = 14$–13
SiS (cool)	$r \leqslant 10$	(7, 8, 9)	ALMA, BIMA, IRAM	$J = 5$–4, $J = 6$–5, $J = 8$–7, $J = 9$–8, and $J = 12$–11

Note. The radial extent was estimated to be the value at which the brightness distribution had fallen to half its peak value.
References. (1) Siebert et al. (2022); (2) Agúndez et al. (2017); (3) Patel et al. (2011); (4) Guélin et al. (1999); (5) Cooksy et al. (2015); (6) Fonfría et al. (2014); (7) Velilla Prieto et al. (2019); (8) Bieging & Tafalla (1993); (9) Lucas et al. (1995).

higher rotational transition lines observed with the SMA may cause the emission to shift inward, and that the compact distribution in the center may be due to the insufficient resolution of the SMA. There are chemical models that predict that most CH_3CN should be distributed at a large radius (about $18''$, see Agúndez et al. 2008b; Li et al. 2014), and other chemical models predict that most CH_3CN is located within a radius of about $15''$, but with a compact distribution of about $1''$ in the center (Agúndez et al. 2015), inconsistent with the ALMA observations. We speculate that the low-J transitions of CH_3CN are likely distributed over a large radius, and the emission may move gradually inward as the rotational energy level increases, similar to C_4H ($\nu = 0$).

Appendix G
Detailed Comparison of Emission Lines Obtained with Different Angular Resolutions

Here, we provide a comparison of the line intensities and line shapes of the same transition of a molecule obtained by telescopes with different angular resolutions, including the IRAM 30 m, Onsala 20 m, FCRAO 14 m, TRAO 14 m, PMO 13.7 m, NRAO 11 m telescopes, the Number Two 10.4 m telescope of the Owens Valley Radio Observatory, and the 7 m Bell Laboratories Antenna at Crawford Hill.

(1) *The impact of different angular resolutions on the integrated line intensities.* Comparison of emission lines observed with different angular resolutions is more uncertain if any of the observed lines are weak and we suggest that such comparisons be made only if the S/N of the lines is greater than or equal to 5. For the strong lines (S/N $\geqslant$ 5), the integrated intensity of the same molecular line from different angular resolutions is approximately identical, i.e., $\int T_R dv \approx$ const., where $T_R = \frac{T_{mb}}{\eta_{BD}}$, $\eta_{BD} = \frac{\theta_s^2}{\theta_s^2 + \theta_{beam}^2}$ (see Section 4.1.1), and $T_{mb} = T_A^*/\eta$ (see Section 2). In other words, the ratio of the integrated line intensity ($\int T_R dv$) between the same molecular transition from different angular resolutions is close to unity. For instance, Zhang et al. (2017) found that the ratios of the integrated intensities observed with the TMRT 65 m telescope for HC_7N ($\nu = 0$, $J = 16$–15), SiS ($\nu = 0$, $J = 1$–0), and HC_3N ($\nu = 0$, $J = 2$–1) to those values derived by Gong et al. (2015) using the Efflesberg 100 m telescope were 1: (0.863 $\pm$ 0.121), 1: (0.928 $\pm$ 0.029), and 1: (0.899 $\pm$ 0.020), respectively. We compare the integrated intensities of SiS, HNC, and HCN in

IRC+10216 observed by the PMO 13.7 m, TRAO 14 m, and IRAM 30 m telescopes, and find that the ratios among SiS ($J = 5$–4), HNC ($J = 1$–0), and HCN ($J = 1$–0) are 1: 0.82: 0.72, 1: 0.88: 0.86, and 1: 0.83: 1.08, respectively. The ratio of the integrated intensities of ^{13}CO deduced by the observations from PMO 13.7 m, TRAO 14 m, and 7 m Bell Laboratories Antenna at Crawford Hill telescopes is 1: 0.88: 0.96.

(2) *The impact of different angular resolutions on the line shapes.* For the strong emission lines (S/N $\geqslant$ 5), the observed spectral line shape is the same for the same transition of the same molecule with different angular resolutions. If the S/N is less than 5, the observed line profiles might differ. Take molecular C_4H as an example. Using the PMO 13.7 m telescope, we observed double-peaked structures of C_4H lines in all the $N = 9$–8, 10–9, 11–10, and 12–11 transitions with S/N $\geqslant$ 5, as shown in Figure C2. Guélin et al. (1978) observed similar transitions of C_4H via the NRAO 11 m telescope with the S/N less than 5, and obtained different conclusions: the shapes of the $N = 9$–8 and $N = 10$–9 lines were difficult to judge, due to the poor S/N; the $N = 11$–10 line showed a flat-topped structure; and the $N = 12$–11 line exhibited a double-peaked structure. The C_4H ($N = 9$–8) observed by the Onsala 20 m telescope (Johansson et al. 1984) and the C_4H ($N = 10$–9) observed by the IRAM 30 m telescope (Cernicharo et al. 1986a) both possess double-peaked line shapes.

(3) *The impact of different angular resolutions on the double-peaked spectra.* For the optically thin species that exhibit double-peaked line shapes, a more considerable intensity contrast can be found between the line wings and the line center while using a telescope with higher spatial resolution (Olofsson et al. 1982). For instance, the C_2H $N = 1$–0, $J = 3/2$–1/2, $F = 2$–1 was observed by the IRAM 30 m (De Beck et al. 2012), Onsala 20 m (Truong-Bach et al. 1987), TRAO 14 m (Park et al. 2008), and PMO 13.7 m (this work) telescopes toward IRC+10216. All of these spectra showed double-peaked shapes with S/N $\geqslant$ 5. The calculated intensity contrasts between the line wings and the line center are 2.3, 1.4, 1.3, and 1.8. These values for HNC ($J = 1$–0) are 1.8, 1.7, 1.2, and 1.4, respectively. Similarly, for ^{13}CO observed by the IRAM 30 m (Kahane et al. 1992), Onsala 20 m (Olofsson et al. 1982), TRAO 14 m (Park et al. 2008), PMO 13.7 m (this work), NRAO 11 m (Kuiper et al. 1976; Wannier & Linke 1978), and the 7 m Bell Laboratories Antenna at Crawford Hill (Knapp & Chang 1985) telescopes, these values are obtained to be 3.4, 2.6, 2.2, 2.4, 1.9, and 1.8, respectively.

ORCID iDs

Xiaohu Li ⃝ https://orcid.org/0000-0003-2090-5416
Tom J. Millar ⃝ https://orcid.org/0000-0001-5178-3656
Yong Zhang ⃝ https://orcid.org/0000-0002-1086-7922
Jianjie Qiu ⃝ https://orcid.org/0000-0002-9829-8655
Donghui Quan ⃝ https://orcid.org/0000-0003-4811-2581
Jianjun Zhou ⃝ https://orcid.org/0000-0003-0356-818X
Yu Gao ⃝ https://orcid.org/0000-0003-0007-2197
Qiang Chang ⃝ https://orcid.org/0000-0002-0040-6022
Lin Xiao ⃝ https://orcid.org/0000-0002-9511-7062
Ryszard Szczerba ⃝ https://orcid.org/0000-0003-2886-4460
Xuan Fang ⃝ https://orcid.org/0000-0002-3981-7355

References

Agúndez, M., & Cernicharo, J. 2006, ApJ, 650, 374
Agúndez, M., Cernicharo, J., & Guélin, M. 2007, ApJL, 662, L91
Agúndez, M., Cernicharo, J., Guélin, M., et al. 2010, A&A, 517, L2
Agúndez, M., Cernicharo, J., & Guélin, M. 2014, A&A, 570, A45
Agúndez, M., Cernicharo, J., Pardo, J. R., Guélin, M., Phillips, T. G., et al. 2008a, A&A, 485, L33
Agúndez, M., Cernicharo, J., Quintana-Lacaci, G., et al. 2015, ApJ, 814, 143
Agúndez, M., Cernicharo, J., Quintana-Lacaci, G., et al. 2017, A&A, 601, A4
Agúndez, M., Cernicharo, J., Waters, L. B. F. M., et al. 2011, A&A, 533, L6
Agúndez, M., Fonfría, J. P., Cernicharo, J., Pardo, J. R., & Guélin, M. 2008b, A&A, 479, 493
Agúndez, M., Fonfría, J. P., Cernicharo, J., et al. 2012, A&A, 543, A48
Anderson, J. K., & Ziurys, L. M. 2014, ApJL, 795, L1
Andrews, H., De Beck, E., & Hirvonen, P. 2022, MNRAS, 510, 383
Apponi, A. J., McCarthy, M. C., Gottlieb, C. A., & Thaddeus, P. 1999, ApJL, 516, L103
Araya, E., Hofner, P., Goldsmith, P., Slysh, S., & Takano, S. 2003, ApJ, 596, 556
Asplund, M., Grevesse, N., Sauval, A. J., & Scott, P. 2009, ARA&A, 47, 481
Avery, L. W., Amano, T., Bell, M. B., et al. 1992, ApJS, 83, 363
Avery, L. W., Broten, N. W., MacLeod, J. M., Oka, T., & Kroto, H. W. 1976, ApJL, 205, L173
Bakker, E. J., van Dishoeck, E. F., Waters, L. B. F. M., & Schoenmaker, T. 1997, A&A, 323, 469
Battino, U., Pignatari, M., Tattersall, A., Denissenkov, P., & Herwig, F. 2022, Univ, 8, 170
Becklin, E. E., Frogel, J. A., Hyland, A. R., Kristian, J., & Neugebauer, G. 1969, ApJL, 158, L133
Bell, M. B. 1993, ApJ, 417, 305
Bell, M. B., Avery, L. W., & Feldman, P. A. 1993, ApJL, 417, L37
Bell, M. B., Avery, L. W., MacLeod, J. M., & Matthews, H. E. 1992a, ApJ, 400, 551
Bell, M. B., Feldman, P. A., & Avery, L. W. 1992b, ApJ, 396, 643
Bernath, P. F., Hinkle, K. H., & Keady, J. J. 1989, Sci, 244, 562
Betz, A. L. 1981, ApJL, 244, L103
Betz, A. L., McLaren, R. A., & Spears, D. L. 1979, ApJL, 229, L97
Bieging, J. H., & Nguyen-Quang-Rieu 1989, ApJL, 343, L25
Bieging, J. H., & Rieu, N.-Q. 1988, ApJL, 329, L107
Bieging, J. H., & Tafalla, M. 1993, AJ, 105, 576
Brown, R. D., Godfrey, P. D., Storey, J. W. V., & Clark, F. O. 1976, Natur, 262, 672
Buhl, D., & Snyder, L. E. 1970, Natur, 228, 267
Bujarrabal, V., Guélin, M., Morris, M., & Thaddeus, P. 1981, A&A, 99, 239
Busso, M., Gallino, R., & Wasserburg, G. J. 1999, ARA&A, 37, 239
Cabezas, C., Cernicharo, J., Alonso, J. L., et al. 2013, ApJ, 775, 133
Cabezas, C., Pardo, J. R., Agundez, M., et al. 2023, A&A, 672, L12
Cernicharo, J., Agúndez, M., & Guélin, M. 2011, in IAU Symp. 280, The Molecular Universe, ed. J. Cernicharo & R. Bachiller (Cambridge: Cambridge Univ. Press), 237
Cernicharo, J., Agúndez, M., Velilla Prieto, L., et al. 2017, A&A, 606, L5
Cernicharo, J., Cabezas, C., Pardo, J. R., et al. 2019a, A&A, 630, L2
Cernicharo, J., Cabezas, C., Pardo, J. R., et al. 2023a, A&A, 672, L13
Cernicharo, J., Daniel, F., Castro-Carrizo, A., et al. 2013, ApJL, 778, L25
Cernicharo, J., Decin, L., Barlow, M. J., et al. 2010a, A&A, 518, L136
Cernicharo, J., Gottlieb, C. A., Guélin, M., Thaddeus, P., & Vrtilek, J. M. 1989, ApJL, 341, L25
Cernicharo, J., Gottlieb, C. A., Guélin, M., et al. 1991a, ApJL, 368, L39
Cernicharo, J., Gottlieb, C. A., Guélin, M., et al. 1991b, ApJL, 368, L43

Cernicharo, J., & Guélin, M. 1987, A&A, 183, L10
Cernicharo, J., & Guélin, M. 1996, A&A, 309, L27
Cernicharo, J., Guélin, M., Agúndez, M., McCarthy, M. C., & Thaddeus, P. 2008, ApJL, 688, L83
Cernicharo, J., Guélin, M., Agúndez, M., et al. 2007, A&A, 467, L37
Cernicharo, J., Guélin, M., Agúndez, M., et al. 2018, A&A, 618, A4
Cernicharo, J., Guélin, M., Hein, H., & Kahane, C. 1987a, A&A, 181, L9
Cernicharo, J., Guélin, M., Kahane, C., Bogey, M., & Demuynck, C. 1991c, A&A, 246, 213
Cernicharo, J., Guélin, M., & Kahane, C. 2000, A&AS, 142, 181
Cernicharo, J., Guélin, M., Menten, K. M., & Walmsley, C. M. 1987b, A&A, 181, L1
Cernicharo, J., Guélin, M., & Pardo, J. R. 2004, ApJL, 615, L145
Cernicharo, J., Kahane, C., Gomez-Gonzalez, J., & Guélin, M. 1986a, A&A, 164, L1
Cernicharo, J., Kahane, C., Gomez-Gonzalez, J., & Guélin, M. 1986b, A&A, 167, L5
Cernicharo, J., Kahane, C., Gomez-Gonzalez, J., & Guélin, M. 1986c, A&A, 167, L9
Cernicharo, J., Marcelino, N., Agúndez, M., & Guélin, M. 2015a, A&A, 575, A91
Cernicharo, J., McCarthy, M. C., Gottlieb, C. A., et al. 2015b, ApJL, 806, L3
Cernicharo, J., Pardo, J. R., Cabezas, C., et al. 2023b, A&A, 670, L19
Cernicharo, J., Velilla-Prieto, L., Agúndez, M., et al. 2019b, A&A, 627, L4
Cernicharo, J., Waters, L. B. F. M., Decin, L., et al. 2010b, A&A, 521, L8
Changala, P. B., Gupta, H., Cernicharo, J., et al. 2022, ApJL, 940, L42
Chapovsky, P. L. 2021, MNRAS, 503, 1773
Charbonnel, C. 1995, ApJL, 453, L41
Chau, W., Zhang, Y., Nakashima, J. I., Deguchi, S., & Kwok, S. 2012, ApJ, 760, 66
Churchwell, E., Winnewisser, G., & Walmsley, C. M. 1978, A&A, 67, 139
Clegg, R. E. S., Hinkle, K. H., & Lambert, D. L. 1982, MNRAS, 201, 95
Cooksy, A. L., Gottlieb, C. A., Killian, T. C., et al. 2015, ApJS, 216, 30
Cordiner, M. A., & Millar, T. J. 2009, ApJ, 697, 68
Cristallo, S., Straniero, O., Gallino, R., et al. 2009, ApJ, 696, 797
Crosas, M., & Menten, K. M. 1997, ApJ, 483, 913
Daniel, F., Agúndez, M., Cernicharo, J., et al. 2012, A&A, 542, A37
Dayal, A., & Bieging, J. H. 1995, ApJ, 439, 996
De Beck, E., Decin, L., de Koter, A., et al. 2010, A&A, 523, A18
De Beck, E., Lombaert, R., Agúndez, M., et al. 2012, A&A, 539, A108
Decin, L., Justtanont, K., De Beck, E., et al. 2010, A&A, 521, L4
Draine, B. T. 1978, ApJS, 36, 595
Epchtein, N., Le Bertre, T., Lepine, J. R. D., et al. 1987, A&AS, 71, 39
Fonfría Expósito, J. P., Agúndez, M., Tercero, B., Pardo, J. R., & Cernicharo, J. 2006, ApJL, 646, L127
Fonfría, J. P., Cernicharo, J., Richter, M. J., et al. 2015, MNRAS, 453, 439
Fonfría, J. P., Fernández-López, M., Agúndez, M., et al. 2014, MNRAS, 445, 3289
Fonfría, J. P., Fernández-López, M., Pardo, J. R., et al. 2018, ApJ, 860, 162
Fonfría, J. P., Hinkle, K. H., Cernicharo, J., et al. 2017, ApJ, 835, 196
Fong, D., Meixner, M., & Shah, R. Y. 2003, ApJL, 582, L39
Fong, D., Meixner, M., Sutton, E. C., Zalucha, A., & Welch, W. J. 2006, ApJ, 652, 1626
Ford, K. E. S., Neufeld, D. A., Goldsmith, P. F., & Melnick, G. J. 2003, ApJ, 589, 430
Ford, K. E. S., Neufeld, D. A., Schilke, P., & Melnick, G. J. 2004, ApJ, 614, 990
Gallardo Cava, I., Bujarrabal, V., Alcolea, J., Gómez-Garrido, M., & Santander-García, M. 2022, A&A, 659, A134
Gensheimer, P. D. 1997a, Ap&SS, 251, 199
Gensheimer, P. D. 1997b, ApJL, 479, L75
Goldhaber, D. M., & Betz, A. L. 1984, ApJL, 279, L55
Goldhaber, D. M., Betz, A. L., & Ottusch, J. J. 1987, ApJ, 314, 356
Gong, Y., Henkel, C., Ott, J., et al. 2017, ApJ, 843, 54
Gong, Y., Henkel, C., Spezzano, S., et al. 2015, A&A, 574, A56
Groesbeck, T. D., Phillips, T. G., & Blake, G. A. 1994, ApJS, 94, 147
Guélin, M., & Cernicharo, J. 1991, A&A, 244, L21
Guélin, M., Cernicharo, J., Kahane, C., & Gomez-Gonzales, J. 1986, A&A, 157, L17
Guélin, M., Cernicharo, J., Paubert, G., & Turner, B. E. 1990, A&A, 230, L9
Guélin, M., Green, S., & Thaddeus, P. 1978, ApJL, 224, L27
Guélin, M., Lucas, R., & Cernicharo, J. 1993, A&A, 280, L19
Guélin, M., Lucas, R., & Neri, R. 1997, in IAU Symp. 170 (CO: Twenty-five Years of Millimeter Spectroscopy) ed. Latter W. B. (Dordrecht: Kluwer), 359
Guélin, M., Muller, S., Cernicharo, J., McCarthy, M. C., & Thaddeus, P. 2004, A&A, 426, L49

Guélin, M., Muller, S., Cernicharo, J., et al. 2000, A&A, 363, L9
Guélin, M., Neininger, N., & Cernicharo, J. 1998, A&A, 335, L1
Guélin, M., Neininger, N., Lucas, R., & Cernicharo, J. 1999, in The Physics and Chemistry of the Interstellar Medium, ed. V. Ossenkopf, J. Stutzki, & G. Winnewisser (Herdecke: GCA-Verlag), 326
Guélin, M., & Thaddeus, P. 1977, ApJL, 212, L81
Habing, H. J., & Olofsson, H. 2004, Asymptotic Giant Branch Stars (Berlin: Springer)
Halfen, D. T., Clouthier, D. J., & Ziurys, L. M. 2008, ApJL, 677, L101
Hall, D. N. B., & Ridgway, S. T. 1978, Natur, 273, 281
He, J. H., Dinh-V-Trung, & Hasegawa, T. I. 2017, ApJ, 845, 38
He, J. H., Dinh-V-Trung, Kwok, S., et al. 2008, ApJS, 177, 275
He, J. H., Kamiński, T., Mennickent, R. E., et al. 2019, ApJ, 883, 165
Henkel, C., Matthews, H. E., Morris, M., Terebey, S., & Fich, M. 1985, A&A, 147, 143
Herwig, F. 2005, ARA&A, 43, 435
Hinkle, K. W., Keady, J. J., & Bernath, P. F. 1988, Sci, 241, 1319
Howard, W. E., Buhl, D., & Snyder, L. E. 1970, IAU Circ., 2251
Jefferts, K. B., Penzias, A. A., & Wilson, R. W. 1970a, ApJL, 161, L87
Jefferts, K. B., Penzias, N. J., Penzias, A. A., & Wilson, R. W. 1970b, IAU Circ., 2231
Jeste, M., Wiesemeyer, H., Menten, K. M., & Wyrowski, F. 2023, A&A, 675, A139
Jewell, P. R., & Snyder, L. E. 1984, ApJ, 278, 176
Johansson, L. E. B., Andersson, C., Elder, J., et al. 1985, A&AS, 60, 135
Johansson, L. E. B., Andersson, C., Ellder, J., et al. 1984, A&A, 130, 227
Kahane, C., Cernicharo, J., Gomez-Gonzalez, J., & Guélin, M. 1992, A&A, 256, 235
Kahane, C., Gomez-Gonzalez, J., Cernicharo, J., & Guélin, M. 1988, A&A, 190, 167
Kaifu, N., Suzuki, H., Ohishi, M., et al. 1987, ApJL, 317, L111
Kasai, Y., Kagi, E., & Kawaguchi, K. 2007, ApJL, 661, L61
Kawaguchi, K., Fujimori, R., Aimi, S., et al. 2007, PASJ, 59, L47
Kawaguchi, K., Kagi, E., Hirano, T., Takano, S., & Saito, S. 1993, ApJL, 406, L39
Kawaguchi, K., Kasai, Y., Ishikawa, S.-I., & Kaifu, N. 1995, PASJ, 47, 853
Keene, J., Young, K., Phillips, T. G., Buettgenbach, T. H., & Carlstrom, J. E. 1993, ApJL, 415, L131
Keller, D., Menten, K. M., Kamiński, T., & Claussen, M. J. 2015, in ASP Conf. Ser. 497, Why Galaxies Care about AGB Stars III: A Closer Look in Space and Time, ed. F. Kerschbaum, R. F. Wing, & J. Hron (San Francisco, CA: ASP), 123
Khouri, T., de Koter, A., Decin, L., et al. 2014, A&A, 570, A67
Knapp, G. R., & Chang, K. M. 1985, ApJ, 293, 281
Koelemay, L. A., & Ziurys, L. M. 2023, ApJL, 958, L6
Kuiper, T. B. H., Knapp, G. R., Knapp, S. L., & Brown, R. L. 1976, ApJ, 204, 408
Le Gal, R., Xie, C., Herbst, E., et al. 2017, A&A, 608, A96
Li, J., Wang, J. Z., Gu, Q. S., & Zheng, X. W. 2013, A&A, 555, A18
Li, X., Millar, T. J., Walsh, C., Heays, A. N., & van Dishoeck, E. F. 2014, A&A, 568, A111
Linke, R. A., Goldsmith, P. F., Wannier, P. G., Wilson, R. W., & Penzias, A. A. 1977, ApJ, 214, 50
Lovas, F. J. 2004, JPCRD, 33, 177
Lucas, R., Guélin, M., Kahane, C., Audinos, P., & Cernicharo, J. 1995, Ap&SS, 224, 293
Massalkhi, S., Agúndez, M., Cernicharo, J., et al. 2018, A&A, 611, A29
McCarthy, M. C., Gottlieb, C. A., Gupta, H., & Thaddeus, P. 2006, ApJL, 652, L141
McElroy, D., Walsh, C., Markwick, A. J., et al. 2013, A&A, 550, A36
McGuire, B. A. 2018, ApJS, 239, 17
McGuire, B. A. 2022, ApJS, 259, 30
Melnick, G. J., Neufeld, D. A., Ford, K. E. S., Hollenbach, D. J., & Ashby, M. L. N. 2001, Natur, 412, 160
Menten, K. M., Reid, M. J., Kamiński, T., & Claussen, M. J. 2012, A&A, 543, A73
Menten, K. M., Wyrowski, F., Keller, D., & Kamiński, T. 2018, A&A, 613, A49
Milam, S. N., Halfen, D. T., Tenenbaum, E. D., et al. 2008, ApJ, 684, 618
Milam, S. N., Woolf, N. J., & Ziurys, L. M. 2009, ApJ, 690, 837
Millar, T. J. 2020, ChJCP, 33, 668
Millar, T. J., Herbst, E., & Bettens, R. P. A. 2000, MNRAS, 316, 195
Morisawa, Y., Fushitani, M., Kato, Y., et al. 2006, ApJ, 642, 954
Morris, M., Gilmore, W., Palmer, P., Turner, B. E., & Zuckerman, B. 1975, ApJL, 199, L47
Morris, M., Zuckerman, B., Palmer, P., & Turner, B. E. 1971, ApJL, 170, L109

Müller, H. S. P., Schlöder, F., Stutzki, J., & Winnewisser, G. 2005, JMoSt, 742, 215
Nguyen-Q-Rieu, Graham, D., & Bujarrabal, V. 1984, A&A, 138, L5
Nyman, L. A., Olofsson, H., Johansson, L. E. B., et al. 1993, A&A, 269, 377
Ohishi, M., Kaifu, N., Kawaguchi, K., et al. 1989, ApJL, 345, L83
Olofsson, H. 1996, Ap&SS, 245, 169
Olofsson, H., Johansson, L. E. B., Hjalmarson, A., & Nguyen-Quang-Rieu 1982, A&A, 107, 128
Pardo, J. R., Cabezas, C., Fonfría, J. P., et al. 2021, A&A, 652, L13
Pardo, J. R., Cernicharo, J., Goicoechea, J. R., Guélin, M., & Asensio Ramos, A. 2007, ApJ, 661, 250
Pardo, J. R., Cernicharo, J., Tercero, B., et al. 2022, A&A, 658, A39
Pardo, J. R., Cernicharo, J., Velilla Prieto, L., et al. 2018, A&A, 615, L4
Park, I. H., Wakelam, V., & Herbst, E. 2006, A&A, 449, 631
Park, J. A., Cho, S.-H., Lee, C. W., & Yang, J. 2008, AJ, 136, 2350
Patel, N. A., Young, K. H., Brünken, S., et al. 2009, ApJ, 692, 1205
Patel, N. A., Young, K. H., Gottlieb, C. A., et al. 2011, ApJS, 193, 17
Peng, T. C., Humphreys, E. M. L., Testi, L., et al. 2013, A&A, 559, L8
Penzias, A. A., Solomon, P. M., Wilson, R. W., & Jefferts, K. B. 1971, ApJL, 168, L53
Pickett, H. M., Poynter, R. L., Cohen, E. A., et al. 1998, JQSRT, 60, 883
Portinari, L., Chiosi, C., & Bressan, A. 1998, A&A, 334, 505
Pulliam, R. L., Edwards, J. L., & Ziurys, L. M. 2011, ApJ, 743, 36
Pulliam, R. L., Savage, C., Agúndez, M., et al. 2010, ApJL, 725, L181
Qiu, J.-J., Zhang, Y., Zhang, J.-S., & Nakashima, J. I. 2022, ApJS, 259, 56
Quintana-Lacaci, G., Agúndez, M., Cernicharo, J., et al. 2016, A&A, 592, A51
Reach, W. T., Ruaud, M., Wiesemeyer, H., et al. 2022, ApJ, 926, 69
Remijan, A. J., Hollis, J. M., Lovas, F. J., et al. 2007, ApJL, 664, L47
Ridgway, S. T., Hall, D. N. B., Wojslaw, R. S., Kleinmann, S. G., & Weinberger, D. A. 1976, Natur, 264, 345
Sahai, R., Wootten, A., & Clegg, R. E. S. 1984, ApJ, 284, 144
Saito, S., Kawaguchi, K., Yamamoto, S., et al. 1987, ApJL, 317, L115
Schöier, F. L., Fong, D., Bieging, J. H., et al. 2007, ApJ, 670, 766
Shan, W., Yang, J., Shi, S., et al. 2012, ITTST, 2, 593
Siebert, M. A., Van de Sande, M., Millar, T. J., & Remijan, A. J. 2022, ApJ, 941, 90
Smith, C. L., Zijlstra, A. A., & Fuller, G. A. 2015, MNRAS, 454, 177
Snyder, L. E., & Buhl, D. 1971, ApJL, 163, L47
Snyder, L. E., & Buhl, D. 1972, NYASA, 194, 17
Snyder, L. E., Henkel, C., Hollis, J. M., & Lovas, F. J. 1985, ApJL, 290, L29
Solomon, P., Jefferts, K. B., Penzias, A. A., & Wilson, R. W. 1971, ApJL, 163, L53
Suzuki, H., Kaifu, N., Miyaji, T., et al. 1984, ApJ, 282, 197
Tenenbaum, E. D., Apponi, A. J., Ziurys, L. M., et al. 2006, ApJL, 649, L17
Tenenbaum, E. D., Dodd, J. L., Milam, S. N., Woolf, N. J., & Ziurys, L. M. 2010a, ApJL, 720, L102
Tenenbaum, E. D., Dodd, J. L., Milam, S. N., Woolf, N. J., & Ziurys, L. M. 2010b, ApJS, 190, 348
Tenenbaum, E. D., & Ziurys, L. M. 2008, ApJL, 680, L121
Tercero, F., López-Pérez, J. A., Gallego, J. D., et al. 2021, A&A, 645, A37
Thaddeus, P., Cummins, S. E., & Linke, R. A. 1984, ApJL, 283, L45
Thaddeus, P., Gottlieb, C. A., Gupta, H., et al. 2008, ApJ, 677, 1132
Thaddeus, P., Gottlieb, C. A., Hjalmarson, A., et al. 1985a, ApJL, 294, L49
Thaddeus, P., Guélin, M., & Linke, R. A. 1981, ApJL, 246, L41
Thaddeus, P., Vrtilek, J. M., & Gottlieb, C. A. 1985b, ApJL, 299, L63
Truong-Bach, Nguyen-Q-Rieu, Omont, A., Olofsson, H., & Johansson, L. E. B. 1987, A&A, 176, 285
Tsuge, M., Kouchi, A., & Watanabe, N. 2021, ApJ, 923, 71
Tucker, K. D., Kutner, M. L., & Thaddeus, P. 1974, ApJL, 193, L115
Turner, B. E. 1970, IAU Circ., 2268
Turner, B. E. 1971, ApJL, 163, L35
Turner, B. E. 1992, ApJL, 388, L35
Turner, B. E., Steimle, T. C., & Meerts, L. 1994, ApJL, 426, L97
Van de Sande, M., & Millar, T. J. 2019, ApJ, 873, 36
Van de Sande, M., & Millar, T. J. 2022, MNRAS, 510, 1204
Van de Sande, M., Walsh, C., & Millar, T. J. 2021, MNRAS, 501, 491
van der Veen, W. E. C. J., Huggins, P. J., & Matthews, H. E. 1998, ApJ, 505, 749
Velilla Prieto, L., Cernicharo, J., Agúndez, M., et al. 2019, A&A, 629, A146
Velilla Prieto, L., Cernicharo, J., Quintana-Lacaci, G., et al. 2015, ApJL, 805, L13
Velilla Prieto, L., Sánchez Contreras, C., Cernicharo, J., et al. 2017, A&A, 597, A25
Wannier, P. G., & Linke, R. A. 1978, ApJ, 225, 130
Wasserburg, G. J., Karakas, A. I., & Lugaro, M. 2017, ApJ, 836, 126

Wilson, R. W., Solomon, P. M., Penzias, A. A., & Jefferts, K. B. 1971, ApJL, 169, L35

Wilson, T. L., & Rood, R. 1994, ARA&A, 32, 191

Winnewisser, G., & Walmsley, C. M. 1978, A&A, 70, L37

Woods, P. M., Schöier, F. L., Nyman, L. Å., & Olofsson, H. 2003, A&A, 402, 617

Wootten, A., Lichten, S. M., Sahai, R., & Wannier, P. G. 1982, ApJ, 257, 151

Yamamoto, S., Saito, S., Guélin, M., et al. 1987, ApJL, 323, L149

Yan, Y. T., Henkel, C., Kobayashi, C., et al. 2023, A&A, 670, A98

Yang, K., Zhang, Y., Qiu, J., Ao, Y., & Li, X. 2023, PASJ, 75, 853

Zack, L. N., Halfen, D. T., & Ziurys, L. M. 2011, ApJL, 733, L36

Zhang, X.-Y., Zhu, Q.-F., Li, J., et al. 2017, A&A, 606, A74

Zhang, Y., Chau, W., Nakashima, J. I., & Kwok, S. 2020, PASJ, 72, 46

Zhang, Y., Kwok, S., & Dinh-V-Trung 2008, ApJ, 678, 328

Zhang, Y., Kwok, S., & Dinh-V-Trung 2009a, ApJ, 691, 1660

Zhang, Y., Kwok, S., Nakashima, J. I., Chau, W., & Dinh-V-Trung 2013, ApJ, 773, 71

Zhang, Y., Kwok, S., & Nakashima, J. I. 2009b, ApJ, 700, 1262

Ziurys, L. M., Apponi, A. J., Guélin, M., & Cernicharo, J. 1995, ApJL, 445, L47

Ziurys, L. M., Apponi, A. J., & Phillips, T. G. 1994, ApJ, 433, 729

Ziurys, L. M., Savage, C., Highberger, J. L., et al. 2002, ApJL, 564, L45

Zuckerman, B. 1987, in IAU Symp. 120, Astrochemistry, ed. M. S. Vardya & S. P. Tarafdar (Dordrecht: Reidel), 345